2019-09-16

Subsurface Sensing Through Data Fusion of Redundant IMU Sensors with Supervised Learning

Liu, Huan

UNIVERSITY OF CALGARY

Subsurface Sensing Through Data Fusion of Redundant IMU Sensors with Supervised Learning

by

Huan Liu

A THESIS

SUBMITTED TO THE FACULTY OF GRADUATE STUDIES

IN PARTIAL FULFILMENT OF THE REQUIREMENTS FOR THE

DEGREE OF DOCTOR OF PHILOSOPHY

GRADUATE PROGRAM IN MECHANICAL AND MANUFACTURING ENGINEERING

CALGARY, ALBERTA

SEPTEMBER, 2019

ABSTRACT

Subsurface sensors, such as inclinometers and tools used to take measurements while drilling, are important to the mining and petroleum industries. The current sensor systems are susceptible to shock, vibrations, and magnetic disturbances. To overcome these challenges, we propose a subsurface sensor fusion system with two sets of redundant inertial measurement units (IMU) to protect against magnetic and shock disturbances that affect the performance of magnetometers and gyroscopes. Orientation information is obtained by multiple micro-electro-mechanical system (MEMS) based inertial sensors, which consist of three-axis accelerometers, gyroscopes, and magnetometers.

In this thesis we obtain angular displacements using two different approaches to improve sensor robustness to magnetic and shock disturbances; also, we discuss the pros and cons of these two different approaches. The first approach is the supervised learning filter (SLF) approach, and the second is the supervised learning-Kalman filter (SL-KF) approach. In SLF, azimuth angle errors obtained from different sensors (magnetometers, accelerometers, and gyroscopes) are compared under magnetic and shock disturbance conditions; then, we employ an adaptive neuro fuzzy inference system (ANFIS) to calculate the error models of the sensors. Based on these sensors' error models, the proper weights of the azimuth angles obtained from different sensors are computed and applied to the azimuth angles to output a final azimuth angle. However, to achieve the best results of SLF, we assume that at least one magnetometer is not affected by interferences at the same time interval (two magnetometers are separated by a distance *D*, and *D*

can prevent both magnetometers from being affected by a magnetic disturbance at the same time). Therefore, SL-KF combines SLF with a KF to further reduce the effect of disturbances on sensors. SLF computes the corrected rotational angles and angular velocities that are subsequently fed into a global filter KF, which performs further corrections.

The present subsurface positioning (directional drilling) relies on angular displacements and values of measurement depth (drill string length) to estimate a well path. However, these methods have limitations to apply in working conditions (for example drill string length maybe inaccurate caused by steel expands with increased temperature and stress). To deal with the drill string length inaccuracy problem, instead of using real external measurement signals (drill string length), we use correction signals designed based on the dual acceleration difference (DAD) method to correct the positions.

The proposed ideas of angular and position estimations are evaluated by experimental results. From the angular evaluation, based on a 59 second root mean square (RMS) calculation, the error of the proposed SLF approach is about 0.26 degrees, assuming one magnetometer is not disturbed by magnetic disturbances. When all sensors are disturbed by shock and magnetic disturbances, compared with SLF, the proposed SL-KF approach increases the performance by up to 56% using a 59 second RMS calculation. From the position evaluation, the proposed dual acceleration method reduces the error magnitudes caused by disturbances from meters to millimeters.

ACKNOWLEDGEMENTS

First, I would like to extend my gratitude to Dr. Simon Park, who has directed me in this research. AI has been a dream of mine for a long time. During my Ph.D, I learned that to excel in the program, I had to leave my comfort zone. Thanks to Dr. Park's guidance, I broke the limitations of my control background.

I am also deeply grateful to Dr. Roman Shor, who generously contributed his knowledge, experiences, and connections in the petroleum industry to help me in this research. These connections with top-level engineers helped me to understand drilling and its associated challenges. In addition, I give special thanks to the committee members of ISCWSA.

I never forgot the geomatics knowledge gained from Dr. Jeong Woo Kim. Through the support of Dr. Kim, I got familiar with the drilling related geomatic knowledge. Although I am still a beginner in this field, I would like to explore it further.

"The devil is in the details": I would like to thank Dr. Ramirez-Serrano, who showed me step by step how to consider the research in detail. All these experiences are useful in my future career.

I am also grateful for the support of Dr. Yang Gao (Geomatics Engineering, U Calgary) and Dr. Maggie Chen (U Texas in Austin) and for their helpful comments on my thesis.

I would like to acknowledge the help and support of the MEDAL lab and the geomatics CAPSTONE team. Our campus experiments on directional drilling not only obtained first place at the CAPSTONE design fair but also were useful in my research.

My deepest gratitude goes to the University of Calgary for offering this research opportunity and financial support through Alberta Innovates Technology Futures (AITF) and the Ruby scholarship to complete this thesis.

Finally, I would like to thank my parents for their continuous and unlimited support with their love, encouragement and inspiration. I am also grateful to my wife and my daughters for their patience, support and continuous encouragement.

TABLE OF CONTENTS

LIST OF FIGURES

LIST OF TABLES

NOMENCLATURE

$a_{N,}a_T$	Centripetal and tangential accelerations (meter/second^2)
a_p	Acceleration magnitude
B_h	Horizontal magnetic field strength (nT, nano Tesla)
B_x, B_y, B_z	Geomagnetic field intensity (nT)
B_{sx}, B_{sy}, B_{sz}	Magnetic intensity measured by a magnetometer (nT)
$B_{sxT}, B_{syT}, B_{szT}$	Magnetic intensity after tilt compensation (nT)
$\tilde{B}_{sx}, \tilde{B}_{sy}, \tilde{B}_{sz}$	Noises of magnetometers (nT)
B_{Hiron}	Hard iron magnetic disturbances (nT)
B_{SOiron}	Soft iron magnetic disturbances (nT)
D	Distance between two IMUs on a rigid body (meter)
f	Frequency (Hz)
F	System dynamic matrix
F_t	System discrete time dynamic matrix
F_c	Coriolis force (Newton)
g	Gravity (9.8 $\mathrm{meter/second^2}$)

G	System input and noise matrix
H_n	Unit matrix
I_n	Identity matrix
K	Kalman gain matrix
K_t	Discrete time Kalman gain matrix
l_i	Measurement depth changing value in each time interval (meter)
MD_i	Measurement depth (meter)
$N(0, \sigma^2)$	Gaussian distribution
$P_t, \hat{P}_t$	Discrete time predict and update matrix of Kalman filter
$q_1\ q_2\ q_3\ q_4$	Quaternions
Q	Process covariance matrix of a Kalman Filter
R	Measurement covariance matrix of a Kalman Filter
R_A, R_B	Rotational radii of IMU_A and IMU_B (meter)
R_{x_A}, R_{y_A} and R_{z_A}	unit vector $\hat{\mathrm{R}}$ in x, y and z axes of frame A
S_p	IMU moving distance (meter)
t	Time (second)
dt	Sample time
ν	Linear moving velocity (meter/second)

w_n, ϑ_n	Process and measurement noises
W	Weight
$\ddot{x}, \ddot{y}, \ddot{z}$	Accelerations on three axes (meter/second^2)
$\ddot{x}_s, \ddot{y}_s, \ddot{z}_s$	IMU accelerometers measured accelerations (meter/second^2)
$\tilde{\ddot{x}}_s, \tilde{\ddot{y}}_s, \tilde{\ddot{z}}_s$	Noises of IMU accelerometers (meter/second^2)
x_s, y_s, z_s	IMU coordinates on three axes
x, y, z	Earth coordinates on three axes
x_c, y_c, z_c	Initial position values
$\Delta x_s, \Delta y_s, \Delta z_s$	Distance differences of two accelerometers
$\Delta x_{ref}, \Delta y_{ref}, \Delta z_{ref}$	Reference distance differences of two accelerometers
X	System dynamic states
X_t	System discrete time states
Y_t	System discrete time outputs
α	Rotation angle around an axis $\widehat{\mathrm{R}}$ defined in frame A
$\beta_{roll}, \beta_{pitch}, \beta_{yaw}$	Euler angles (degree)
$\theta_x, \theta_y, \theta_z$	Angles rotate around x, y and z axes (degree)
$\dot{\theta}_x, \dot{\theta}_y, \dot{\theta}_z$	Angular speeds around x, y and z axes (degree/second)

$\ddot{\theta}_x, \ddot{\theta}_y, \ddot{\theta}_z$	Angular accelerations around x, y and z axes (degree/second^2)
$\theta_{sx}, \theta_{sy}, \theta_{sz}$	Angles rotate around x_s, y_s and z_s axes of IMUs (degree)
$\dot{\theta}_{sx}, \dot{\theta}_{sy}, \dot{\theta}_{sz}$	Angular speeds around x_s, y_s and z_s axes of IMUs (degree/second)
$\ddot{\theta}_{sx}, \ddot{\theta}_{sy}, \ddot{\theta}_{sz}$	Angular accelerations of IMUs (degree/second^2)
ρ	Rotational radius in polar coordinates (meter)
σ	Noise standard deviation
σ^2	Noise variance
$\gamma_{Azi}, \gamma_{Incli}$	Ratio factors of dual acceleration difference method
ω	Angular velocity (degree/second)

CHAPTER 1. INTRODUCTION

1.1 Background and Motivations

Subsurface sensing evaluates the performance of subsurface industry activities. These activities include reservoir status monitoring with inclinometers, enhanced oil recovery (EOR), carbon capture and storage (CCS), hydraulic fracking (HF), and measurement while drilling (MWD) during horizontal drilling operations. The sensors used in subsurface industry activities must provide the proper angles and positions.

For angle measurements, traditional technologies often use gas or liquid bubble-based sensors to estimate tilting states [Hwang 2017]. This type of measurement uses gravity when the instrument tilts. The bubble moves to maintain its alignment with the gravity vector allowing the pitch and roll angles to be obtained and scaled with the alignment. Inertial accelerometers are another means of measuring rotation angles between sensor coordinates and the Earth's gravity coordinates [Luinge 2002; Sprager et al., 2015]. These gravity-based orientation measuring sensor systems (such as bubble-based sensors or inertial accelerometers) depend on the angles between the gravity field and the instruments rotation plane [Trimpe et al., 2010].

The drawback of these devices is that the Earth's gravity field makes it difficult to measure the azimuth (yaw) directions that are generated on the plane that is horizontal to the ground [McElhinney et al., 2000]. Magnetometers (compasses) can measure full orientations, including azimuth, but they are very noisy and easily affected by magnetic disturbances [Ren et al., 2014]. A hybrid multi-sensor system that combines a magnetometer with a gyroscope can increase the accuracy of the azimuth since the gyroscope's signal is not affected by magnetic disturbances. The combination of these two sensors removes the noise inherent in magnetic signals and reduces the integral calculation drift caused by the near-direct current (DC) component of gyroscope signals [Borenstein et al., 2009].

For travel path positioning measurements, when estimating a moving position, accelerometers measure acceleration and then double integrate it to compute the moving distance. Velocity can also be determined during this integral calculation [Axelsson et al., 2012]. Similar to the drawback of gyroscopes, the DC components and noise from the acceleration measurements can cause drift during the integral calculation [Latt et al., 2011].

Multi-sensor fusion systems are becoming popular because of their enhanced measurement accuracy and reliability in terms of tracking and target identification. Another benefit is their improved robustness against failure. Sensor fusion systems take measurements of an environment from multiple sources and combine those measurement data to produce the best possible performance.

For example, inertial measurement systems (IMUs) are built using a self-contained navigation technique in which measurements are provided by gyroscopes, magnetometers, and accelerometers. IMUs utilize these three types of signals to estimate the orientations and positions of an object. Because of its low cost, IMUs are used in many multi-sensor information fusion (MSIF) applications. Combined with other sensors, such as global positioning systems (GPS), cameras, radar, and lasers, MSIF can be used for dead reckoning, automotive tracking, human motion detection, indoor navigation, etc. External sensors are implemented as references in many inertial motion capture systems to reduce the drift of acceleration integral calculations [Ilyas et al., 2016]. Many studies have focused on the performance of a combination of IMUs and external sensors in systems such as ultrasonic sensors, laser range sensors, cameras, GPS, and radar [Hellmers et al., 2013; Kim et al., 2015; Girard et al., 2011].

However, the above-mentioned methods do not reduce the influence of unknown magnetic disturbances caused by iron materials or other magnetic resources, since, for underground sensing, external sensor corrections (GPS, etc.) are difficult to obtain. It is therefore not feasible to measure the Earth's magnetic field in the presence of iron materials, which include casings, drill pipes, and iron ores that are present in the subsurface. Although the effect of this magnetic interference can be reduced by utilizing long, non-magnetic drill collars, this solution is expensive due to the relatively high cost of these non-magnetic materials. In addition to magnetic disturbances, IMUs also suffer from shock impacts that are caused during the drilling work process. These shocks reduce the performance of gyroscopes.

The sensor system currently used in the industry, MWD, does not favor gyroscopes [Shor et al., 2015]; applying gyroscopes in cases of rapidly rotating objects with large accelerations has drawbacks [Larin et al., 2012]. The measurement ranges of the MEMS gyroscopes included in the IMUs we are using are only hundreds of degrees/second [Iozan et al., 2016; Cao et al., 2017]. Consequently, each gyroscope is limited by a maximum angular velocity constrained by design structures, especially for MEMS gyroscopes [Tsai et al., 2010]. Also, various shock impacts affect the performance of MEMS gyroscopes. Although the requests for size, weight, reliability, and power consumption can be satisfied because advanced materials technologies can build miniature sensing elements, such as fiber-optic coils, the costs are unacceptable [Gebre-Egziabher et al., 2004].

Therefore, using redundant accelerometers to obtain rotation information is becoming popular [Wang et al., 2014; Bhuiyan et al., 2013]. Without assistance from gyroscopes, the minimum number of accelerometers needed to extract three-dimensional (3D) rotational information is six. Further, using six accelerometers creates an additional integration for the inertial mechanization and requires a non-coplanar array geometry [Nilsson et al., 2016]. Therefore, the configuration of two IMUs and three accelerometers on the *x*, *y*, and *z* axes of each IMU satisfies the minimum requirements to obtain rotational information with only accelerometers.

Because it is difficult to utilize external location correction sensors such as GPS [Tarokh 2007], one of the challenges in displacement tracking is the lack of information resources, similar to the case of using only accelerometers without the assistance of extra correction sensors. The noise, DC components, and shocks contained in acceleration signals cause a long-term double integral calculation of acceleration drift in displacement estimations. A new fusion method with improved robustness against magnetic disturbances that can perform with relatively high accuracy in terms of position estimation is of the utmost interest.

Traditional underground path position estimation methods, including the minimum curvature method (MCM) and spline curve methods such as the advanced spline-curve (ASC) method. The MCM is the most common model from the defined algorithms used to compute wellbore trajectory. The orientation angles (inclination and azimuth) and pipe length are inputs of the MCM and ASC. The MCM assumes that the arc between survey stations is a constant curvature. However, high resolution surveys show that this assumption is not true because of the negative influence of the sliding/rotational pattern drilling [Lentsch et al., 2012]. Since MCM tends to create an artificially low tortuosity by mathematically smoothing the well path between survey stations, MCM miscalculates the true vertical depth (TVD) and underestimates torque and drag (T&D). To overcome these limitations, researchers developed the ASC model to provide realistic results and accurately calculate the spatial course of the well path [Abughaban et al., 2016]. ASC methods are accurate [Amorin et al., 2010; Sampaio 2007], but the accuracy of both MCM and ASC methods depend on their inputs: orientation angles and measured depth. Therefore, MSIF technologies that can improve the accuracy of orientation angles and travel path positions are necessary.

MSIF design methodology is used in various methods that generally use either a stochastic approach or an artificial intelligence (AI) process. In stochastic methods, a Kalman Filter (KF), an Extended Kalman Filter (EKF), or an Unscented Kalman Filter (UKF) are the basis of the data fusion design. KFs remove the uncertainties of sensors and output accurate information, but their computations are complicated and need a priori noise information for co-variance matrices designs.

A particle filter (PF), also known as a Monte-Carlo filter, is another methodology that can solve hidden Markov chain and nonlinear filtering problems. Similar to EKFs and UKFs, PFs are also suitable candidates for nonlinear filter design. In AI approaches, artificial neural networks (ANNs), fuzzy logic (FL), or adaptive network-based fuzzy inference systems (ANFIS) are typically used to judge the weights of different sensors under precise rules and to improve the performance of methods (such as KFs) that are designed based on probability [Chavez-Garcia et al., 2016; Chavez-Garcia 2014; Jeon et al., 2014; Brigante et al., 2011; Dong et al., 2009; Bancroft et al., 2011].

To address the above-mentioned problems of subsurface sensing, this study provides several multi-sensor fusion approaches to decrease the effect of shock and magnetic disturbances on the sensors. The fusion structure is based on the supervised learning method and KF. Also, the dual acceleration difference method is applied to generate a correction signal for the output computation of KF.

1.2 Research Objectives

The goal of this study is to develop a sensor fusion system that minimizes the effect of unknown magnetic and shock disturbances on subsurface orientation and travel path position estimations. This technology reduces wellbore orientation errors caused by magnetic and shock interferences. The proposed sensor fusion system is also minimally affected by shocks when estimating position based on redundant acceleration information. This fusion system can be applied in wellbore positioning, and it can show the states of underground reservoirs using precise rotational measurements.

Different kinds of sensors can be fused to obtain better performance compared to the performance of individual sensors on their own. Therefore, utilizing redundant sensor information in this research is considered to improve detection performance. We have two primary objectives. First, to develop a better fusion method to estimate the orientation angles of a sensor system which will be used for underground sensing. This fusion estimation technique can be applied to contaminated magnetic environments and shock working conditions. The second objective is to build a robust position fusion system to prevent underground position estimations from being affected by magnetic and shock interferences.

The methodology of the first objective utilizes a simple sensor structure comprised of a rigid beam element and two sets of redundant IMUs that move in translational and rotational directions. Using this method, a robust azimuth orientation estimation under unknown magnetic and shock disturbances is achieved. For the second objective, orientation angles obtained from the proposed method are then combined with acceleration signals to determine positions. Diverse interference types that commonly occur in the environment are studied under different operational conditions to evaluate the performance of this method.

1.2.1 Hardware Design of Proposed Sensor System

Due to a lack of information on position tracking under conditions without GPS, it is necessary to develop a virtual simulation environment to test sensor performance under actual application conditions. This research checks several different conditions in the real subsurface sensing field, including various position tracking simulations, and simulates working conditions that experience magnetic and shock disturbances.

A base prototype of the sensor configuration is developed. This prototype system includes two sets of IMUs positioned on a rigid body of related electrical circuits designed for long-distance sensing conditions, such as long-distance signal transferring, data conversion modules, etc. A high-precision 3D calibration test rig is also built to generate orientation (inclination and azimuth) and translational motions to simulate a subsurface tracking situation. The prototype of the sensor is tested for different conditions, such as rotational, translational, 2D, and 3D movements.

1.2.2 Robust Angular Fusion-minimizing Magnetic and Shock Disturbances for Azimuth Orientation Estimation

The first objective is to build a robust angular fusion system to minimize unknown magnetic distortions and shock impacts and to prevent underground azimuth and position estimations from being affected by magnetic and shock interferences. Two fusion structures are considered to address this problem, including the stochastic fusion (KF), which consists of gyroscopes and magnetometers, and an intelligent fusion based on ANFIS. Simulations and experiments that use a 3D calibration tool and on-campus GPS are conducted to investigate the effectiveness of each method.

Subsurface angle estimations are affected by un-known magnetic disturbances and shock impacts. The shocks negatively affect gyroscopes and are obstacles to achieve accurate estimations of continuous wellbore surveys. We propose using a supervised learning filter (SLF), which includes different error models of different kinds of IMU sensors (accelerometer, gyroscope, and magnetometer) with ANFIS, when the IMU sensor experiences shock and magnetic disturbances. Based on these error models, proper weights of these different IMU sensors are calculated. Finally, these weights correct the azimuth angles obtained from the sensors. In addition, SLF can be combined with a KF to further reduce the impact of magnetic and shock disturbances.

The sensor fusion algorithms are evaluated using experimental data. The results show that SLF and it's variant, SL-KF, are good candidates to determine accurately orientation angles and remove unknown magnetic and shock disturbances.

1.2.3 Robust Position Fusion-minimizing Magnetic and Shock Disturbances for Movement Displacement Estimation

The second objective is to build a fusion method that can be used for subsurface position tracking without external location correction sensors such as GPS. Also, this fusion method should be able to deal with insufficient or inaccurate external position correction situations, such as errors in drill string correction (errors caused by steel stretch). In addition, shock robustness should be included in this method.

To satisfy the above requirements, we develop a position measurement system using redundant sets of accelerometers and polar coordinates. A KF is used to reduce the effect of shock disturbances on position estimations; a dual acceleration difference method is applied to design the proper covariance matrices of a KF. First, errors in the process and measurements are computed by comparing the process and measurements with the reference values calculated using the dual acceleration difference method. Then the errors are inputted into the covariance matrices (Q & R). Based on the proper covariance matrices, the KF computes the correct weights of the predicted and observed values for the final output. According to the experiment, the dual acceleration difference KF (DAD-KF) reduces the effect of shocks on the position.

1.3 Organization of Thesis

Chapter 2 is a literature survey on sensor fusion and inertial sensors. Existing multi-sensor fusion systems and their industrial applications are described. This chapter also discusses current sensor fusion concepts and approaches.

Chapter 3 outlines the experimental procedure and setup. This chapter presents the proposed sensor design for subsurface application, which considers long-distance digital data transfer and has a unique structure of sensor configuration. Then the processes of building high-precision calibrations (2D and 3D) for magnetometers and the process of dynamic acceleration compensation for accelerometers are discussed. The compensated and calibrated results are also presented. Finally, a testing rig and its control system are described.

Chapter 4 focuses on detailed methodologies of the proposed sensor fusion for determining orientation angles. The importance of orientation angle fusion is briefly discussed; then an overall perspective on the proposed technique is provided. In addition, this chapter shows how a SLF can reduce the effect of magnetic and shock interferences. Chapter 4 includes the details of error model building with ANFIS amd describes how the SL-KF hybrid increases KF's robustness to unknown magnetic and shock disturbances. Lastly, the proposed fusion methods are evaluated by conducting experiments, and the limitations and assumptions of the experimental results are discussed.

Position estimations are shown in Chapter 5. A dual acceleration difference method is proposed to compute the correction values for a KF's covariance matrices design (Q & R matrices). The purpose of the design is to increase the robustness of the KF to shock disturbances for position estimations. The lab-scale test shows the proposed DAD-KF is not affected by shocks. Also, a two-level positioning method is proposed and tested using a drilling simulation field positioning test to determine if the method is suitable for application in industry.

Chapter 6 provides a summary of this research and the future work.

CHAPTER 2. LITERATURE SURVEY

Subsurface sensing is crucial to subsurface industry activities. The current subsurface sensing research focuses on MEMS inertial sensors since the sensors have the advantages of being small and light-weight, can be cheaply manufactured, and require less power [Eldesoky et al., 2017]. The IMUs used in subsurface sensing usually contain accelerometers, gyroscopes, and magnetometers.

Each type of sensor has different limitations. Multiple Sensor Fusion Systems (MSFSs), technology that automatically analyzes and integrates information obtained from different sensors based on certain algorithms, was recently developed to achieve more accurate estimations than a single sensor or information source alone can provide [Lu et al., 2014; Dong et al., 2009; Aydin et al., 2018]. Information integration technologies complement and optimize different information from sensors to achieve the most realistic output possible. These technologies minimize weaknesses in individual sensors that may produce poor readings, which can include disturbances, noises, and other uncertainties [Luo et al., 2011].

Compared to a single sensor sensing system, a MSFS is more complicated and has a higher cost, but these disadvantages are minimal compared to the advantages [Cappello et al., 2015]. A MSFS improves a system's robustness because different sensors can compensate for one other even if some sensors perform poorly under harsh conditions. It also performs better in terms of noise reduction and accuracy. MSFS, along with redundant data, can provide more information to help obtain a clearer result. [Gao et al., 2018].

In this chapter, section 2.1 reviews the recent trends in subsurface sensing technology. Particular attention is paid to two applications: inclinometers and directional drilling surveys.

Section 2.2 introduces physical structures and challenges and compensations of the MEMS-based IMUs. In section 2.3, multiple sensor algorithms and development trends based on IMUs in many application fields are reviewed, including KFs and their variations and intelligent filters. Section 2.4 summarizes this chapter.

2.1 Subsurface Sensing Technologies

Subsurface injection operations(SIO) and directional drilling surveys are the two key applications in the subsurface sensing field. Inclinometers for subsurface sensing are usually used to measure the inclinations caused by subsurface movement. In addition, they are often applied to monitor subsurface deformation due to reservoir injection. SIO includes CCS, water flooding, steam injection, and waste disposal. Similar monitoring requirements are seen in shale gas or oil operations that involve hydraulic fracking [Warpinski 2013]. In these applications, detecting leakages and ground movements is needed, and if necessary, corrective actions can be undertaken to prevent catastrophic failures occurring. Direct monitoring of reservoirs is, however, difficult. Instead, heaving information is usually collected near the surface, and stress and volumetric expansion of the reservoir and leakage information can be indirectly acquired from the heaving data [Vasco 2000]. The reverse method is usually applied to determine the reservoir information according to the inclinometer measurements.

Directional drilling survey obtains the drilling trajectory orientations and positions. A complete knowledge of the wellbore direction and orientation during the drilling process is essential to guarantee proper directional drilling procedure [ElGizawy et al., 2009]. Therefore, directional drilling survey technologies, which include discrete and continuous surveys, are necessary to estimate the borehole positions or 3D space of a well path. The discrete wellbore survey is an accurate method, but it requires a series of halts in the drilling process to give static conditions for obtaining the directional measurements, such as the inclination and azimuth [Buchanan et al., 2013]. In contrast, for continuous surveys, the halts are not necessary because directional steering parameters, such as the gravity tool face, are added [Stockhausen et al., 2016]; however, moving noise is challenging. Currently, the azimuth error range of continuous surveys is approximately from 3 degrees to 20 degrees [Xue et al., 2016; Edvardsen et al., 2014].

Directional drilling surveys require orientation angle sensors to provide azimuth, inclination angles for the drill, drill string length, and calculation methods such as MCM [Yuan et al., 2015] and ASC [Abughaban et al., 2016]. These angle sensors are part of the MWD tool, which in current technology is installed several feet behind the drill bit [Noureldin et al., 2002]. Finally, combining the orientation angles and drill string length allows for borehole positions to be calculated using MCM and ASC. Therefore, the accuracy of the orientation angles and drill string length significantly influences borehole positioning.

IMU sensors measure orientation angles, but unfortunately, the sensors are affected by magnetic and shock disturbances, which occur when drilling takes place. Drill string length is less affected by magnetic and shock disturbances; however, the length values are not accurate due to the string steel stretch error, which is caused by drill string weight and the subsurface thermal evvironment. Also, the magnitude of the error may be up to 2.5/1000 meters [Henderson 2009; Lowdon 2014].

2.1.1 Inclinometer

Inclinometers have undergone rapid evolution in recent years. Current inclinometers contain high-precision instruments with a sensitivity that can detect tilting angles. Typically, an inclinometer is a metal cylinder with a length of roughly 1 or 2 meters and a diameter of 15 centimeters. It contains a tiltmeter (on an orthogonal axes) and precision electronics [Hisz et al., 2013]. One example is the bubble inclinometer, where a gas bubble contained within a conductive, liquid-filled glass casing is used to detect the Earth's gravitational field [Roberts et al., 1993]. As the instrument tilts, the bubble moves to maintain its alignment with the gravity vector. Precision electronic products detect changes in resistivity, which are caused by the motion of the gas bubble, between electrodes mounted on the glass sensor.

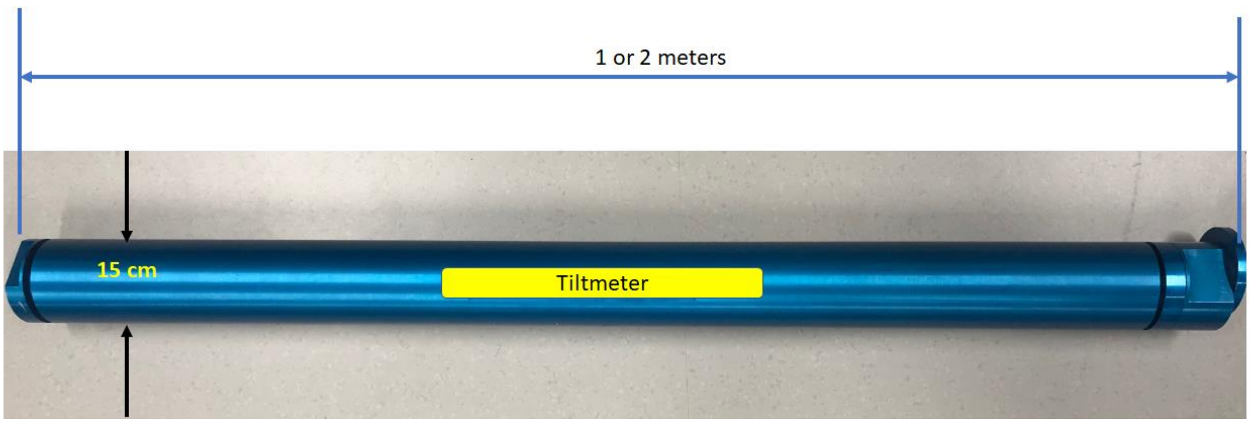

Figure 2.1.1 Structure of a tiltmeter

Other kinds of inclinometer systems have also been proposed. One example is the thermal inclinometer designed based on the analysis of a thermal profile [Johann et al., 2006]. This system demonstrates that temperature difference has a proportional relationship to the tilting angle. Another proposed system is the magneto-resistive inclinometer. In this system, a tilting motion causes magnets to move, which in turn changes the magnetic flux. The resistance change of the magneto-resistive elements then reflects the tilted angle [Jogschies et al., 2015].

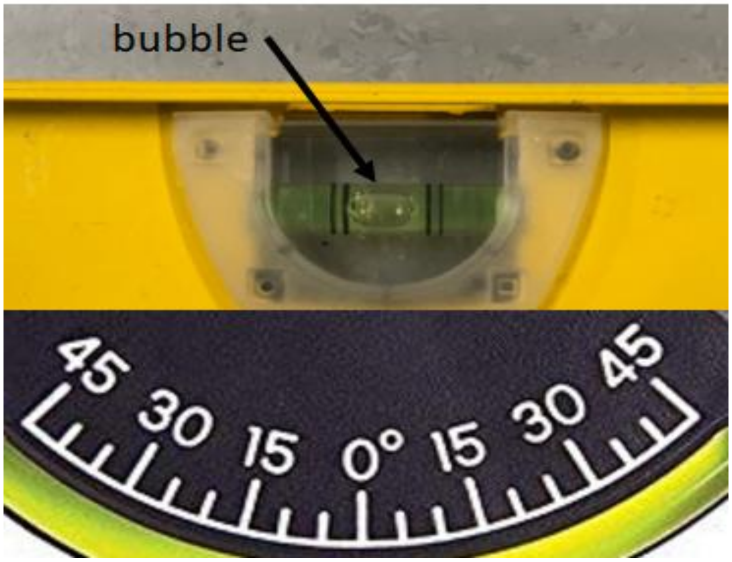

Figure 2.1.2 Structure of a bubble type tiltmeter

These types of inclinometers all have limited reliability. As a result, inertial sensors, particularly MEMS inertial sensors, are becoming an increasingly attractive alternative; the main areas of current inclinometer research are MEMS inertial sensors [Kok et al., 2017]. In this type of system, an inertial navigation system (INS) uses a self-contained navigation technique in which measurements are provided by gyroscopes, magnetometers, and accelerometers; fusing these three kinds of signals allows the orientations and positions of an object to be estimated.

Inclinometers are used to measure the tilting of an object. It typically includes a tilt meter and related electronics with different variants such as bubble, thermal, or inertial sensors. The current inclinometer research focuses on MEMS inertial sensors because of the feature of self-contained navigation.

2.1.2 Directional Drilling Survey Sensors

During the last two decades, directional drilling processes have been the subject of intensive research because oil companies and drilling contractors are interested in these technologies. If one first drills into an oil-bearing formation at an angle and then follows the formation horizontally, the productivity and longevity of a producing well can be significantly increased. Also, a directional drilling system should include directional drilling survey equipment and a steerable system in addition to the conventional drilling assembly [Noureldin 2002]. A directional drilling assembly consists of a bit, stabilizers, a motor section, and MWD as shown in Figure 2.1.3. The non-magnetic drill collar holds the surveying equipment.

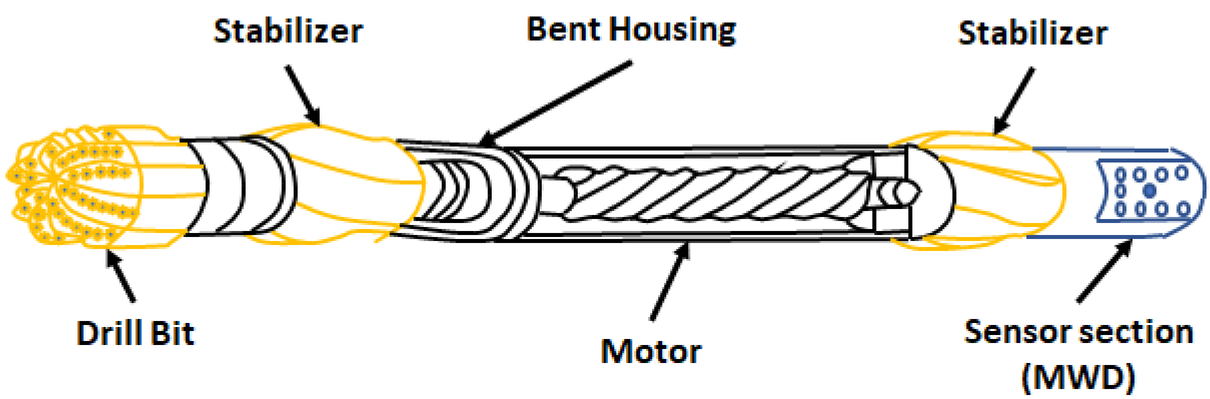

Figure 2.1.3 Structure of a directional drilling tool [Modified from ROTATE DRILLING MOTOR 2019]

The directional drilling procedure begins with drilling a vertical hole to an appropriate depth using conventional rotary drilling [ElGizawy 2009]. Drilling survey systems are typically used to provide the position and orientation of the bottom hole assembly for the drilling process. Current directional drilling survey systems are based on magnetic surveying technology [Song et al., 2018] where the magnetic surveying part of the drilling survey system is a special non-magnetic drill collar consisting of three-axis accelerometers and three-axis magnetometers [Xue et al., 2014]. This method does not consistently perform well because of magnetic interference, which are randomly located and difficult to predict [Kaur et al., 2011]. Such magnetic disturbances can be caused by drill string components that may contain magnetic interference, geomagnetic influences, downhole ore deposits, etc. [Zhang et al., 2016]. In addition, harsh working conditions, such as shocks, are encountered in directional drilling; therefore, gyroscopes are not favored since they are easily and negatively influenced by the shocks. Moreover, the large sensor size is a significant limitation of directional drilling survey applications. MEMS-based IMUs are a good alternative solution to this problem since MEMSs are very small and can easily meet size requirements [Hirama 2015]. The drawback of MEMS sensors is their limited practical application due to low precision.

Directional drilling is crucial to the petroleum industry. However, the current technologies used in directional drilling suffer from size limitations, magnetic and shock disturbances, and drill string length errors caused by steel stretches. MEMS IMUs are good alternatives in terms of addressing the size limitation and they can endure severe shocks. For example, a shock test with severe shock forces of 1400 g over 0.017s at a frequency of 3400 Hz for 4 hours proved the MEMS IMUs can be fully functional in drilling applications [ElGizawy 2009]. However, the fusion robustness to the magnetic and shock disturbances also to the stretch errors are still needed to be considered.

2.1.3 Challenges of MEMS for Subsurface Sensing

Using MEMS IMUs for current drilling survey system needs to consider the sampling time range. Current drilling industry practices use 30, 90, 120, and 180 Hz under drilling working conditions since the drilling characteristics are obvious at low frequencies [Tang 2016]. For MEMS sensors, the sampling time can be set up to 800 Hz [Analog Device].

The most traditional method to determine orientation angles uses a combination of accelerometers and magnetometers. Also, the angular rates measured from gyroscopes are employed to remove noises that are embedded in the accelerometers and magnetometers [Kao et al., 2008]. A hybrid multi-sensor system that combines a magnetometer with a gyroscope can increase the accuracy of the azimuth angles because a gyroscope's signal is unaffected by known magnetic disturbances. A combination of these two sensors with a KF removes the noise inherent in known magnetic signals and reduces the integral calculation drift caused by the DC component of gyroscope signals [Borenstein et al., 2009; Liu et al., 2018]. However, the magnetic disturbances are unknown, and traditional KFs cannot filter out unknown disturbances in many situations.

Geo-referencing is a possible method to identify the magnetic disturbances. For example, the earth's magnetic field is distorted by ambient ferromagnetic objects, so to judge whether a magnetometer is influenced by magnetic disturbances or not, researchers propose using parameters from the Earth's magnetic field model, such as Geomagnetism Canada, to compare with the measurements from magnetometers [Liu et al., 2018; Liu et al., 2019]. However, this method requires information from the Earth's magnetic field, which is difficult to obtain during field applications. The traditional method is fused with MEMS gyroscopes to reduce heading errors because information on angular speeds measured using gyroscopes can be utilized to determine rotation angles through simple integral calculations [Kok et al., 2017; Tan et al., 2018]. In this situation, gyroscopes are employed to correct heading errors since the integral calculation is not influenced by magnetic disturbances [Fan et al., 2017; Zhang et al., 2011].

However, there are several problems with gyroscope using; compared to surface sensing activities (for example, detecting indoor or outdoor vehicle movements), subsurface movements are much slower. For this reason, magnetometers may be exposed to ferromagnetic objects for a long time; therefore, the drift caused in the gyroscope integral calculation will not be ignored [Lee et al., 2016].

In addition to integral calculation drift, gyroscope applications in the cases of rapidly rotating objects with large accelerations experience difficulties [Larin et al., 2012] since each gyroscope is limited by a maximum angular velocity constrained by design structures, especially for MEMS gyroscopes [Tsai et al., 2010]. MEMS gyroscopes in the IMUs we are using are unable to function accurately under the harsh conditions caused by the large rotational accelerations that occur during drilling processes since a typical MEMS gyroscope measurement range is only hundreds of degree/s [Iozan et al., 2016; Cao et al., 2017]. Since MEMS gyroscopes are limited by a maximum angle velocity constrained by design structures [Tsai et al., 2010], the harsh working conditions caused by the large rotational accelerations and shock impacts during drilling survey processes can damage the structure of the MEMS gyroscopes. In addition, MEMS gyroscopes are subjected to various shock impacts [Li et al., 2014], and these shocks and vibrations can cause significant drift during the data integral calculation process [Du et al., 2018]. Further, the costs make this technology prohibitive, even though the advanced materials technologies can build miniature sensing elements, such as fiber-optic coils, to satisfy the requirements for size, weight, reliability, and power consumption [Gebre-Egziabher et al., 2004]. Therefore, industry practices do not favor gyroscopes [Shor et al., 2015].

Consequently, researchers explored the possibility of using redundant accelerometers to replace gyroscopes to obtain the rotation information [Wang et al., 2014; Bhuiyan et al., 2013]. However, the redundant accelerometer method also has limitations [Nilsson et al., 2016]: a minimum of six accelerometers are necessary to extract 3D rotational information and the configuration of the six accelerometers needs a non-coplanar array geometry. Therefore, two redundant sets of IMUs with a known distance D satisfy the minimum requirements for obtaining rotational information using only accelerometers since there are three accelerometers on the *x*, *y*, and *z* axes of each IMU (totaling six accelerometers), and they are not coplanar.

2.2 MEMS-Based Inertial Measurement Units (IMU)

IMUs can provide basic orientation and position information for subsurface monitoring. An IMU generally consists of a proof mass that is suspended by a series of springs and/or beams that allow the mass to oscillate around a set zero point. The sensor is then able to measure the motion of the body to which it is attached by relating the displacement of the proof mass to the dynamic characteristics of the internal components. Modern day inertial sensors used for navigation purposes primarily consist of accelerometers, gyroscopes, and magnetometers that measure linear acceleration, angular velocity, and azimuth direction respectively.

2.2.1 Accelerometers

A simplified accelerometer model is shown in Figure 2.1.4. Inertial forces are measured along the axis of motion of a suspended proof mass within the accelerometer. The mass is attached to both a spring and a dashpot element. Motion causes the proof mass to move from its set null point. The inertial sensor then transmits this information to the system’s user typically through the use of magnetic coils. An electric current is passed through the coils to apply a restoring force to the proof mass as a response to outside inertial forces. The amount of current required to maintain the zero position of the mass is directly proportional to the magnitude of the inertial force applied to the accelerometer.

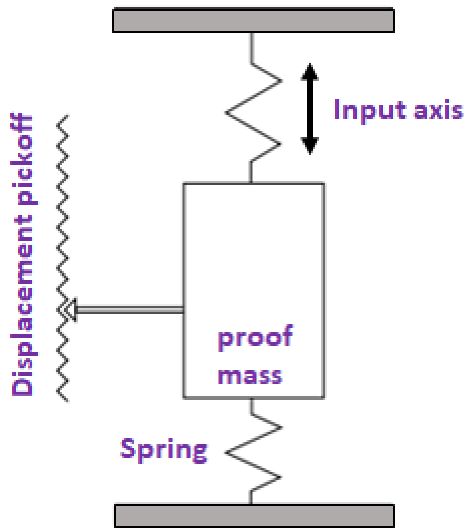

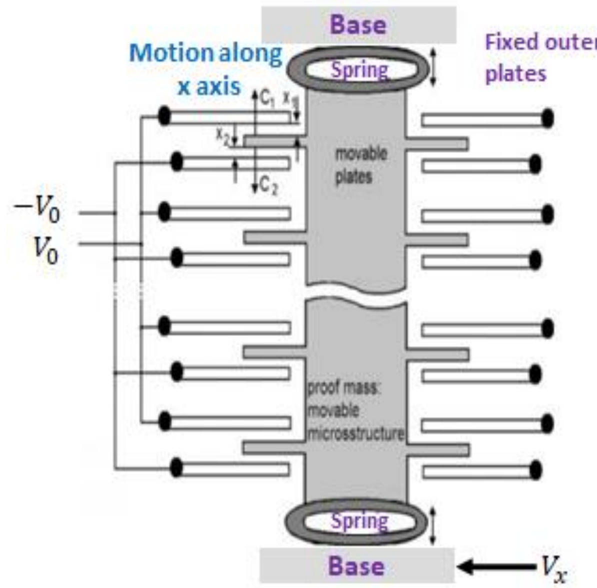

[Principle, modified from Woodman, 2007] [MEMS Structure, modified from Qazizada, 2016]

Figure 2.1.4 Mechanical accelerometer

Inertial forces, commonly referred to as the specific force, account for the local gravity field and the actual acceleration of the object. An accelerometer measures the acceleration of a body with respect to free fall rather than to its total acceleration. For example, if the accelerometer is placed at rest on a table with the sensitive axis oriented in the same direction as the local gravity vector, the accelerometer measures the magnitude of the local gravity vector. However, if the accelerometer is then dropped from the table so that it is in free fall, the sensor measures approximately 0 g. Similarly, if the accelerometer is suddenly lifted from the table, the sensor measures the upward acceleration in addition to the gravity vector. The accelerometer does not necessarily measure gravity itself, but rather its acceleration relative to gravity.

2.2.2 Gyroscopes

A gyroscope provides information on a body's rotation with respect to the inertial reference frame. There are two types of commercially-available gyroscopes: gimbal and strapdown [Woodman 2007]. A gimbal sensor has a platform that is kept aligned with the navigational frame. As the body to which the gimbal system is attached rotates through the inertial frame, the gimbals rotate in such a way that the angular momentum vector of the spinning disc does not change its orientation. In contrast, the platform of a strapdown gyroscope is kept aligned with the body frame. The gimbal sensor is more accurate and requires less computational work than a strapdown gyroscope, but its larger size and higher cost mean that the strapdown sensor is more common. In this research, we use strapdown sensors. The inertial sensors are mounted rigidly on the device in strapdown systems, allowing output quantities to be measured in the body frame rather than the global frame.

MEMS gyroscopes make use of the Coriolis effect, which states that when the body frame of an object traveling along a linear path is rotated with respect to an inertial frame, a force is applied to the body in a direction perpendicular to the motion and in the same plane as the motion. In a frame of reference rotating around angular velocity ω, a mass moving with velocity v experiences the force [Woodman 2007]:

$$F_c = -2m(\omega \times v) \tag{2.1}$$

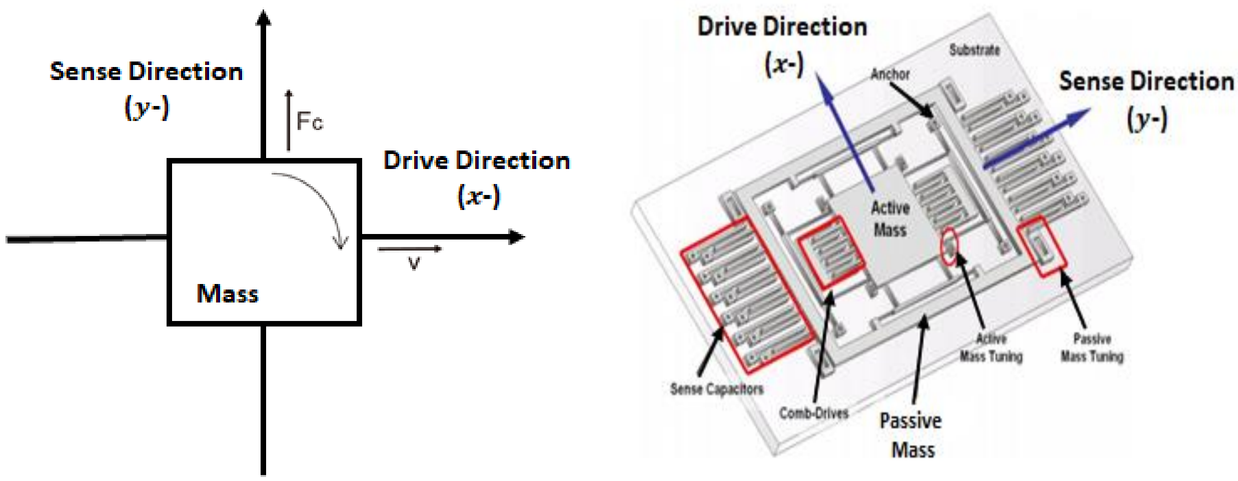

[Coriolis force, modified from Woodman 2007]   [MEMS Structure, modified from Shkel, 2001]

Figure 2.1.5 Mechanical gyroscope

This type of sensor is also known as a vibratory gyroscope, and an example is the tuning fork gyroscope. A tuning fork is made to vibrate at a certain known rate. As the gyroscope is rotated, the Coriolis acceleration applies a force on the plane perpendicular to the plane of vibration. This perpendicular force can then be sensed through various methods to deduce the angular rate. While the gyroscope is rotating the Coriolis force causes a secondary vibration to be induced along the perpendicular sense axis, as shown in Figure 2.1.5. MEMS gyroscopes contain vibrating elements to measure the Coriolis effect. The angular velocity can be calculated by measuring this secondary rotation.

The gyroscopes can provide smooth angular velocity signals. However, their DC components cause drifts in the integral computation. Also, shocks and vibrations can easily affect their measurements [Du et al., 2018]. In addition, the reliability of gyroscopes is affected by harsh working conditions, such as during directional drilling [Zhou et al., 2014].

2.2.3 Magnetometers

The Earth's magnetic field is measured by magnetometers. Magnetometers rely on mechanical motion from the Lorentz force acting on a current-carrying conductor in the magnetic field. Most commercially-avaible magnetometers are fluxgate sensors [Sherrett et al., 2013], as shown in Figure 2.1.6.

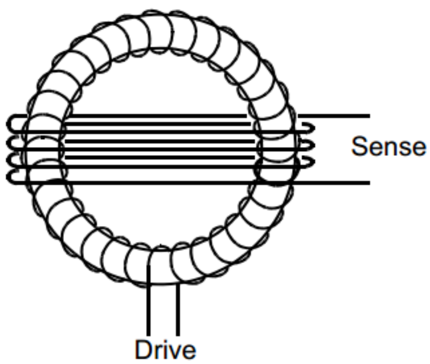

Figure 2.1.6 Fluxgate sensor [modified from Moreland 2002]

Under normal conditions, assuming the sense coil is symmetrical, the coil does not detect the field generated by the toroid because the coil is balanced. An additional external magnetic field can cause an imbalance in the toroid's hysteresis, which results in a net field that is detected by the sense coil. Traditional mechanical inertial sensors are able to provide accurate measurements but at a higher cost; the low-cost market has become increasingly populated by MEMS sensors. All springs, masses, dampers and other components traditionally found in mechanical sensors are now constructed within the same piece of material.

A MEMS magnetometer provides stable geomagnetic strength measurements even though the readings are noisy. Further, magnetic disturbances distort the stable sensor readings of a magnetometer. The errors caused by magnetic disturbances are classified into two types: hard iron and soft iron. Therefore, proper calibrations and occasionally a filter designed for data processing is necessary to maintain the performance of a magnetometer.

2.2.4 Challenges and Compensations

IMUs face many challenges such as gimbal lock caused by a Cartesian rotation system, drift caused by a gyroscope after the integral calculation, and drift caused by accelerometers after the double integral calculation. Researchers have developed many methods to address these challenges. This section reviews a selection of these methods.

<u>Gimbal Lock Compensation (Quaternions)</u>

In 3D, one degree of freedom is lost when there are three gimbal mechanisms where the axes of two of the gimbals are in a parallel configuration. This situation is called a gimbal lock. Quaternion-based computation is critical to sensor fusion because it can solve the gimbal lock problem.

A quaternion is a four-dimensional complex number ($\tilde{q} = [q_1\ q_2\ q_3\ q_4]$) that is used to represent the orientation of a rigid body or coordinate frame of three-dimensional space, where q_1 is the real part and q_2 , q_3 and q_4, are three imaginary parts of the quaternion. An arbitrary orientation of frame B relative to frame A can be achieved through a rotation of angle α around an axis $\hat{R}$ defined in frame A (Figure 2.1.7). The following equation shows the relation between quaternions and a rotation angle:

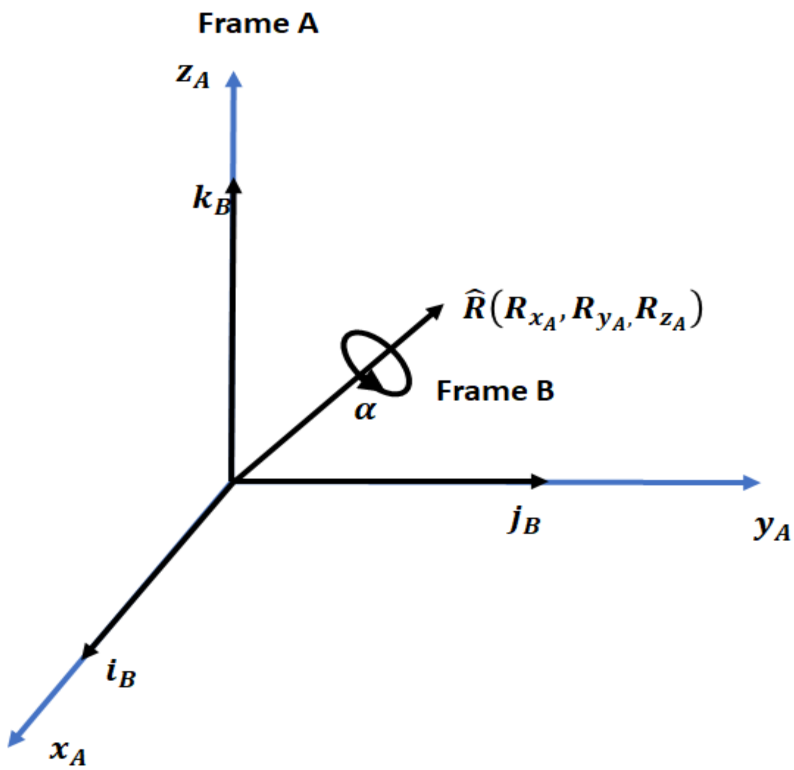

Figure 2.1.7 Quaternion frame (frame B) vs. Cartesian frame (frame A)

$$\tilde{q} = [q_1\ q_2\ q_3\ q_4] = \left[cos\left(\frac{\alpha}{2}\right)\quad R_{x_A}sin\left(\frac{\alpha}{2}\right)\ R_{y_A}sin\left(\frac{\alpha}{2}\right)\ R_{z_A}sin\left(\frac{\alpha}{2}\right)\right] \qquad (2.2)$$

where R_{x_A}, R_{y_A}, and R_{z_A} define the components of the unit vector $\hat{R}$ in x, y and z axes of frame A [Groÿekatthöfer et al., 2012].

Quaternions are more compact and faster to compute than matrix representations of Euler angles. They are often calculated from angular rates obtained from gyroscopes because those measurements can be expressed using four-element row vectors in the body frame using the quaternion representation [Madgwick 2010]. Quaternions are typically used to map matrices, also known as rotation matrices [Diebel 2006]. The kinematics rotation matrix of quaternion is given as follows:

$$\dot{\tilde{q}} = \frac{1}{2}\begin{bmatrix} 0 & -\omega_x & -\omega_y & -\omega_z \\ \omega_x & 0 & \omega_z & -\omega_y \\ \omega_y & -\omega_z & 0 & \omega_x \\ \omega_z & \omega_y & -\omega_x & 0 \end{bmatrix} \tag{2.3}$$

Here, $\omega_x, \omega_y, and\ \omega_z$ are angular velocities obtained from gyroscopes [Feng et al., 2017].

Linear interpolation of quaternions is used for sensor fusion between quaternions obtained from gyroscopes and quaternions derived from accelerometers and magnetometers [Wozniak et al., 2015]. This interpolation is based on features of the gravitational and magnetic fields. There are three steps: 1) update quaternions with a micro-rotation of the angular velocity vector from a gyroscope; 2) normalize the vector of gravity and the geomagnetic fields obtained from an accelerometer and a magnetometer, and then derive the diagonal vectors to compute the quaternions received from accelerometers and gyroscopes; and 3) fuse these two quaternions with linear interpolation [Wozniak et al., 2015].

The gradient descent method of the quaternion is developed parallel to the linear interpolation. This method is executed by the error function derived from the square of the errors obtained from accelerometers and magnetometers. The error function is then minimized with a gradient descent method [Chova et al., 2015].

The quaternion sensor fusion (QSF) design requires the angular rotation representation to be in quaternion form. Consequently, Euler angles ($\beta_{pitch}, \beta_{roll}, \beta_{yaw}$) must be transformed into quaternions; the following equations (2.4) is used for this transformation. [Groÿekatthöfer et al., 2012]:

$$\tilde{q} = \begin{bmatrix} q_1 \\ q_2 \\ q_3 \\ q_4 \end{bmatrix} = \begin{bmatrix} \cos\left(\frac{\beta_{yaw}}{2}\right) cos\left(\frac{\beta_{pitch}}{2}\right) cos\left(\frac{\beta_{roll}}{2}\right) + \sin\left(\frac{\beta_{yaw}}{2}\right) sin\left(\frac{\beta_{pitch}}{2}\right) sin\left(\frac{\beta_{roll}}{2}\right) \\ \cos\left(\frac{\beta_{yaw}}{2}\right) cos\left(\frac{\beta_{pitch}}{2}\right) sin\left(\frac{\beta_{roll}}{2}\right) - \sin\left(\frac{\beta_{yaw}}{2}\right) sin\left(\frac{\beta_{pitch}}{2}\right) cos\left(\frac{\beta_{roll}}{2}\right) \\ \cos\left(\frac{\beta_{yaw}}{2}\right) sin\left(\frac{\beta_{pitch}}{2}\right) cos\left(\frac{\beta_{roll}}{2}\right) + \sin\left(\frac{\beta_{yaw}}{2}\right) cos\left(\frac{\beta_{pitch}}{2}\right) sin\left(\frac{\beta_{roll}}{2}\right) \\ -\cos\left(\frac{\beta_{yaw}}{2}\right) sin\left(\frac{\beta_{pitch}}{2}\right) sin\left(\frac{\beta_{roll}}{2}\right) + \sin\left(\frac{\beta_{yaw}}{2}\right) cos\left(\frac{\beta_{pitch}}{2}\right) cos\left(\frac{\beta_{roll}}{2}\right) \end{bmatrix} \tag{2.4}$$

Equations 2.5-2.7 shows the transformation from quaternions to Euler angles.

$$\beta_{roll} = arctan(2q_3q_4 + 2q_1q_2, 2q_1^2 + 2q_4^2 - 1) \tag{2.5}$$

$$\beta_{pitch} = -arcsin(2q_2q_4 - 2q_1q_3) \tag{2.6}$$

$$\beta_{yaw} = arctan(2q_2q_3 + 2q_1q_4, 2q_1^2 + 2q_2^2 - 1) \tag{2.7}$$

<u>Gyroscope Drift Compensation (Complementary Filter)</u>

Combined with accelerometers, a complementary filter is a powerful, easily-applied method of removing the drift that results from gyroscope integral calculation. As shown in Figure 2.1.8, the complementary filter is a combination of low-pass and high-pass filters. The most important feature is the light calculation load, which allows the complementary filter to be implemented on cheap, simple equipment without the performance deteriorating significantly [Quoc et al., 2015].

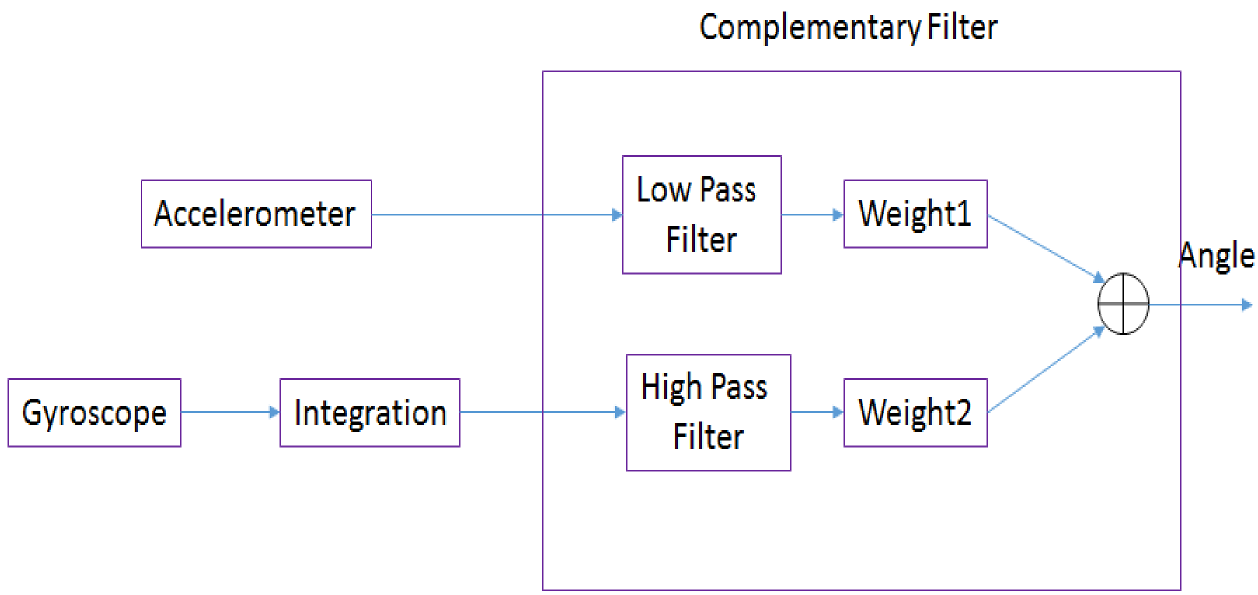

Figure 2.1.8 Structure of complementary filter for tilt angle estimation

Nonlinear systems require complementary nonlinear filters [Zlotnik et al., 2018]. A complimentary nonlinear filter combines accelerometer output for low-frequency motion estimations and an integrated gyroscope output for high-frequency estimations to estimate motion [Koksal et al., 2019]. Using an object's angle rate and acceleration combined with the relation between angular rate and angle in the different dynamic model, the complementary filter can adequately estimate the motions of the object [Bourke et al., 2008].

In addition, a combination of a discrete low-pass filter and a complementary nonlinear filter has been proposed to estimate attitudes. The complementary filter, which is introduced in Vasconcelos (2009), estimates attitudes in Euler angles without quaternion designs.

<u>Euler Angle Compensation (Azimuth of Magnetometer)</u>

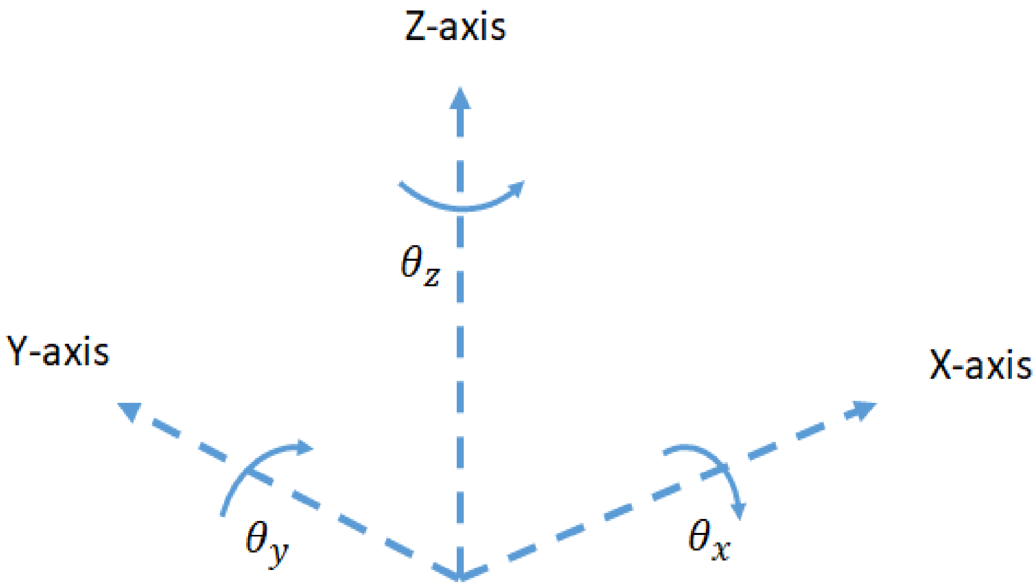

Figure 2.1.9 Euler angle coordinates

Using gravity signals, we can compute the pitch and roll angles. The azimuth angle is determined by calculating the magnetometer outputs. With the accelerameter outputs, which are gravitational acceleration components (g_x, g_y, g_z), the pitch and roll angles can be obtained using the following [Yuan et al., 2015]:

$$\begin{cases} \theta_y = tan^{-1}(\frac{g_x}{\sqrt{g_y^2+g_z^2}}) \\ \theta_x = tan^{-1}(\frac{g_y}{\sqrt{g_x^2+g_z^2}}) \end{cases} \tag{2.8}$$

where g_x, g_y, and g_z are gravity measurements on the axes of x, y and z of an accelerometer. The outputs of the accelerometer are read as total accelerations, including the dynamic accelerations of movement and gravity. As the SMS moves in subsurface environments, its body system is in a situation of low dynamics or moves at a constant velocity. There are no sharp accelerations or decelerations in our tests.

The inclination and roll angles are used to compensate for rotation, including for the azimuth angle computation using a magnetometer. Only the horizontal elements of the geomagnetic field intensity contribute to the azimuth calculation. After roll and inclination rotation, the magnetometer frame is at an angle to the geomagnetic field frame. The rotational relationship between the values (B_{sx}, B_{sy}, B_{sz}) measured by a magnetometer in the sensor coordinates and the magnetic values (B_x, B_y, B_z) in the Earth's coordinates is expressed as follows:

$$\begin{bmatrix} B_x \\ B_y \\ B_z \end{bmatrix} = \begin{bmatrix} cos\theta_y & 0 & -sin\theta_y \\ sin\theta_x sin\theta_y & cos\theta_x & -sin\theta_x cos\theta_y \\ sin\theta_x cos\theta_y & -sin\theta_x & cos\theta_x cos\theta_y \end{bmatrix} \begin{bmatrix} B_{sx} \\ B_{sy} \\ B_{sz} \end{bmatrix} \tag{2.9}$$

Equation 2.9 shows the roll and pitch compensation matrix that converts the magnetometer frames to geomagnetic magnetic frames. The gyroscope also needs a similar rotation compensation. The computations of pitch and roll with gravity elements, which are measured by the accelerometer, is a crucial step for angular estimations.

The Earth's magnetic field (EMF), as measured at any point on the Earth's surface, is a combination of several magnetic values generated by various sources. We can describe the geomagnetic field by measuring intensity and two angles (declination and inclination) or three orthogonal components (X, Y, and Z towards geographic north, east, and vertically down, respectively). Magnetometers measure the vector components of the magnetic field. With the features of EMF, the azimuth can be obtained using magnetometers.

The geomagnetic field $B(B_x, B_y, B_z)$ has a fixed component B_h on the horizontal plane pointing to the Earth's magnetic north. This component can be calculated using the magnetic sensor sensing axes B_{sx} and B_{sy}. The azimuth angle is then calculated using equation 2.10 [Mansuclal 2010]:

$$\theta_z = tan^{-1}(B_{sy}/B_{sx}) \tag{2.10}$$

Equation 2.10 outputs an azimuth angle and is only correct if the sensor measurements of B_{sx} and B_{sy} are on a horizontal plane parallel to the Earth's surface. In the situation that the sensor is tilted, the values of B_{sx} and B_{sy} are not correctly measured and the azimuth computed by the above equation includes an error term [Mansuclal 2010]. Equation 2.10 also implies that the estimated magnetic azimuth is affected by any disturbance or perturbation in the horizontal field components. Consequently, local magnetic elements control the magnetic azimuth estimation process [Ali, 2013].

2.3 Sensor Fusion Methodology

Many issues must be addressed to design a sensor fusion system. Key considerations include the sensor types and the sensors' accuracy, distribution, data association, and management [Kalandros et al., 2004]. Furthermore, it is important to design a sensing system that is specific to its target at the same time eliminating sensor uncertainty [Helm et al., 2010].

The varying environmental conditions and the limitations of the sensors themselves can contribute to the above-mentioned problems. Proper design of a sensor fusion should consider reducing noise and the uncertainties of the sensors, be modeled on external environments, and selecting the proper algorithm structure and design. Applicable knowledge bases used to develop sensor fusions are theories of control, signal processing, artificial intelligence, probability, and statistics [Luo et al., 2011].

There are many design methods of sensor fusion, most of which can be classified into two categories: a stochastic approach and artificial intelligence (AI) [Pettersson et al., 2005]. In stochastic methods, Kalman Filters (KFs) and their extensions [Extended Kalman Filters (EKFs) and Unscented Kalman Filters (UKFs)] are the foundations of the fusion design [Fang et al., 2017]. KFs successfully remove sensor uncertainties and produce accurate information; however, the design depends on a priori-information on covariance matrices [Basso et al., 2017].

Another important filter is the particle filter (PF), also is called Monte-Carlo filter. PF methodology is utilized to solve hidden Markov chain and nonlinear filtering problems [Creal 2011]. Similar to EKFs and UKFs, PFs are a good candidate for the design of a nonlinear filter.

In AI approaches, artificial neural networks (ANNs) and fuzzy logic (FL) are typically used to judge the weights between different sensors under certain rules. They are utilized to improve the performance of methods designed based on probability and statistics, such as KFs [Chang et al., 2010].

2.3.1 Kalman Filters

Fusing an accelerometer and a gyroscope to obtain inclination angles or a magnetometer and a gyroscope to obtain azimuth angles removes drift in the integral calculation of the gyroscope signal. The accelerometer and magnetometer signals are expected to be noisy; however, the noises do not cause the gravity and magnetic field readings from accelerometers and magnetometers to change over an extended period. The integral computation of a gyroscope's measurements is only accurate in a short time interval, but the signal from a gyroscope has a higher signal to noise ratio (SNR) than the signal from a magnetometer. Both advantages of these three kinds of sensors can be integrated using a KF to estimate orientation angles [Brigante et al., 2011]. The KFs can also fuse IMUs (usually accelerometers) with correction sensors, such as GPS and cameras. to estimate positions [Du 2010; Alatise et al., 2017; Kim et al., 2016]. A drawback of applying KFs in sensor fusion is the heavy computational load. However, the technical development of microcontrollers has removed this drawback. For example, KFs with around 30 Hz can be applied to a low power STM32L053 microcontroller with a processing time of 1.18 milli-seconds in a 32 MHz central processing unit (CPU), and the CPU usage is only 3.8% [Valade et al., 2017].

<u>Adaptive Covariance Matrix Q & R Design</u>

The performance of a KF highly depends on the proper design of Q & R (covariance matrices). An automatically-tuning KF can improve robustness by calculating the covariance matrices of noise in real time using information obtained from the difference between predicted values and measurements [Akhlaghi et al., 2012]. Many adaptive covariance matrix design methods have been reported. For example, the covariance matrix associated with external acceleration is estimated to adaptively tune the KF gain [Widodo et al., 2016]; for better performance, the KF can be improved by updating the Q matrix in real time [Liu et al., 2015]; Using deep neural networks can also dynamically adapt the Q matrix of a KF during the training process [Brossard et al., 2019]. The measurement noise covariance distribution can also be approximated through finite samples to update the R matrix [Assa et al., 2017].

<u>Quaternion KF</u>

The quaternion KF (QKF) can be designed to estimate project behaviors using quaternions for tracking orientation to avoid the gimbal lock problem and to provide efficient computation [Smith et al., 2006]. Also, a QKF can be customized to be used for various applications and to test different algorithms for increasing performance. For example, a QKF is used as a smoother for gyroscopes and accelerometers for orientation fusion [Makni et al., 2016]; Both quaternion and gyroscope biases are built into one error model to improve QKF's accuracy [Madgwick 2010; Sadaghzadeh et al., 2014]; QKF is used to develop indoor position estimations [Hasan et al., 2013].

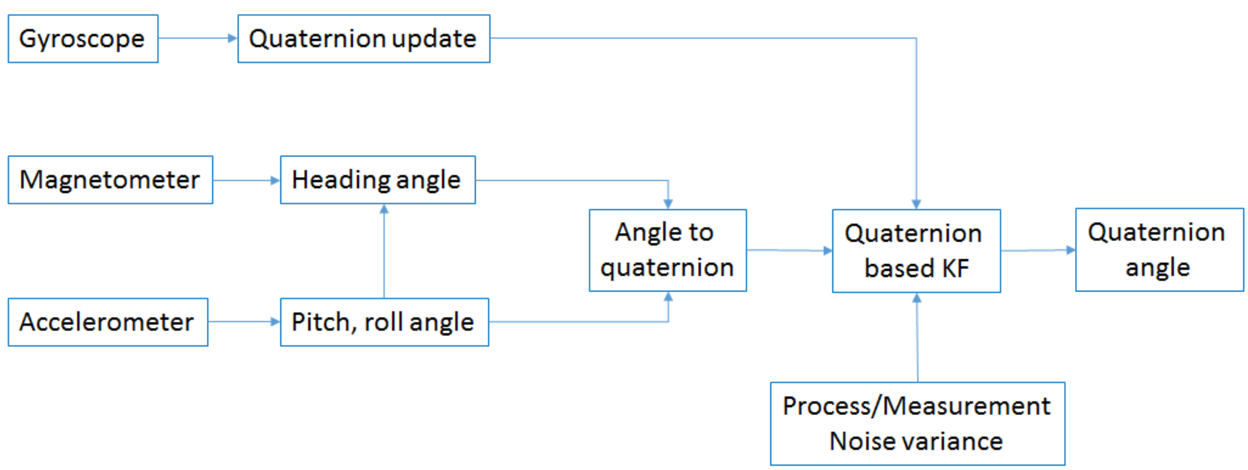

Figure 2.1.10 Structure of quaternion-based KF design

For a QKF design, the basic idea is that the Euler angles are first converted into quaternions, and then the quaternions are fed into the KF as shown in Figure 2.1.10.

Extended and Unscented KF

An EKF is a nonlinear filter [Li et al., 2017], but the Jacobian matrix is used instead of the nonlinear system model for calculating the covariance matrices [Julier et al., 1996]. An EKF is employed to estimate orientations due to its better nonlinear filtering performance [Khot et al., 2006]. EKF can also be applied to fuse accelerometers and optical sensors to obtain a moving object's positions [Hyun 2010]. In this article, accelerometer data is used to calculate displacement through double integral calculation. An optical navigation system is used to take continuous snapshots of the surface and compare the images to determine the distance traveled to reduce the drift caused by the integral calculation. The optical navigation sensor can be applied as an odometer [Hyun 2010]. Further, the frequent outages problem can be overcome using accelerometers with an EKF.

Random sigma points are used instead of system models to further increase the nonlinear performance of a KF; this new KF is called an unscented KF (UKF). It is not necessary to compute the Jacobian matrix for a UKF, and therefore, the truncation errors are reduced [Zhou et al., 2019]. A UKF can also be applied to determine the pitch and roll angle of high-speed objects such as projectiles [Wang et al., 2010]. In this research, the change in the range of motion is extensive and includes the rolling rate range of a rocket ranging from 1 r/s to 70 r/s. In addition, five accelerometers are employed for sensing. A UKF can also be applied for aerial vehicle positioning to fuse GPS and IMU [Zhang et al., 2005]. However, position estimations of environments with insufficient GPS is challenging. Combining vision information with IMUs can solve this problem. For example, a UKF is proposed to estimate the movement of a trolley using a forward-looking camera, a three-axis airspeed sensor and an onboard IMU [Gaedeke et al., 2014].

Combination of KFs and Other Methods

A KF design can be modified in many ways based on the application details. A filter structure, including pre-filter (complementary filter) and post-filter (KF), can be used to solve the problems of bandwidth and delay [Ghanbari et al., 2015]. Also, a KF can be combined with a direction cosine matrix (DCM) for a navigation application [Choukroun et al., 2008]. The DCM is an algorithm for motion and orientation estimations that updates a 3x3 matrix defined by the changing relative angles between the subject and ground reference frames [Ali 2013]. The algorithm works effectively only under low-speed situations without magnetic disturbances. Therefore, designing a KF to detect and remove errors from magnetometers [Feng 2017] can increase the DCM's robustness to magnetic disturbances.

A KF-based fusion design requires an accurate mathematical model of the object and knowledge of predefined errors. Many cases suffer from complex stochastic error characteristics that are difficult to model [Bistrovs et al., 2011]. The nonlinearities and IMU unknown bias uncertainties result in the reduced performance of KFs. Researchers developed hybrids of KFs and intelligent methods to solve this problem. For example, hybrid a KF with a fuzzy neural network (FNN) is used to estimate trajectories for implementing at touch interface [Li et al., 2019]. The KF output is fused with GPS to estimate positions, and ANN compensation is used to refine the results and to reduce the nonlinear error affection [Chang et al., 2010]. GPS data and inertial sensor data can be fused with a KF; the output of the KF is then compared with a radial basis function neural network (RBFNN) to estimate the error so that the result of the KF can be corrected [Xia et al., 2009].

2.3.2 Other Sensor Fusion Methodologies

Rule-based systems using human expert knowledge are employed to fuse GPS and accelerometer sensors data [Bistrovs et al., 2010]. For example, ANFIS can be designed to augment a KF creating a corresponding nonlinear error model to minimize IMU position errors [Noureldin et al., 2009]. This design can predict position errors during a GPS outage to enhance overall system accuracy. In addition to ANFIS, fuzzy logic can also be applied to design mobile robot tracking fusion by fusing the information from vision systems, laser radar, IMUs and speed information [Subramanian et al., 2009]. In addition, since the accuracy of GPS signals is affected by trees and other obstructions, the reliability of the machine vision is influenced by soil color and changing light levels. Further, IMUs suffer from drifting, and therefore, fuzzy logic fusion design is applied to reduce the errors from GPS, machine vision and IMUs [Shen et al., 2007].

Intelligent fusion methods, such as the neuro-fuzzy approach, can also be employed to design a GPS-free position correction that is based on a camera and an IMU for an indoor moving object [Casanova et al., 2011]. In this neuro-fuzzy design approach, a camera is used to capture movements, which means that the movements can be evaluated by measuring the displacement of selected image points in consecutive frames (optical flow). All measurements obtained from the IMU and camera are fed into the neuro-fuzzy system to estimate final positions. Furthermore, for indoor positioning, PFs have been designed. For example, a PF is used to extend the typical wireless local area network (WLAN)-based indoor positioning systems by integrating a MEMS accelerometer and map information [Wang et al., 2007]. Since indoor environments are GPS outage, global navigation satellite system (GNSS) receivers are forced to operate under more demanding conditions in receiving GPS signals than outdoor applications [Vecchione et al., 2010]; therefore, an indoor positioning reference system such as WLAN is necessary.

2.4 Summary

This chapter reviews the literature regarding subsurface sensing technology applications, MEMS-based IMUs, and sensor fusion methodologies. First, inclinometers and directional drilling survey sensors and their applications are discussed. Then, working principles, challenges, and basic compensations of IMUs are described. In the sensor fusion methodology section, fusion methodologies with MEMS IMUs (accelerometer, gyroscope, and magnetometer) are reviewed. The advantages and limitations of the most frequently used fusion algorithms based on MEMS IMU sensors are also summarized. The benefits of implementing sensor fusion based on IMUs are shown by presenting application examples in various fields. IMU-based sensor fusion has become a fundamental technology to develop an AI system. Sensor fusion systems with multiple sets of sensors can theoretically provide better estimations compared with the results from single sensor systems.

Subsurface sensing procedures often experience magnetic and shock disturbances. However, current sensor fusion methods have difficulty dealing with the unknown magnetic distortions and drifts are caused by shocks in the integral calculation because traditional methods focus on using external correction signals to remove the magnetic disturbances and drifts. All external correction signals that are derived from GPS or other alternative sensors, such as Wi-Fi, camera, or radio, are impossible to implement in subsurface environments. Consequently, it is necessary to develop sensor a fusion technology with MEMS IMUs that does not suffer from these problems.

CHAPTER 3. EXPERIMENTAL SETUP

The proposed sensor is called a subsurface monitoring system (SMS). Subsurface industry activities such as directional drilling need accurate positioning techniques to provide safe and efficient working conditions. SMS is designed to quantify changes in orientation angles and positions by measuring the movements of the SMS's instrument itself. Specifically, the SMS is expected to reduce the effect of magnetic and shock disturbances using a physical structure configuration (hardware) and fusion methods (software). This chapter describes the design details of the SMS and a test rig, which is used for calibration and testing. The calibration methods of magnetometers and compensation methods of accelerometers are also included.

The measurements of motion are expected to have no bias errors, though the measurements may contain noise. The setup of the rig controls movement by pre-setting the track paths and speeds. The reference values are derived from the encoders, which are used in the result analysis. These experiments can simulate subsurface tilting movements, while IMUs record the corresponding measurements of the tilt movements.

3.1 Configuration Design of Subsurface Monitoring System (SMS)

Two sets of IMUs and related circuits are included in the SMS. The IMUs (ADIS 16448) take the measurements since the SMS cannot obtain correction assistance from GPS in a subsurface environment. As we developed the SMS, we encountered several problems. For example, we need to reduce the influence of the magnetic disturbances caused by iron ores.

Magnetic disturbances can be reduced in many ways, such as increasing the distance between the IMUs and the disturbances [Abbott et al., 2007]. To find the distance relationship between the sensor and the magnetic disturbances for the SMS design, we conducted magnetic interference effect tests (Figure 3.1.1). Six magnets (the value was about 4.16×10^5 nT with a 50mm distance to the sensor on an aligned collinear axis) were stacked in line and then taped onto one of the test stand's sliders. The justable table (Figure 3.1.1) was tuned to ensure the magnets were exactly collinear with one axis of the IMU to prevent the misalignment of the IMU.

The results are presented in Figure 3.1.2; as shown, distance is a crucial factor in reducing the influence of magnetic disturbances. When one axis (for example, the x_s axis) of a magnetometer is pointed at the magnetic source, that axis is most affected; the other axes (y_s, z_s) are also affected, but by a smaller deviation. For all axes, if the distance is sufficiently increased, the effect of the disturbance significantly decreases. Consequently, the SMS should be designed with a configuration that allows for a long enough distance between the two IMUs so that the IMUs are disturbed while the sensor system passes through the iron ores.

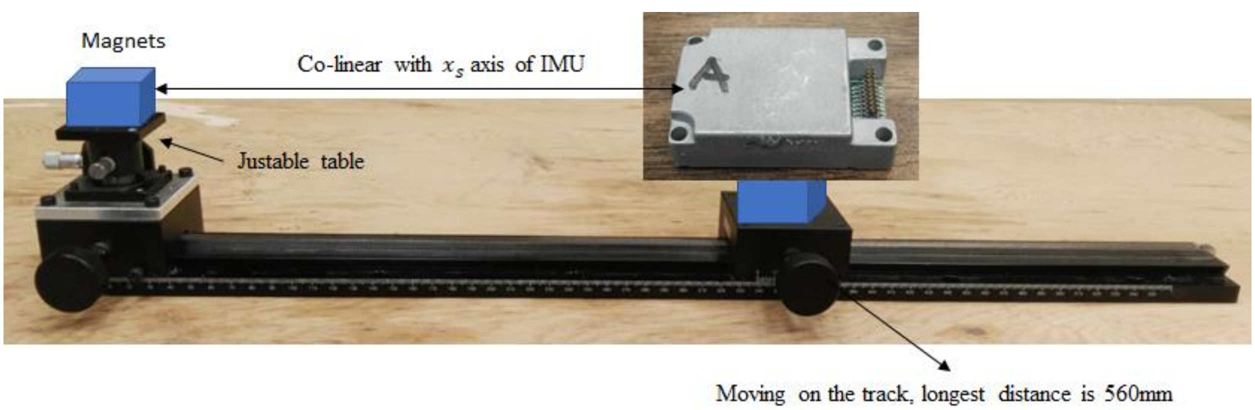

Figure 3.1.1 IMU magnetic disturbance test

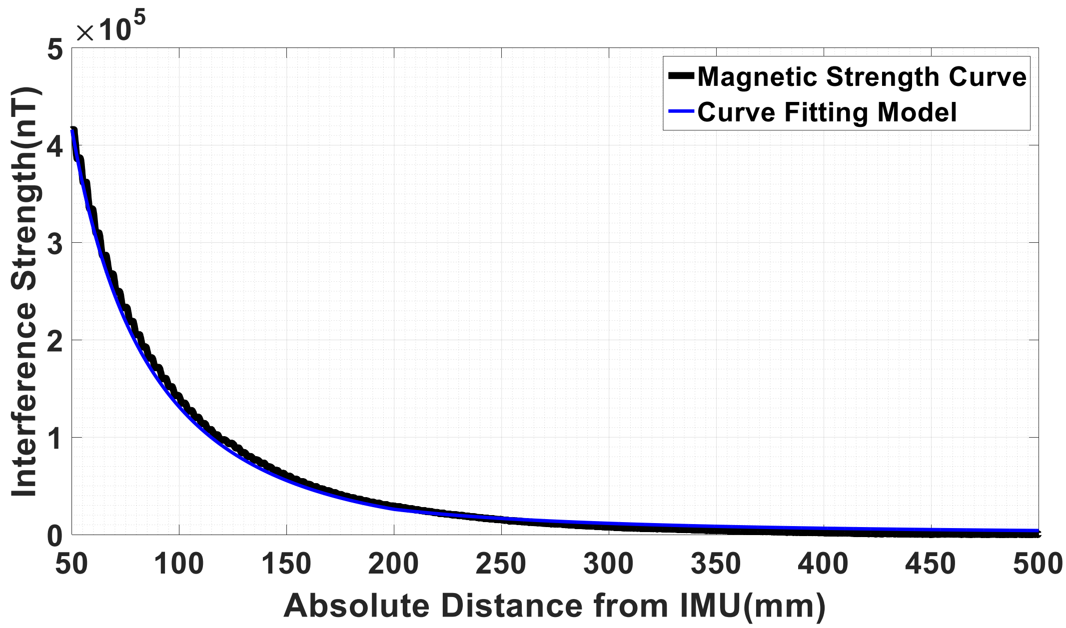

Figure 3.1.2 Experimental results, relation between magnetic disturbance strength and distance

The solid black line in Figure 3.1.2 depicts the magnetic disturbance magnitude-distance relationship. When test data in Figure 3.1.2 are used for the curve fitting model, a relation between the magnitude and distance can be approximated using the following equation:

$$|B_n| = D^{-h(s)} \times 4.16 \times 10^5 \tag{3.1.1}$$

where,

$$\begin{cases} h(s) = ks + 1.5 & D < 200mm \\ \quad h(s) = 2 & D > 200mm \end{cases} \tag{3.1.2}$$

where $s \in (0{,}1855)$ and $k = 2.7 \times 10^{-4}$. The curve fitting model is depicted in Figure 3.1.2 using a solid blue line. The relation between the magnitude and distance of the x_s, y_s, and z_s axes is shown in the Table 3.1.1.

Table 3.1.1 Magnitude and distance relation on the x_s, y_s, and z_s axes

Distance(mm)	x_s(nT)	y_s(nT)	z_s(nT)
50	402493	34403.2	99358.6
100	139773.4	8076.9	20851.6
150	59421.7	2242.5	6422.9
200	28934.1	111.8	2948
250	15191.8	-159.9	1346.4
300	7712.9	-302.9	917.4
350	4280.9	-874.9	431.2
400	1835.6	-460.2	474.1
450	405.6	-245.7	16.5
500	-180.7	-217.1	-455.4

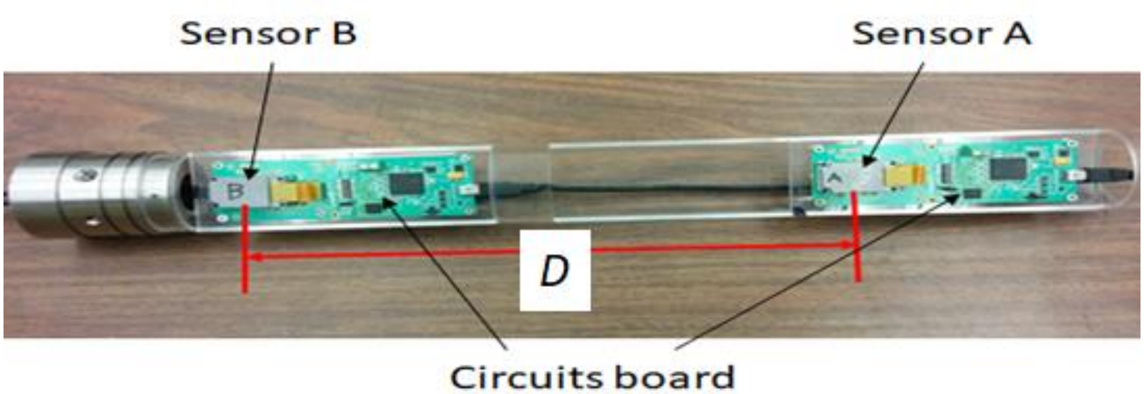

Figure 3.1.3 SMS configuration

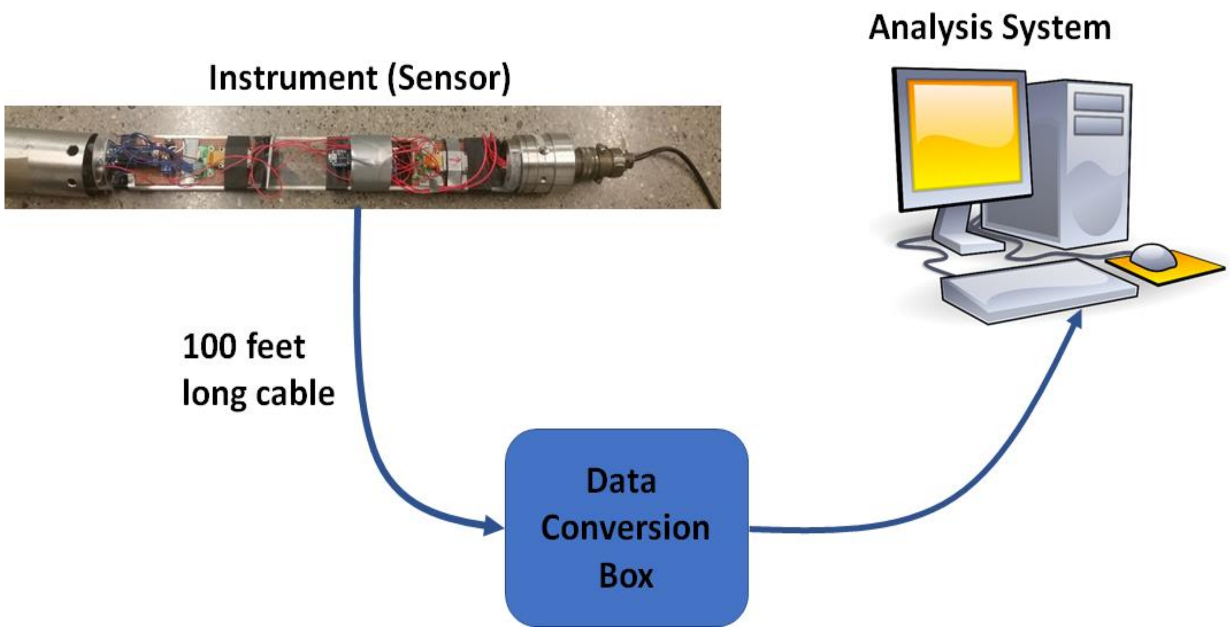

Figure 3.1.4 Sensor data flow

The proposed sensor system provides orientation angles using two redundant sets of IMUs. Each IMU set has gyroscopes ($\times$ 3), accelerometers ($\times$ 3), and magnetometers ($\times$ 3) located on the x_s, y_s, and z_s axes to determine its orientation. Also, both IMUs are configured with aligned directions, and they are placed with a known distance D apart as shown in Figure 3.1.3. The newly-designed sensor system consists of the following sections: the instrument, the data conversion system including data loggers, and the analysis system. The data flow of these sections is detailed in Figure 3.1.4. The instrument device (the sensor) is the physical device that records data while buried in the ground. It includes the IMUs, microcontrollers, and communication modules. The instrument sends the recorded measurements to the data conversion system.

The communication modules are necessary because signals sent along USB cables are limited by distance. The range of data transfers between a computer and instrument using a USB cable is only several meters [Norton 2009]. Consequently, USB cables cannot be used for subsurface data communication. Therefore, industry data conversion methods are necessary to transport data over long distances. Microcontrollers must first convert the data to TTL signals (RS485 standard) before the data is transported. The microcontrollers act as an intermediary between the IMUs and the conversion system.

3.2 Testing and Calibration Rig

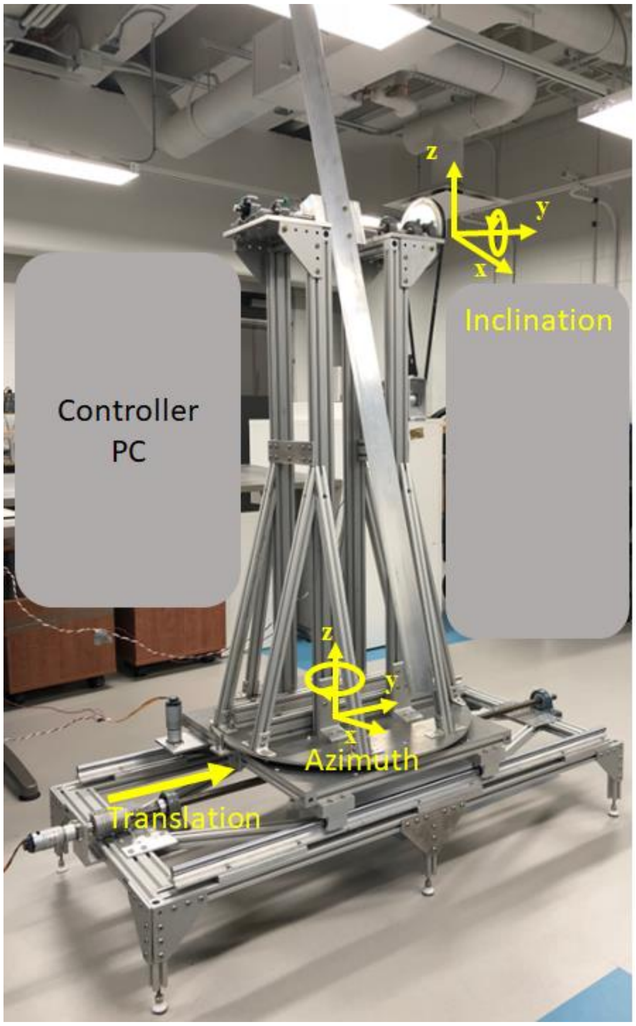

Figure 3.2.1 Test rig

The test rig consists of a two-axis turntable riding on a linear moving stage, as shown in Figure 3.2.1. Three encoders that are located on three DC drive motors are used to track the movements of the rig. This test rig simulates inclination, azimuth, and translational movements. The host control PC reads in encoder signals and sends out command signals to different motors. The desired motion paths are programmed through the controller, which performs the necessary calculations and transmits the commands to the motors. The command values of the corresponding motions are calculated based on the collected feedback information.

3.3 Calibrations

3.3.1 IMU Errors

An IMU navigation system consists of three axes of accelerometers, gyroscopes, and magnetometers. The triad of axes defines a single orthogonal 3D frame. An accelerometer and a magnetometer sense acceleration and magnetic strength, respectively, along one axis, while each gyroscope measures the angular velocity around the same axis.

When used in a navigation system, commercial IMUs on their own perform poorly, because of errors in the IMUs' measurements. In general, IMU errors can be classified as biases, scale factor errors, or misalignment errors [Ferguson 2015]. IMU biases in accelerometers, gyroscopes, and magnetometers are errors present in the measurements regardless of the real information, such as the forces, angular rates, or magnetic strength, obtained by the sensors. IMU sensors are also affected by scale factor errors, which describe how well the output of the sensor corresponds with an input. Scale factor errors contribute to IMU displacement measurement errors only when the IMU is moving [Looney 2010]. Misalignment errors describe the angular difference between each sensor’s axis of rotation and the system-defined navigation reference frame [Looney 2015], as shown in Figure 3.3.1. In this diagram, the three solid black lines represent the three axes in the navigation frame, and the θ-based angles represent the misalignment errors between the navigation frame and sensor body axes. These IMU errors can be removed using calibration methods [Pasquale 2010; Hemanth et al., 2012; Yang et al., 2017; Ladetto et al., 2002].

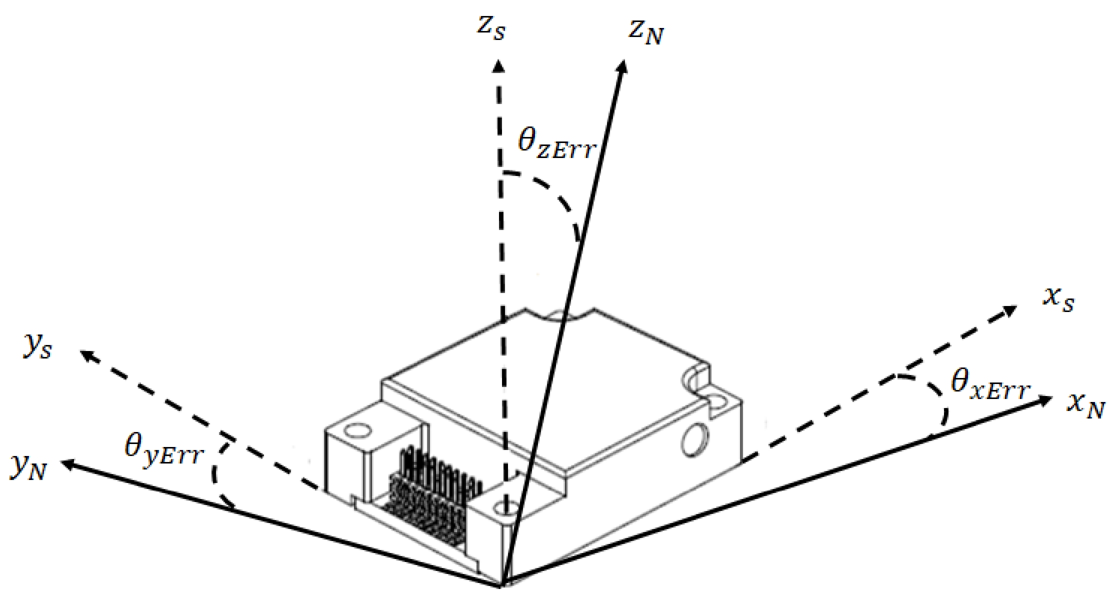

Figure 3.3.1 Sensor body axes (x_s, y_s, z_s) and navigation sensing axes (x_N, y_N, z_N)

The noises that are included in accelerometers, gyroscopes, and magnetometers are classified into white noise and pink noise $(^1/_f)$ [Woodman 2007; Patonis et al., 2018; Denoual et al., 2014; Butta et al., 2012]; here, f denotes frequency. However, for magnetometers used in this research, there is no specification about the noise type listed on the data sheet. According to the test conditions, the noise of the magnetometer is treated as pink noise.

In addition, magnetometers suffer from hard and soft iron errors, which in most cases significantly affect the navigation performance. A tumble test of the magnetometer in an ideal 3D environment without any hard or soft iron disturbances shows a perfect sphere with a center at (0,0,0) and a radius equal to the total magnetic field strength at the test location:

$$B_x^2 + B_y^2 + B_z^2 = B^2 \tag{3.3.1}$$

Table 3.3.1 IMU noise specification [ADIS 16448]

		IMU		
Gyroscope	Parameter	Conditions	Value	Unit
	Angular Random Walk	1σ	0.66	$°/\sqrt{hr}$
	In-Run Bias Stability	1σ	14.5	$°/hr$
	Output Noise	RMS	0.27	$°/sec$
Accelerometer	Velocity Random Walk	1σ	0.11	$°/\sqrt{hr}$
	In-Run Bias Stability	1σ	0.25	mg
	Output Noise	RMS	5.1	mg
Magnetometer	Output Noise	RMS	2.4	$mgauss$

Under real conditions, however, the generated center is offset because of the presence of hard iron, which interferes with the permanent magnets in the sensors. Mathematically, this error is equivalent to zero-deviation [Liu et al., 2014]:

$$B_{Hiron} = [B_{xHiron} \quad B_{yHiron} \quad B_{zHiron}]^T \tag{3.3.2}$$

The hard iron error is modeled as follows:

$$(B_{sx} - B_{xHiron})^2 + \left(B_{sy} - B_{yHiron}\right)^2 + (B_{sz} - B_{zHiron})^2 = B^2 \tag{3.3.3}$$

Here, $\left(B_{sx}, B_{sy}, B_{sz}\right)$ represent magnetometer measurement values on three axes. If the soft iron disturbances caused by the magnetism-inducing interaction of ferromagnetic compounds with an external field exist, the perfect sphere would become an ellipsoid. This change in shape means soft iron changes the intensity and direction of the sensed magnetic field. The soft iron effect can be modeled as a three by three matrix [Renaudin et al., 2010]:

$$B_{SOiron} = \begin{bmatrix} B_{SOxx} & B_{SOxy} & B_{SOxz} \\ B_{SOyx} & B_{SOyy} & B_{SOyz} \\ B_{SOzx} & B_{SOzy} & B_{SOzz} \end{bmatrix} \tag{3.3.4}$$

The soft iron error can also be modeled as follows to image the error easily:

$$\left(\frac{B_{sx}}{B_{SOxx}}\right)^2 + \left(\frac{B_{sy}}{B_{SOyy}}\right)^2 + \left(\frac{B_{sz}}{B_{SOzz}}\right)^2 = B^2 \tag{3.3.5}$$

The complete error model of hard and soft iron is as follows:

$$\left(\frac{B_{sx} - B_{xHiron}}{B_{SOxx}}\right)^2 + \left(\frac{B_{sy} - B_{yHiron}}{B_{SOyy}}\right)^2 + \left(\frac{B_{sz} - B_{zHiron}}{B_{SOzz}}\right)^2 = B^2 \tag{3.3.6}$$

Equation 3.3.6 shows the relationship of hard and soft iron to the magnetic sphere. The center of the sphere has an offset value caused by the hard iron. In contrast, the soft iron factors change the shape of the sphere to an ellipse.

3.3.2 Calibration and Compensation Procedures

Calibrating IMUs involves removing as many error sources as possible before deploying the unit for navigation. Techniques such as the six-position static test for accelerometers and angular rate tests for gyroscopes can be used to remove errors such as bias offsets and scale factor errors. The details of how to calibrate hard and soft iron errors for magnetometers are described below.

<u>2D Calibration for Lab Test</u>

Rotating a magnetometer in a sphere and collecting data from all three axes is a traditional method to calibrate a magnetometer in 3D. However, to form a sphere, a sensor is required to rotate a large number of circles, which is not feasible in the lab test rig in this research; therefore, simplifying 3D magnetometers has become a popular research topic [Hemanth et al., 2012; Yang et al., 2017; Ladetto et al., 2002]. For lab tests, a simplified approach that only calibrates in the horizontal plane is applied during each linearized inclination angle interval. Considering the rotation, the horizontal components of the sensor measurements are calculated using a 3D rotation matrix:

$$\begin{bmatrix} B_{sxT} \\ B_{syT} \\ B_{szT} \end{bmatrix} = \begin{bmatrix} sin\theta_y & 0 & cos\theta_y \\ sin\theta_x sin\theta_y & cos\theta_x & -sin\theta_x cos\theta_y \\ cos\theta_x cos\theta_y & -sin\theta_x & cos\theta_x sin\theta_y \end{bmatrix} \begin{bmatrix} B_{sx} \\ B_{sy} \\ B_{sz} \end{bmatrix} \tag{3.3.7}$$

Using Equation 3.3.7, the 3D calibration can be simplified into 2D (Figure 3.3.2). The magnetometer starts from an inclination angle of 0 degrees and then rotates 90 degrees. Simultaneously, the magnetometer rotates on the azimuth direction from 0 to 90 degrees, which is shown with a green dashed line in Figure 3.3.2 (this path is also used as the test track). Then, the azimuth angle continues to rotate a full 360 degrees with a constant inclination angle (90 degrees, horizontal to the ground); the magnetometer finally stops at the yellow point in the figure.

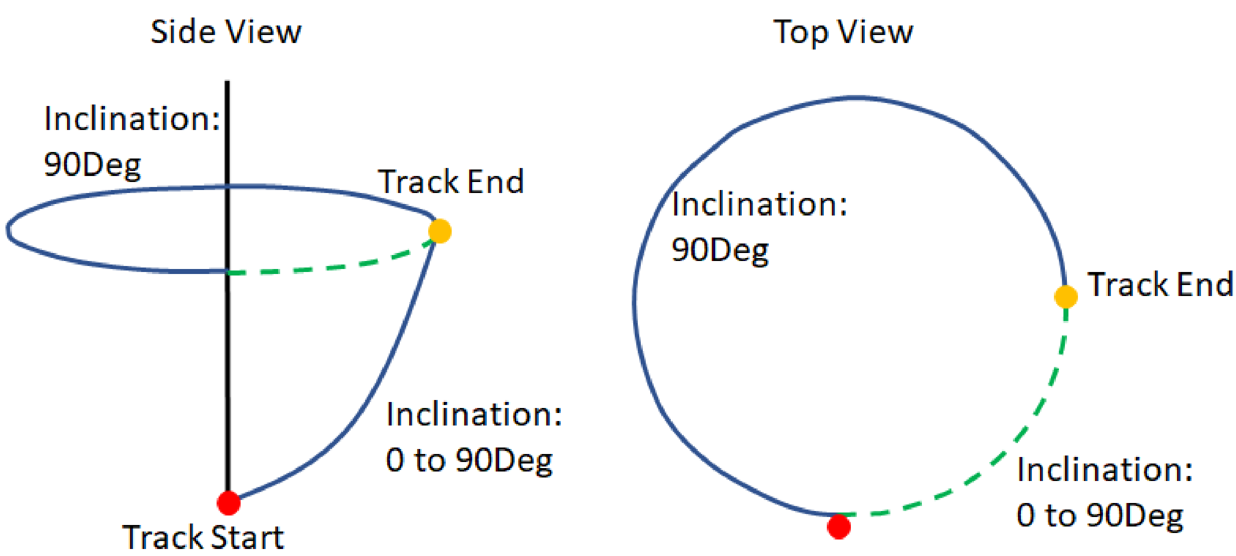

Figure 3.3.2 Magnetometer calibration track

During the rotation process, the sensor axes need to be converted to earth coordinates using Equation 3.3.7, and in this research, the magnetometer is only used to calculate the azimuth angle. Therefore, 2D calibration based on the data sets of B_{sxT} and B_{syT} is sufficient. A full circle of 2D rotation can be obtained as shown in Figure 3.3.2; after the 2D calibration (removal of hard and soft iron), a set of reference magnetic measurement data is obtained. This reference data is then compared to the test track data (with inclination), and the scale factors are calculated.

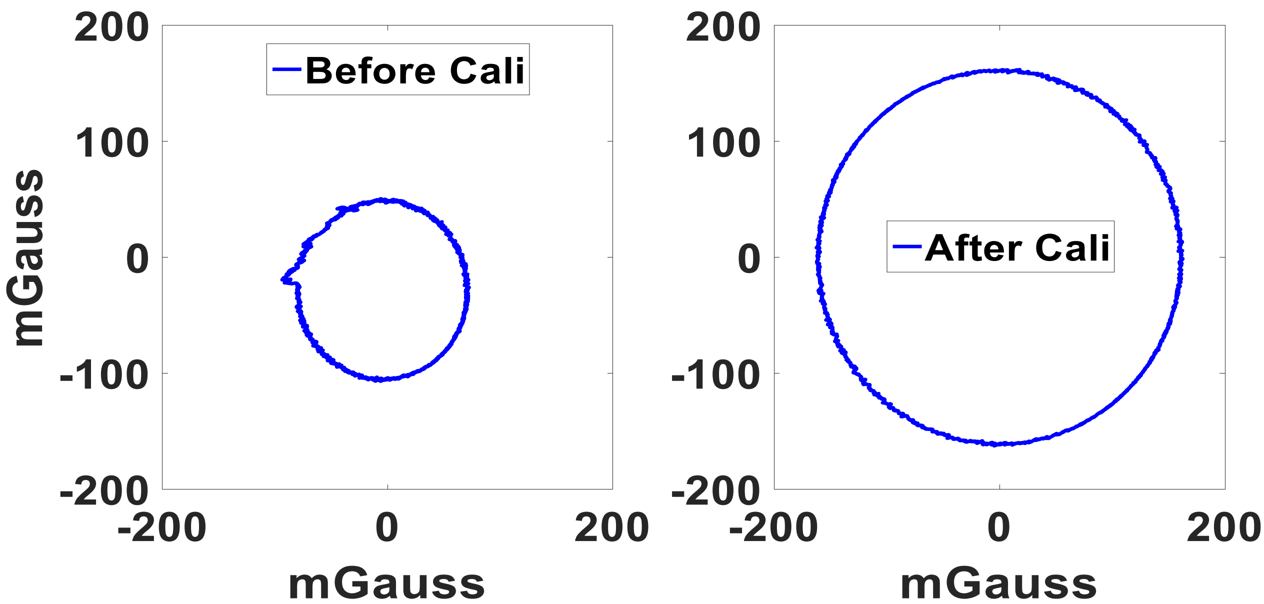

Figure 3.3.3 Calibration of magnetometer (2D)

Sensor calibration needs to be completed during data measurement, particularly with magnetometers. Figure 3.3.3 shows the results of 2D calibration for the magnetometers with the test rig. The values of a horizontal magnetic field of strength B_h are different depending on the location. The values can be obtained from the database of International Geomagnetic Reference Field. The magnetic field parameters B_h at the University of Calgary, the location used in this research, is 16115 nT [Geomagnetism Canada]. From the values of the magnetic field at the university, the shape of the magnetic circle after calibration, shows that the magnetometers are well calibrated.

3D Calibration for Field Tests

The hard iron error of the magnetometers is easily calculated using the average values of the measurements on the axes:

$$B_{Hiron} = \frac{1}{2}\left[B_{sx}^{max,+} + B_{sx}^{min,-} \quad B_{sy}^{max,+} + B_{xy}^{min,-} \quad B_{sz}^{max,+} + B_{sz}^{min,-}\right]^T \tag{3.3.8}$$

$$B_{Hiron} = [37.9665 \quad -4.0040 \quad -6.2920]^T \tag{3.3.9}$$

nT (nano Tesla) is used as the unit for Equation 3.3.8 and Equation 3.3.9. For the soft iron matrix, the calibration procedure can be simplified by eliminating the non-diagonal components to minimize the model's complexity [Renaudin 2010]. The soft iron matrix equation

$$B_{SOiron} = \begin{bmatrix} B_{SOxx} & B_{SOxy} & B_{SOxz} \\ B_{SOyx} & B_{SOyy} & B_{SOyz} \\ B_{SOzx} & B_{SOzy} & B_{SOzz} \end{bmatrix} \tag{3.3.10}$$

is simplified to:

$$B_{SOiron} = diag(B_{SOxx} \quad B_{SOyy} \quad B_{SOzz}) \tag{3.3.11}$$

where,

$$B_{SOxx} = \frac{1}{3}\left(B_{avg,sx} + B_{avg,sy} + B_{avg,sz}\right)/B_{avg,sx} \tag{3.3.12}$$

$$B_{SOyy} = \frac{1}{3}\left(B_{avg,sx} + B_{avg,sy} + B_{avg,sz}\right)/B_{avg,sy} \tag{3.3.13}$$

$$B_{SOzz} = \frac{1}{3}\left(B_{avg,sx} + B_{avg,sy} + B_{avg,sz}\right)/B_{avg,sz} \tag{3.3.14}$$

and

$$B_{avg,sx} = \frac{1}{2}\left(B_{sx}^{max,+} - B_{sx}^{min,-}\right) \tag{3.3.15}$$

$$B_{avg,sy} = \frac{1}{2}\left(B_{sy}^{max,+} - B_{sy}^{min,-}\right) \tag{3.3.16}$$

$$B_{avg,sz} = \frac{1}{2}\left(B_{sz}^{max,+} - B_{sz}^{min,-}\right) \tag{3.3.17}$$

After calibration, B_{SOiron} is as follows:

$$B_{SOiron} = diag(1.0694 \quad 1.0766 \quad 1.0751) \tag{3.3.18}$$

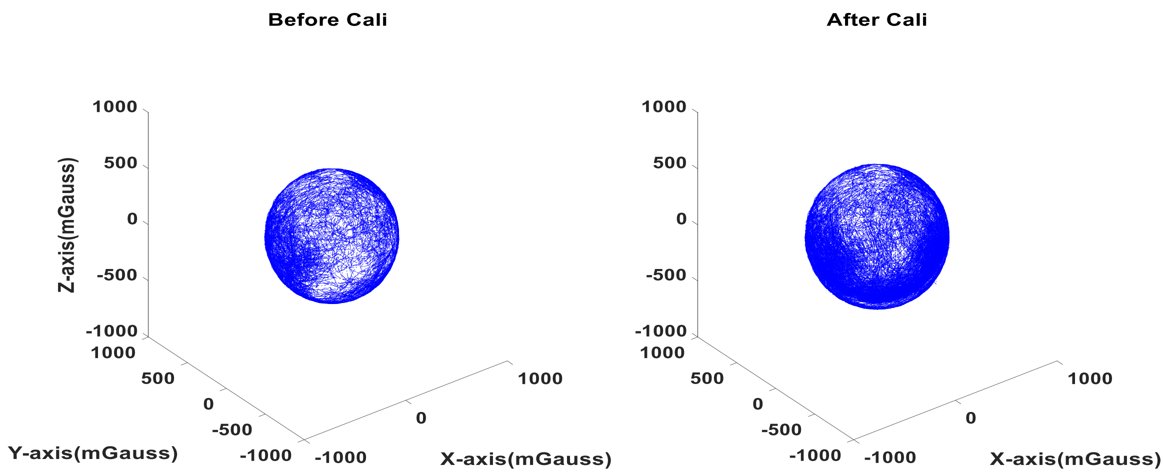

Figure 3.3.4 Calibration of magnetometer (3D)

Figure 3.3.4 shows the results of a 3D calibration for magnetometers. From the values of the magnetic field at the University of Calgary and the shape of the magnetic sphere, it can be determined that the magnetometers are well calibrated.

Accelerometer Correction Procedures

Dynamic accelerations can be used to obtain positions by calculating the double integral. However, movements are not fast in many applications of subsurface sensing and measurements of accelerations are difficult to obtain if movements are slow in real application environments. Therefore, accelerometers have difficultly measuring accurate dynamic accelerations because acceleration values are very small. For lab-scale tests in this research, the accelerometer measurements of dynamic acceleration correction are necessary even after gravity is removed from the calculation because the dual acceleration difference method only works well for certain rotations (>140 deg/s) [Kiosk 2008]. To address this problem, we propose an acceleration correction method using dual accelerometers and ANFIS to calculate accurate accelerations. As shown in Figure 3.3.5, two IMUs rotate around the azimuth and inclination directions on the same side of the rotation center; the difference between the centrifugal accelerations is calculated as follows:

$$|\ddot{x}_B - \ddot{x}_A| = (R_B - R_A)\left(\dot{\theta}_y^2 + \dot{\theta}_z^2\right) = D\left(\dot{\theta}_y^2 + \dot{\theta}_z^2\right) \tag{3.3.19}$$

Here, D is the distance between two IMUs. $\dot{\theta}_y$ and $\dot{\theta}_z$ are inclination and azimuth angular speeds, respectively, which are obtained from other sensors such as gyroscopes. However, when the rotation is slow, the accelerometers cannot accurately measure the dynamic accelerations, and therefore, an error, described below, occurs:

$$Err_{\ddot{x}1} = |\ddot{x}_{SB} - \ddot{x}_{SA}| - D\left(\dot{\theta}_{sy}^2 + \dot{\theta}_{sz}^2\right) \tag{3.3.20}$$

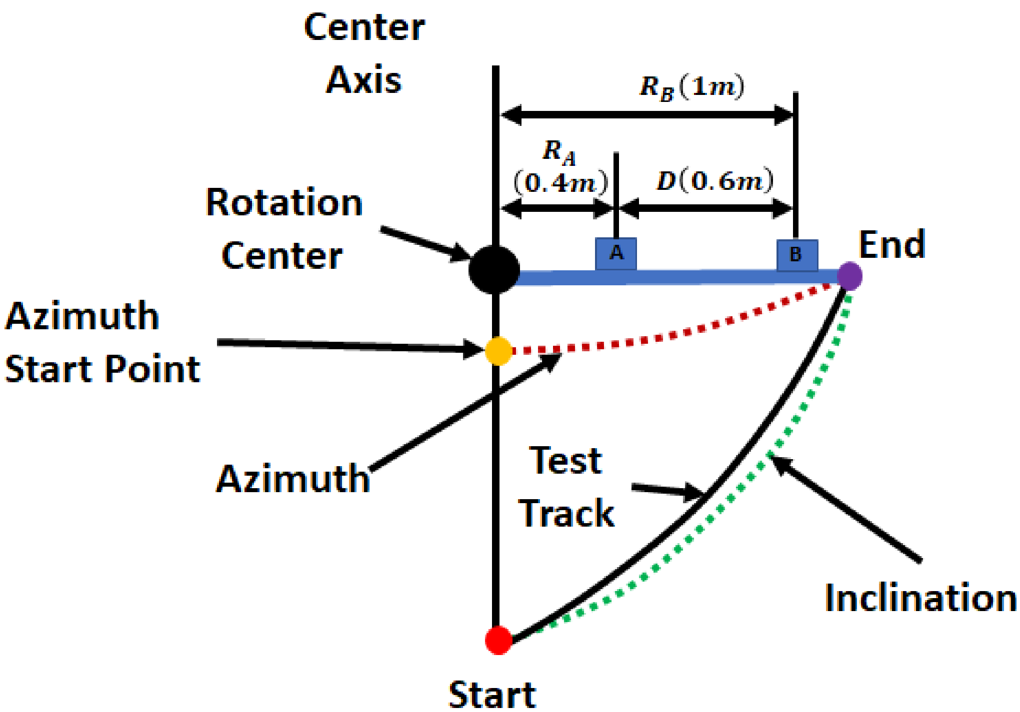

Figure 3.3.5 Moving displacement in polar coordinates

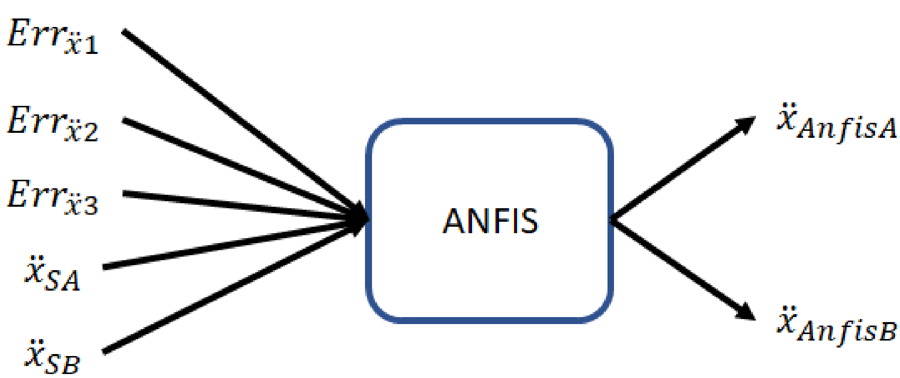

Figure 3.3.6 ANFIS design to obtain accelerations

where S denotes the value from an accelerometer sensor. Also, we know

$$|\ddot{x}_B + \ddot{x}_A| = (2R_A + D)\left(\dot{\theta}_y^2 + \dot{\theta}_z^2\right) = (2R_B - D)\left(\dot{\theta}_y^2 + \dot{\theta}_z^2\right) \tag{3.3.21}$$

Therefore,

$$Err_{\ddot{x}2} = |\ddot{x}_{SB} + \ddot{x}_{SA}| - (2R_A + D)\left(\dot{\theta}_{sy}^2 + \dot{\theta}_{sz}^2\right) \tag{3.3.22}$$

$$Err_{\ddot{x}3} = |\ddot{x}_{SB} + \ddot{x}_{SA}| - (2R_B - D)\left(\dot{\theta}_{sy}^2 + \dot{\theta}_{sz}^2\right) \tag{3.3.23}$$

Here, the radii R_A and R_B are calculated as follows:

$$R_A = \frac{\ddot{x}_{SA}}{(\dot{\theta}_{sy}^2 + \dot{\theta}_{sz}^2)}, \qquad R_B = \frac{\ddot{x}_{SB}}{(\dot{\theta}_{sy}^2 + \dot{\theta}_{sz}^2)} \tag{3.3.24}$$

Based on the above Equations 3.3.20-3.3.24, ANFIS can obtain accurate accelerations (an example is shown in Figure 3.3.6 with the correction case on the x_s axis). For the acceleration correction on the y_s and z_s axes, the following equations can be derived similar to the derivation of Equation 3.3.19:

$$(\ddot{y}_B - \ddot{y}_A) = D\ddot{\theta}_z \tag{3.3.25}$$

$$(\ddot{z}_B - \ddot{z}_A) = D\ddot{\theta}_y \tag{3.3.26}$$

Similar to the process for the x_s axis, the errors on the y_s and z_s axes are as follows:

$$Err_{\ddot{y}1} = (\ddot{y}_{SB} - \ddot{y}_{SA}) - D\ddot{\theta}_{sz} \tag{3.3.27}$$

$$Err_{\ddot{z}1} = (\ddot{z}_{SB} - \ddot{z}_{SA}) - D\ddot{\theta}_{sy} \tag{3.3.28}$$

$$Err_{\ddot{y}2} = |\ddot{y}_{SB} + \ddot{y}_{SA}| - (2R_A + D)\ddot{\theta}_{sz} \tag{3.3.29}$$

$$Err_{\ddot{z}2} = |\ddot{z}_{SB} + \ddot{z}_{SA}| - (2R_A + D)\ddot{\theta}_{sy} \tag{3.3.30}$$

$$Err_{\ddot{y}3} = |\ddot{y}_{SB} + \ddot{y}_{SA}| - (2R_B - D)\ddot{\theta}_{sz} \tag{3.3.31}$$

$$Err_{\ddot{z}3} = |\ddot{z}_{SB} + \ddot{z}_{SA}| - (2R_B - D)\ddot{\theta}_{sy} \tag{3.3.32}$$

The accelerations on the y_s and z_s axes are corrected using ANFIS, as shown in Figure 3.3.6. Figure 3.3.7 shows the raw dynamic accelerations from IMUs A and B, both of which are mounted on the rotation arm of the test rig; the configuration is shown in Figure 3.3.5. The original signals are not accurate because the rotational speed is low (<15deg/s). After the ANFIS compensation, the accelerations are corrected (Figure 3.3.8). Also, Figure 3.3.9 shows that the rotational radii can be calculated using the corrected accelerations (the rotational radii are shown in Figure 3.3.5).

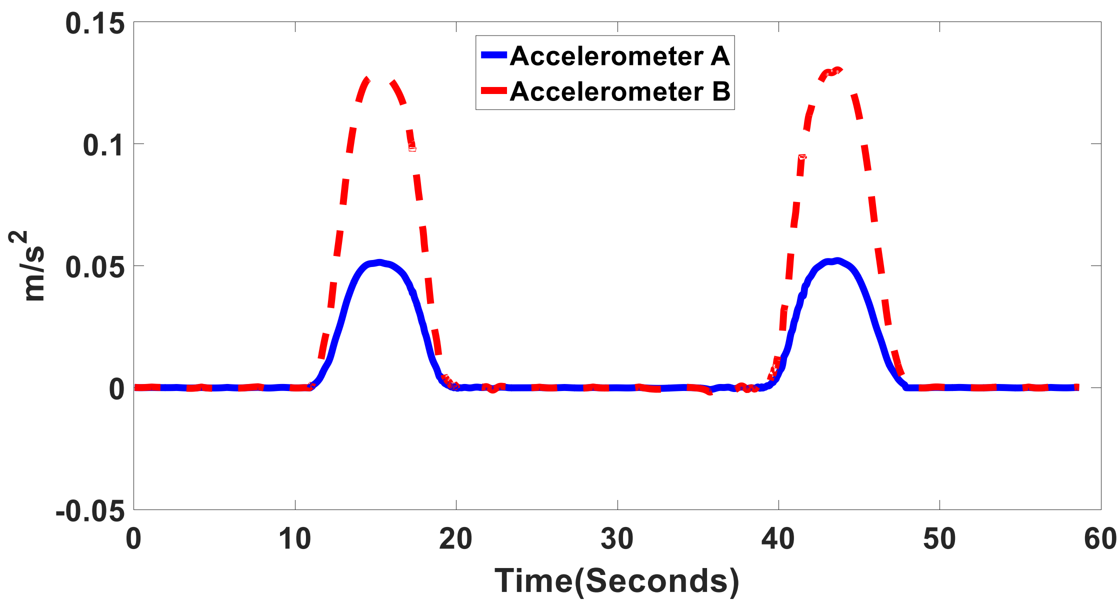

Figure 3.3.7 The dynamic accelerations after compensation

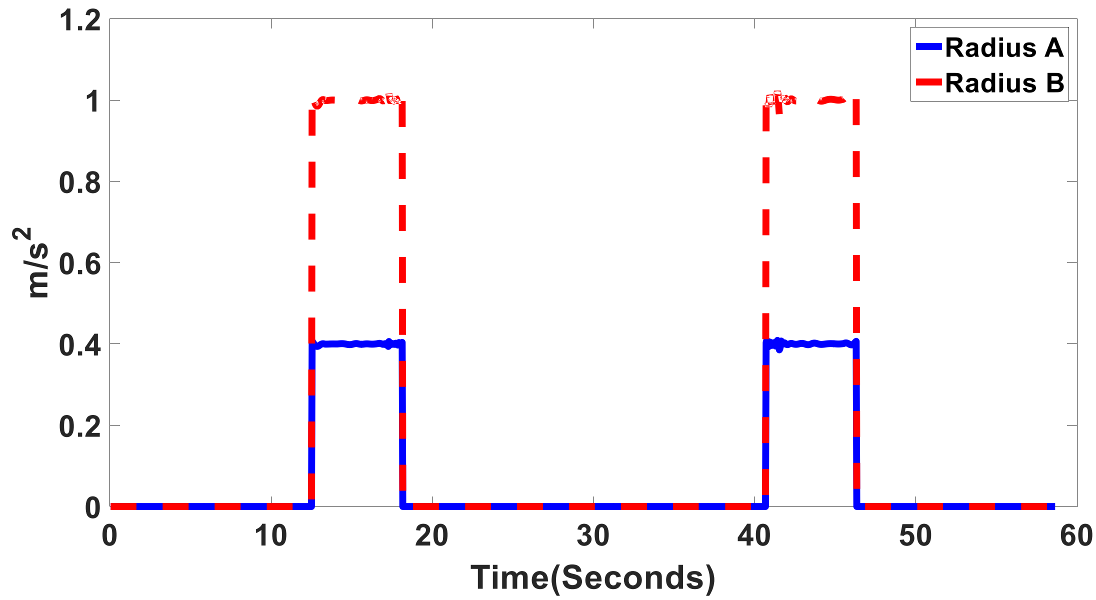

Figure 3.3.8 The radii calculated using the corrected accelerations

3.4 Summary

The sensor configuration is designed such that two IMUs are mounted on a rigid body that is separated by a known distance *D*. To test the sensor, we built a testing and calibration rig to simulate subsurface sensing movements including rotational (inclination, azimuth) and translational motion.

Different kinds of IMU errors are then described, including the 2D and 3D magnetic hard and soft iron calibration methods. The 2D calibration is designed for indoor tests and includes two steps: the 3D magnetic measurements (vertical and horizontal) are first converted into 2D measurements (horizontal) using a transfer matrix, and then the converted 2D measurements are calibrated. Tumble tests are used for 3D calibration for outdoor tests.

Finally, to extend the dual acceleration difference method to low speed rotation applications (<140 deg/s), we introduce an ANFIS design, which is used to correct the rotational dynamic accelerations.

CHAPTER 4. ANGLE FUSION METHODS

Subsurface sensing technologies are necessary to investigate the subsurface environment and evaluate industry subsurface activities. For subsurface activities, such as using an inclinometer to monitor reservoir status or MWD for directional drilling, the sensors applied in subsurface sensing must provide proper orientation angles to guarantee proper activity procedures. For example, it is necessary for the MWD sensors to measure proper well path orientations, which are then combined with the drill string length to obtain drilled borehole positions. Inclinometers are usually used to measure the inclinations of a well during subsurface activities.

Data from accelerometers and magnetometers are typically used to determine the orientation angles in commercial operations. In some tools, gyroscopes are employed to improve the low signal to noise ratios of accelerometers and magnetometers. A hybrid multi-sensor system that combines a magnetometer with a gyroscope can increase the accuracy of the azimuth since a gyroscope's signal is smooth and robust against magnetic disturbances. Combining these two sensors with a Kalman filter (KF) removes the noise inherent in magnetic signals and reduces drift in integral calculation caused by the DC component of gyroscope signals [Bergamini et al., 2014].

The current MWD systems are based on magnetic surveying technology [ElGizawy et al., 2010], where the magnetic surveying part of MWD systems is housed in a special non-magnetic drill collar and consists of three-axis accelerometers and three-axis magnetometers [Xue et al., 2014]. However, this method does not perform well because of magnetic disturbances, which are randomly located and hard to predict. Such magnetic disturbances can be caused by drill string components (such as polarized steel pipe or electrically powered equipment) that may affect the magnetic field, geomagnetic influences, downhole ore deposits, etc. [Noureldin 2002; EIGizawy 2009].

If there are magnetic disturbances, a gyroscope is employed to correct the heading errors since the headings can be updated by gyroscope data [Fan et al., 2017; Zhang et al., 2011]. However, there are several problems associated with gyroscope compensation. Unlike typical sensing activities at the earth's surface, such as outdoor vehicle movement detection, motion in the subsurface is much slower, which means magnetometers may be exposed to ferromagnetic objects for an extended period of time, and the drift caused in gyroscope data integral calculation may affect the heading performance [Lee et al., 2016]. Also, gyroscopes are susceptible to shock impacts, and the shocks could cause drift in gyroscope data integral calculation.

Liu et al. [2018] proposes a two-level structure fusion method to reduce the influnce of magnetic disturbances using QKF and ANFIS with geomagnetic referencing. QKF is affected by unknown, non-white magnetic disturbances when obtaining azimuth angles because a priori variance information is necessary to set up the matrices of Q and R. To reduce the effect of unknown magnetic disturbances of a QKF, we propose a global ANFIS filter. The filter consists of a two-level structure with two local level filters (QKF) and a global level filter (ANFIS). To remove the unknown magnetic disturbances, using the local geomagnetic field values as a reference, we compare the measurements of two magnetometers with the reference values. Then the deviation values (between the two sets of magnetometers and the geomagnetic reference) are used as input into the ANFIS filter. According to the deviation information, the ANFIS calculates the proper weights for the two magnetometers. In this situation, however, shock is not considered.

In this chapter, we discuss our design that uses two redundant sets of IMUs with a known distance *D* to increase the accuracy of orientation angle estimations in the presence of magnetic and shock disturbances.

Section 4.1 outlines a supervised learning filter (SLF) designed to reduce the effect of shock and magnetic disturbances. Supervised machine learning methods have a feature that allow it to map inputs to outputs based on teaching signal training [Roth 2016; Wang 2011]. The teaching signal can also be used as data labelling [Arachie et al., 2019]. Our design labels the errors (big or small) of different kinds of sensors when the sensors perform poorly due to disturbances. Each sensor is used to compare with other sensors to obtain the error groups of the sensor (we name this sensor as center sensor). Then, the error groups are fed into ANFIS to label the center sensor as belonging to small or big error groups. After identifying the center sensor's accuracy, a proper weight is calculated and added to the center sensor. The proposed idea is evaluated using lab-scale evaluation results based on a lab test rig. The results yield accurate angle estimations based on an error RMS value evaluation and under the condition that at least one sensor is accurate.

Section 4.2 introduces a KF optimized by the supervised learning method introduced in section 4.1. This supervised learning (SL)-KF is designed to further increase accuracy when all sensors are affected by the disturbances. The rotational angles and angular speeds are first computed by an SLF (local filter) and then fed into a KF, which uses as a global filter. This method is evaluated using the same test conditions described in section 4.1 and then compared with the proposed SLF.

4.1 Shock and Magnetic Robustness of SLF (Fusion Method 1)

According to Liu et al. [2018], data from accelerometers and magnetometers are typically used to determine orientation angles. The gravity elements on the x_s, y_s, and z_s axes, which are measured using accelerometers, can be used to compute inclination angles; the magnetometers measure magnetic field strength, and these measurements can be used to compute azimuth angles. However, the high signal to noise ratio of magnetometers needs to be improved. Gyroscopes are good candidates to reduce noise due to their smooth signals. A drawback of gyroscopes is drift during long-term integral calculations caused by the DC components embedded in gyroscopes [Bergamini et al., 2014].

Earth surface sensing activities employ gyroscopes to correct heading errors because the heading angles can also be obtained through integral calculations of gyroscopes data [Fan et al., 2017; Zhang et al., 2011]. When a magnetometer is exposed to ferromagnetic objects, the data from a gyroscope is used to correct the error caused by magnetic disturbances. However, when movements are too slow, gyroscopes may not be used to correct long duration magnetic disturbances because the drift caused by the integral calculation may difficult to be corrected [Lee et al., 2016]. Shocks also cause drift because gyroscopes are affected by shock impacts.

In addition to drift in the integral calculation, measuring rapidly rotating objects with large accelerations is challenging [Larin et al., 2012] since each gyroscope is designed for a particular maximum angular velocity, especially for MEMS gyroscopes [Tsai et al., 2010]. MEMS gyroscopes included in the IMUs used in this study are strongly affected by the large rotational accelerations during drilling processes since for a typical MEMS gyroscope the measurement range is only a few hundreds of degree/s [Iozan et al., 2016; Cao et al., 2017]. Also, the performance of MEMS gyroscopes can be affected by various shock impacts [Li et al., 2014].

Typical MWD tools currently used in industry favor accelerometers [Shor et al., 2015], but gyroscopes are often found in tools used for continuous drilling survey applications [ElGizawy et al., 2010]. Non-strapdown based gyroscopes are available (for example, fiber-optic coil), which may be more robust to the subsurface environment; however, current technologies are not economically viable [Gebre-Egziabher 2004].

Using redundant accelerometers to obtain rotation information is becoming popular as a means to address the issues of gyroscopes [Wang et al., 2014; Bhuiyan et al., 2013]. Without the assistance of a gyroscope, the minimum number of accelerometers needed to extract 3D rotational information is six [Nilsson et al., 2016]. Therefore, using two IMUs, each with three accelerometers, one each on the x_s, y_s, and z_s axes, allows for rotational information to be obtained using only accelerometers.

The objective of this section is to enhance the accuracy of subsurface orientation using two redundant sets of IMUs to reduce the effect of magnetic and shock disturbances on orientation angle estimations. Magnetometers and gyroscopes are used to obtain orientation angles, and instead of gyroscopes, redundant accelerometers are used to obtain redundant rotational information. By separating the IMUs by a constant distance, the difference between the two centripetal acceleration elements may be used to provide redundant rotational information. The newly proposed sensor configuration and fusion method improve sensor robustness to magnetic and shock disturbances. Using two magnetometers with a constant distance can reduce the negative effect of magnetic disturbances. For the fusion method, an SLF that uses ANFIS is designed. The ANFIS builds the error models of different orientation angles obtained from the accelerometers, gyroscopes, and magnetometers, which means using the ANFIS to label the errors (small or big) of each sensor. Based on the outputs from these error models, weights are calculated for each sensor and these weights show the accuracy of each sensor in an applied environment.

4.1.1 Rotation Angles from Dual Tri-axis Accelerometers

Gyroscopes are good at obtaining angular velocities under dynamic movements. However, the maximum angular speed measurement limitation, which is caused by the internal structure of a gyroscope, reduces potential applications in the industry [Iozan et al., 2016; Cao et al., 2017]; in addition, shocks negatively impact the performance of gyroscopes [Li et al., 2014]. Using dual tri-axis accelerometer sets separated by a known distance to find angular velocity estimations, orientation estimations can be improved [Kionix, 2008]. The acceleration magnitude (a_p) of a moving point, as shown in Figure 4.1.1, is calculated as follows:

$$a_p = \sqrt{a_x^2 + a_y^2 + a_z^2} = \sqrt{a_N^2 + a_T^2} \tag{4.1.1}$$

where a_x, a_y, a_z are the particle accelerations on *x*, *y*, and *z* axes, respectively, a_N is centripetal acceleration, and a_T is tangential acceleration. The following equation is used to find the difference between the two measurements of the accelerometers:

$$a_{NB} - a_{NA} = (\rho_B - \rho_A)\left(\dot{\theta}_z^2 + \dot{\theta}_y^2\right) = D\left(\dot{\theta}_z^2 + \dot{\theta}_y^2\right) \tag{4.1.2}$$

The x_s axis of the IMU is oriented along the rotation radius (centripetal direction, as shown in x_s of the IMU in Figure 4.1.1), the y_s and z_s axes of the IMU are tangential to the rotation(y_s,z_s

axes of the IMU in Figure 4.1.1), and the rotation center of the IMU is set as (0,0,0); however, the rotation arm does not rotate around the IMU x_s axis in our test rig design.

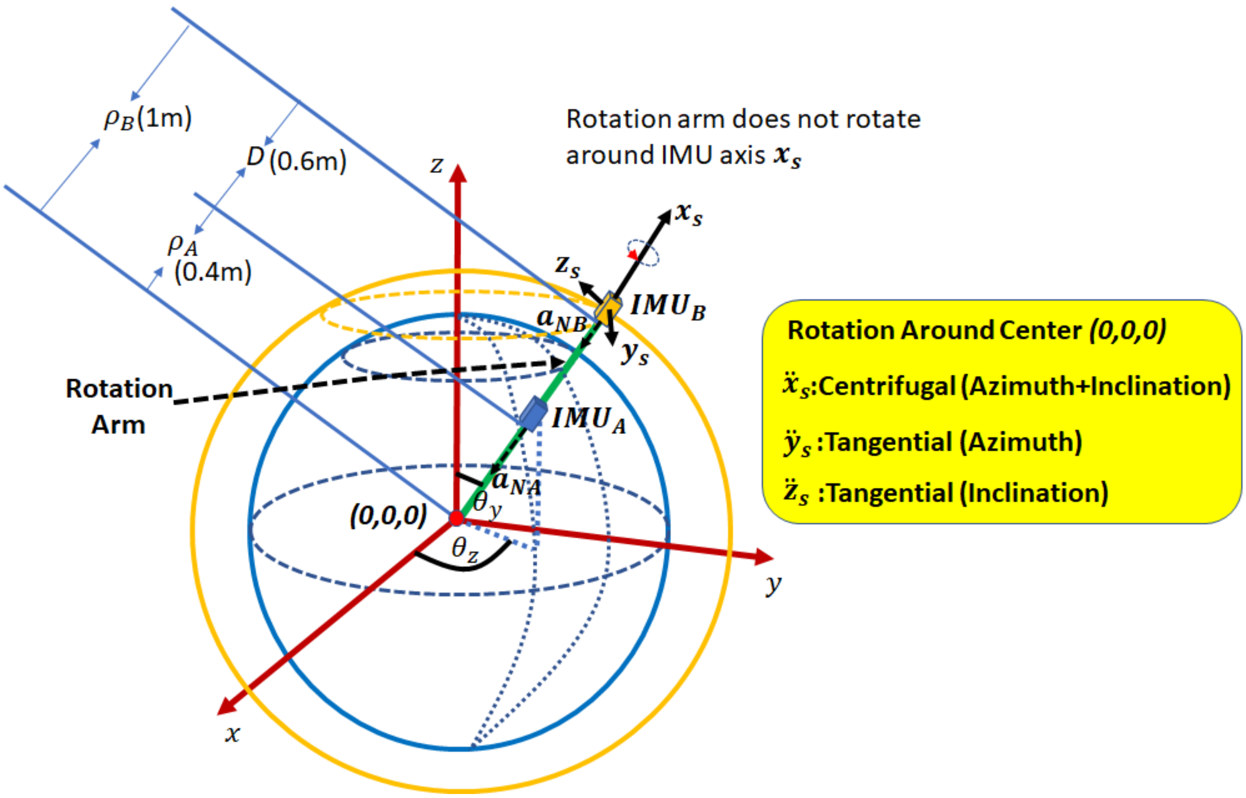

Figure 4.1.1 Spherical coordinates for two redundant accelerometers

Based on the configuration of the pair of IMUs, the centripetal components of the accelerations in Equation 4.1.2 are measured using the x_s axes of the IMUs. Therefore, the centripetal acceleration a_{NA} & a_{NB} obtained by IMU$_A$ and IMU$_B$ are denoted as $\ddot{x}_{sA}$ & $\ddot{x}_{sB}$, respectively. The difference between these two centripetal elements of the acceleration is used to calculate the square root sum of the roation speeds of the inclination and azimuth (Equation 4.1.3) [Kionix, 2008].

$$\dot{\theta}_{centripetal} = \sqrt{\dot{\theta}_z^2 + \dot{\theta}_y^2} = \sqrt{|\ddot{x}_{sB} - \ddot{x}_{sA}|/D} \quad (4.1.3)$$

Here, the s denotes the values obtained from an IMU.

$$\dot{\theta}_{zcentripetal} = \vartheta_{Azi} * \dot{\theta}_{centripetal} \quad (4.1.4)$$

$$\dot{\theta}_{ycentripetal} = \vartheta_{Incli} * \dot{\theta}_{centripetal} \quad (4.1.5)$$

$$\gamma_{Azi} = \frac{\dot{\theta}_{zinteg}}{\sqrt{\dot{\theta}_{zinteg}^2 + \dot{\theta}_{yinteg}^2}} \quad (4.1.6)$$

$$\gamma_{Incli} = \frac{\dot{\theta}_{yinteg}}{\sqrt{\dot{\theta}_{zinteg}^2 + \dot{\theta}_{yinteg}^2}} \quad (4.1.7)$$

Because $\dot{\theta}_{centripetal}$ in Equation 4.1.3 includes the components of inclination, azimuth, and angular velocities, and the term is always positive, it cannot be used directly. As shown in Equations 4.1.6 and 4.1.7, the ratio factors ($\gamma_{Azi}, \gamma_{Incli}$), which identify the proper percentages of inclination and azimuth, are necessary; also, the factors provide correct rotational directions (positive and negative signs of the calculated rotational angular speeds). These ratio factors can be obtained from the integral calculation of the tangential accelerations or derived from azimuth (magnetometer) and inclination (gravity) angular values.

4.1.2 SLF Design (Magnetic and Shock Disturbance Robustness)

Identifying when measurements have low accuracy, as during a shock event or while passing a magnetic disturbance, is paramount to effective sensor fusion. For example, as one of the redundant IMUs passes a magnetic disturbance, the magnetometer is adversely affected, but the gyroscope remains unaffected.

The azimuth angle is estimated using the weighted information obtained from different sensors and methods; the weighted average of different azimuth angles provides an appropriate estimation despite magnetic disturbances. To determine the proper weights of each azimuth angle, we employ a fuzzy inference system (FIS). In this paper, a special process of the SLF using ANFIS is proposed to tune membership functions and design the precise fuzzy rules to improve performance and to build the error model of each sensor. Sensor values are used as the inputs of the ANFIS error models to output the error of each sensor. Based on the magnitudes of these errors, the weight of each sensor is computed.

Adaptive Neural Fuzzy Inference System (ANFIS)

ANFIS is an algorithm that combines neural network and fuzzy logic to obtain more accurate results. By using a back propagation neural network learning algorithm, the parameters of the Takagi-Sugeno (TS) fuzzy model continue updating until they reach an optimal solution [Arsava 2013].

ANFIS is a combination of a Takagi-Sugeno type fuzzy inference system (FIS) and a neural network (NN). The core of ANFIS is FIS, and combined with the NN, the 'IF-THEN' rules are updated automatically to predict the behavior of many uncertain systems [Lei 2012].

Compared to FIS, NN is employed to adapt the environments in ANFIS. With the input-output data, a back propagation algorithm is applied to ANFIS to minimize the error [Ayaz 2014;

Nilashi 2011]. Lei [2012] used two fuzzy if-then rules based on a first order Sugeno model to explain the ANFIS architecture (Figure 4.1.2).

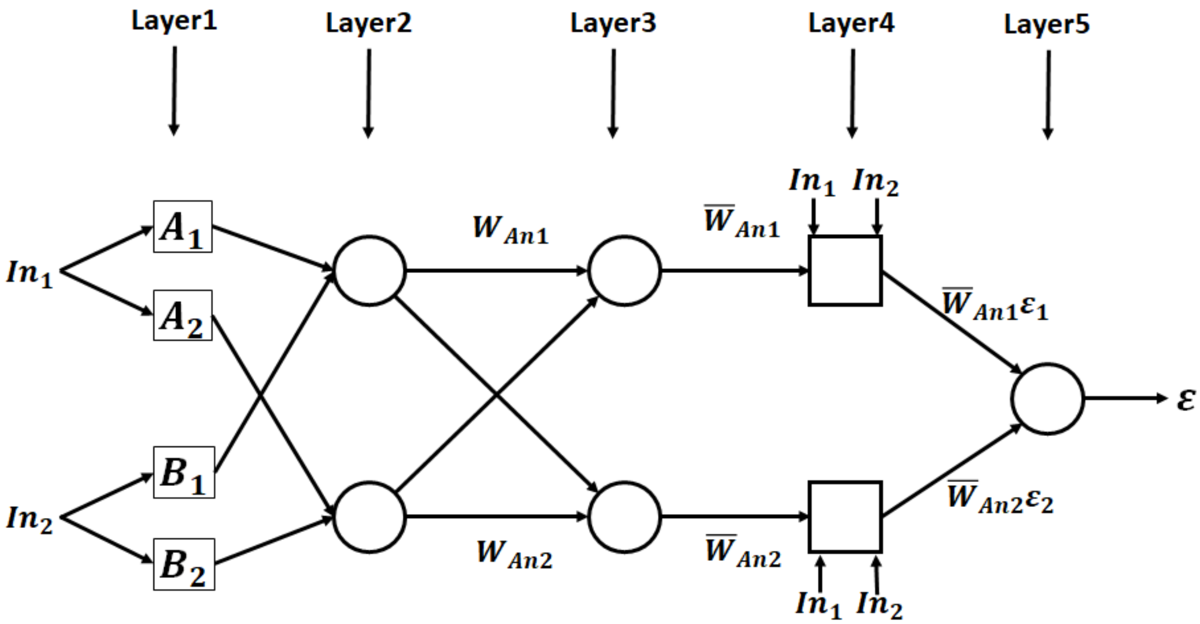

Figure 4.1.2 ANFIS structure

$$Rule\ 1: If\ (In_1\ is\ A_1)\ and\ (In_2\ is\ B_1)\ then\ (\varepsilon_1 = p_1 In_1 + q_1 In_2 + r_1) \tag{4.1.8}$$

$$Rule\ 2: If\ (In_1\ is\ A_2)\ and\ (In_2\ is\ B_2)\ then\ (\varepsilon_2 = p_2 In_1 + q_2 In_2 + r_2) \tag{4.1.9}$$

The structure has five layers:

Layer_1: The first layer consists of input variables, also known as membership functions (MFs). Usually, the bell-shaped membership function is employed.

Layer_2: The second layer is called the MF checking layer. The incoming signals from the first layer are multiplied in this layer. This layer functions as MFs to fuzzify the inputs.

Layer_3: This layer is the layer of rules. Here, the activation level of each rule is computed, and the number of nodes in this layer is equal to the number of fuzzy rules. Each node calculates weights as follows:

$$\overline{W_i} = \frac{W_i}{W_1 + W_2}, i = 1,2 \tag{4.1.10}$$

Layer_4: The fourth layer provides the output values resulting from the inference of rules. Every node in the fourth layer is an adaptive node with a node function:

$$\overline{W_i}\varepsilon_i = \overline{W_i}(p_i In_1 + q_i In_2 + r_i), i = 1,2 \tag{4.1.11}$$

Layer_5: The fifth layer sums all inputs coming from the fourth layer. A single node in this layer is not adaptive. It computes the overall output as the summation of all incoming signals.

In this study, there are five clusters of data that serve as inputs of each ANFIS error model. Bell-shaped membership functions are chosen with a maximum value (one) and a minimum value (zero). The fuzzy logic toolbox in MATLAB was used for the entire process of training and evaluating the fuzzy inference system.

Error Teaching Signal

To obtain the error teaching signal, we compute various azimuth angles from magnetometers directly using gyroscope data integral calculation and information from two tri-axes accelerometers. These computed azimuth angles are compared with a reference azimuth angle to calculate the errors. For the lab-scale evaluation, the reference signal was from the encoder of the rotation motor. For a drilling industry application, the reference signal may be obtained from wellbore survey data [Liu et al., 2019].

SLF Logic

The first function of this design is to estimate the magnetometer errors caused by interferences to increase magnetic disturbance robustness. We have two azimuth angles from magnetometers (Azi_{mag1}, Azi_{mag2}, the errors of these two magnetometers are Err_{mag1}, Err_{mag2}), two azimuth angles from gyroscope signal integral calculations ($Azi_{gyro1},\ Azi_{gyro2}$, the errors of these two gyroscopes are Err_{gyro1}, Err_{gyro2}), and three azimuth angles from accelerometers ($Azi_{tangen}, Azi_{centri1}, Azi_{centri2}$, the errors are $Err_{acc1}, Err_{acc2}, Err_{acc3}$). There are three clusters of inputs identified with different blocks (a, black; b, red; and c, grass). For each cluster, one kind of sensor is used as the center value to compare with the other sensors; then, the obtained errors are used as inputs for ANFIS to build the error models (block a center: magnetometers; block b center: gyroscopes; block c center: dual accelerometers). For example, as shown in the black block (block a) of Figure 4.1.3, each azimuth angle from a magnetometer is compared with other azimuth angles from the other magnetometer, gyroscopes and accelerometers. The relationship between these relative differences and the sensor error is built with ANFIS as shown in Figure 4.1.3, which means the error model of each sensor is estimated using the relative differences between the sensors. After comparing the errors of all sensors, the weights of these sensors are obtained.

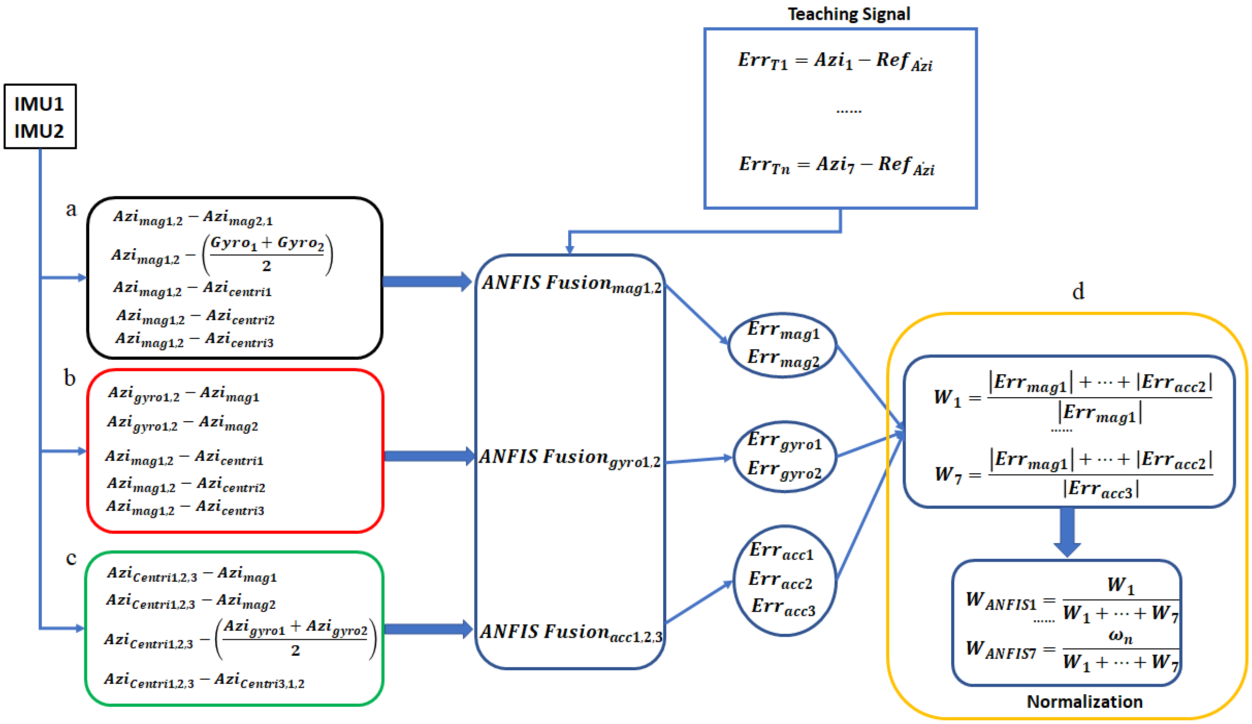

Figure 4.1.3 The structure of the SLF

For example, if IMU_A is affected by a magnetic disturbance but IMU_B is not, the magnetometer in IMU_A will not agree with the remaining measurements in IMU_A, while all measurements in IMU_B will be in agreement. In the event of a shock, the gyrosocpes in both IMU_A and IMU_B will be affected, but the disagreement between sensor measurements may still be used to compute the errors in the signals because the magnetometer is less affected by shocks compared with accelerometers and gyroscopes [Gooneratne 2017]. Calculating the weights of $W_{ANFIS1} \ldots W_{ANFIS7}$ based on the different azimuth error values is shown in Figure 4.1.3 (the orange block, block d); the ratio between one error and the sum total of the errors indicates how accurate the sensor is. After normalizing, the weights are used for final azimuth output.

4.1.3 Discussion of Lab-scale Evaluation and Results

As shown in Figure 4.1.4, the sensor setup contains dual IMUs, each of which has triaxial gyroscopes (× 3), accelerometers (× 3), and magnetometers (× 3) located on the x_s, y_s, and z_s axes, and data is sampled at 205 Hz. The IMUs are separated by 0.6 meters, with IMU_A located 0.4 meters and IMU_B located at 1.0 meter from the center of rotation, and they are mounted on a rigid body. The reference azimuth is obtained from the encoders on the motors. Sensor noise is classified as constant bias, calibraiton errors (scale factors, alignments, and linearities), and white or pink noise ($1/f$) [Woodman 2007; Patonis et al., 2018]. Constant bias and calibration errors are removed using calibration methods [Pasquale 2010; Hemanth et al., 2012; Yang et al., 2017; Ladetto et al., 2002].

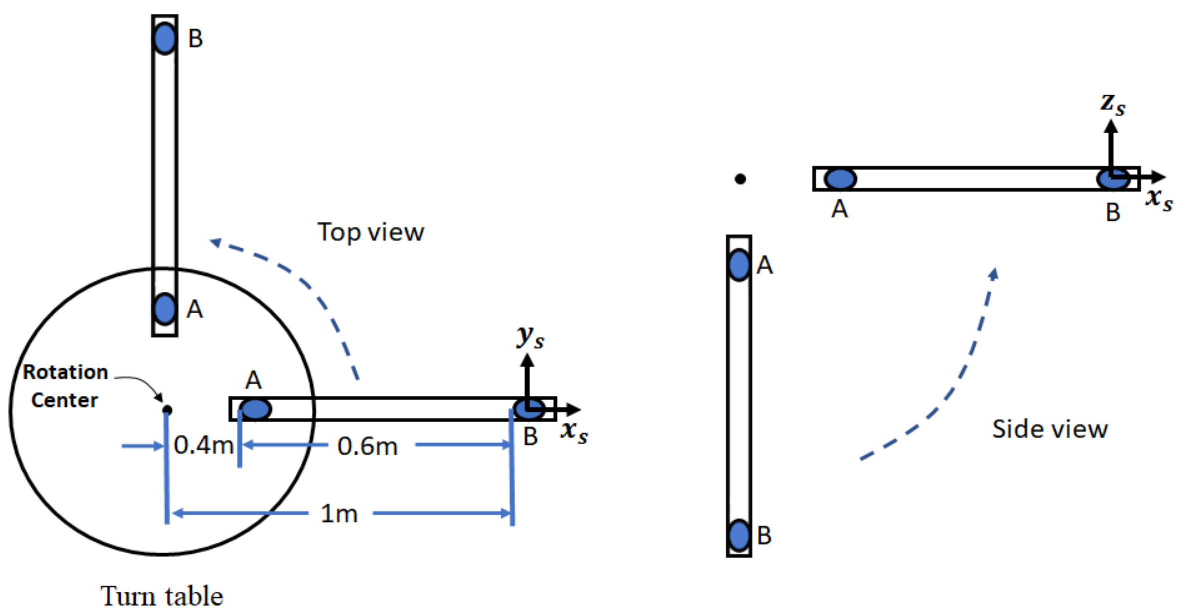

Figure 4.1.4 Trajectories implemented in the test rig

Table 4.1.1 provides the experimental events time-line. From 0 to 11 seconds is Rest1; from 11 to 19 seconds is the first rotation (Rotation1); from 13 to 16 seconds is the first magnetic disturbance in the first rotation; from 13.6 to 15 seconds is the shock disturbance; from 19 to 40 seconds is the second rest (Rest2); from 40 to 48 seconds is the second rotation (Rotation2) and the second magnetic disturbance happens during this time interval (43 to 46 seconds); from 48 to 59 seconds is Rest3.

Table 4.1.1 Experimental events time-line

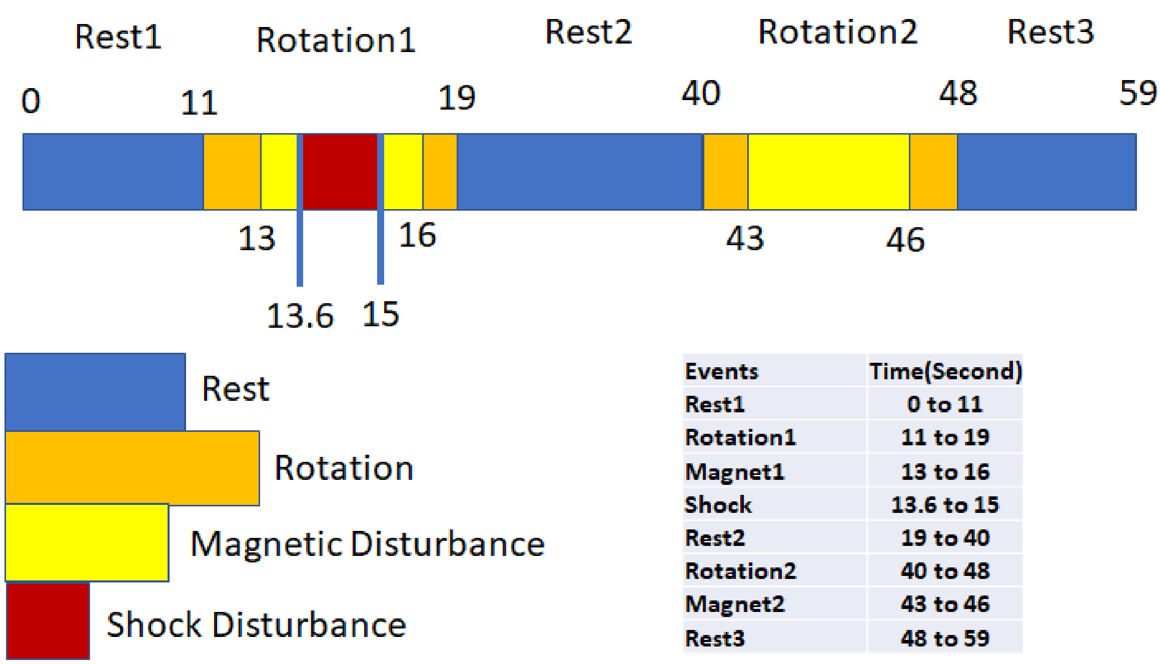

Events	Time(Second)
Rest1	0 to 11
Rotation1	11 to 19
Magnet1	13 to 16
Shock	13.6 to 15
Rest2	19 to 40
Rotation2	40 to 48
Magnet2	43 to 46
Rest3	48 to 59

Three continuous impacts were made with a shock hammer to simulate shocks with a 0.4 second time interval in the test rig setup. Magnetic disturbances were simulated using a permanent magnet (4.16×10^5 nT with a 50 mm distance) temporarily placed near one of the IMUs. Planned trajectories were implemented using the test rig. The coordinate frame was anchored at the IMUs as shown in Figure 4.1.5.

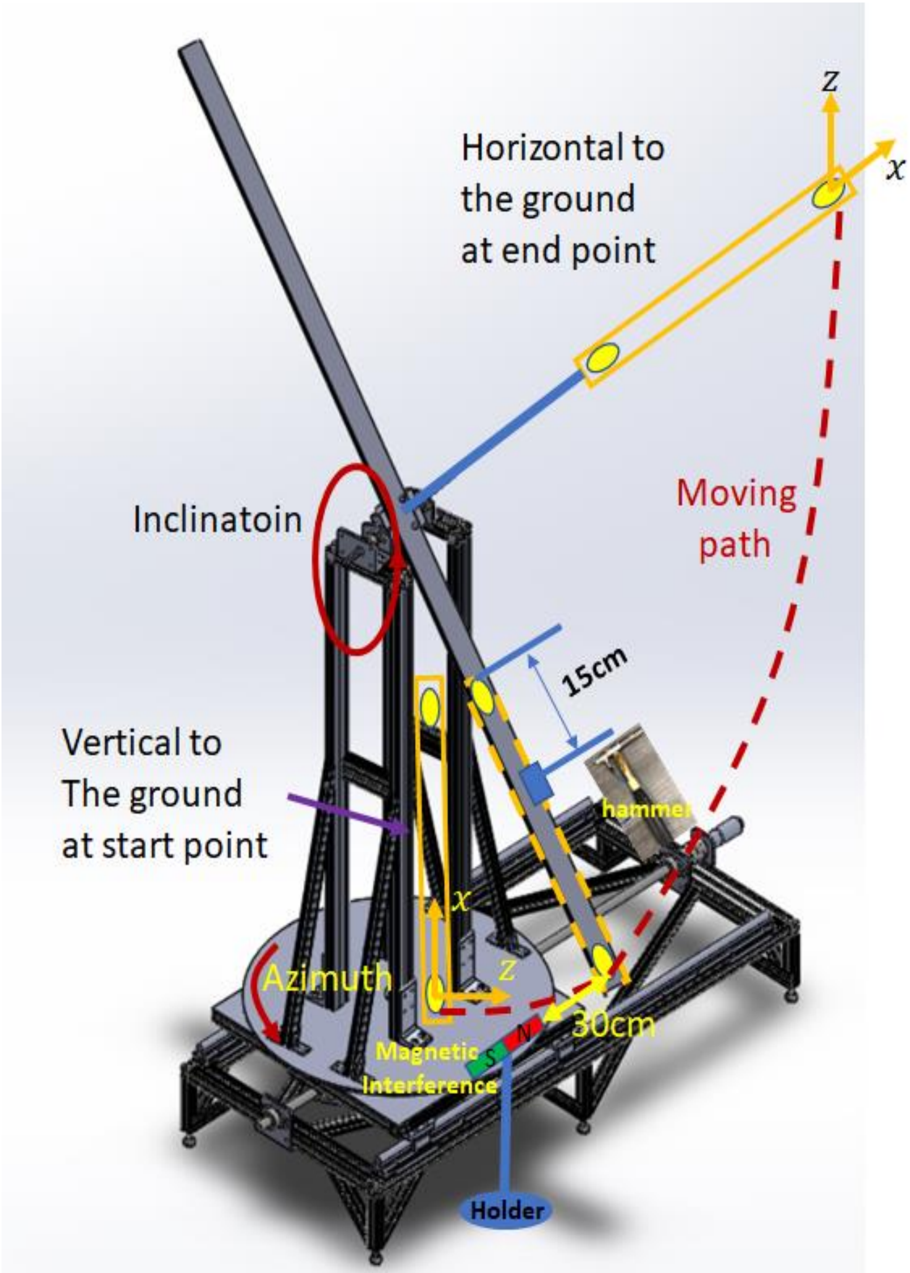

Figure 4.1.5 Image picture of shock and magnetic disturbance test.

Two case studies were used to evaluate the performance of the proposed sensor structure and the SLF method. For the first case study, a magnetic disturbance was applied to one magnetometer. The other magnetometer was unaffected since the separated distance *D* reduced the influence of the interference as a function of inverse 1st , 2nd, or 3rd power of *D* [Wu et al., 2017; EMFSinfo 2019]. Additionally, the sensors were subjected to shock impacts. Since both IMUs were mounted on a single rigid body, both gyroscopes were affected. For the second case study, both magnetometers were influenced by the same magnetic disturbance at the same time. Further, all sensors were affected by shock impacts.

Magnetic Interference and Shock Impact - First Case Study

Figure 4.1.6 shows the shock forces measured by an impact hammer sensor (PCB 208.A03) during a shock test (3 direct impacts on the rotation arm 15 cm away from IMU_A and 45 cm from IMU_B). Figure 4.1.7 shows the data of two magnetometers: the azimuth angle from $magnetometer_A$ is blue, and the azimuth angle from $magnetometer_B$ is black. $Magnetometer_B$ was affected twice by simulated magnetic interferences, while $magnetometer_A$ remained unaffected. The lower subplot of Figure 4.1.7 shows that the magnetometers were slightly affected by the shocks (the shock data were measured from the shock experiment, Figure 4.1.5).

Figure 4.1.8 shows the output results of the shocks on the gyroscopes. The disturbance data were obtained from the same shock test. The bottom plot of Figure 4.1.8 is the integral calculation of the gyroscope signal (angular velocity). The shocks caused an angle drift (around 10 degrees) during the integral calculation process.

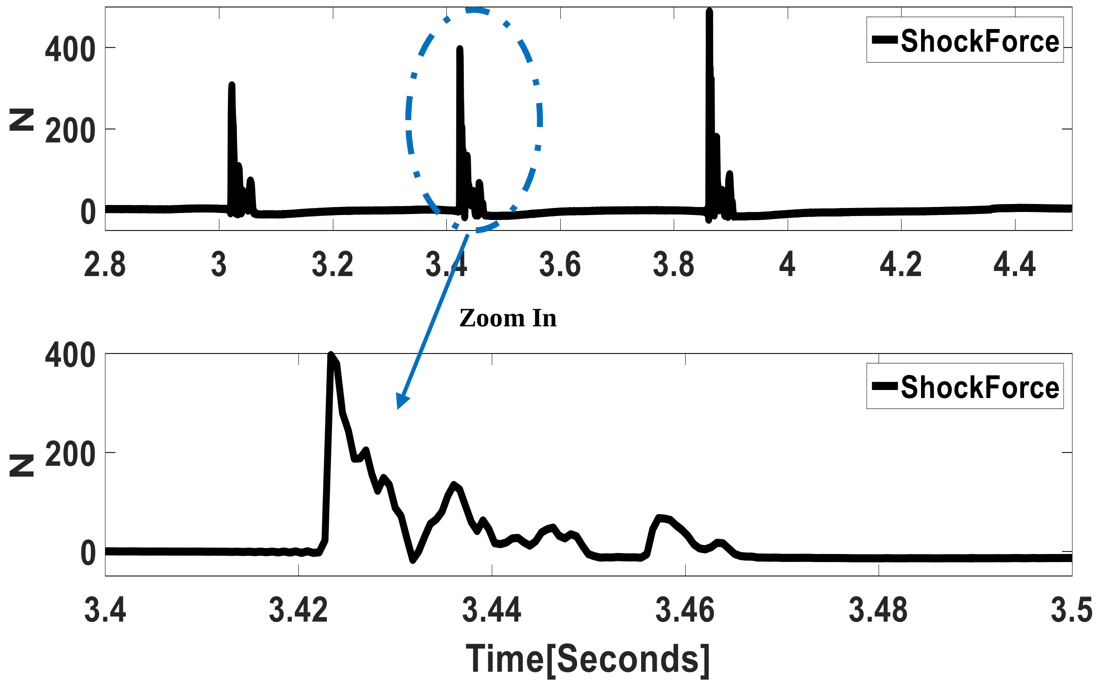

Figure 4.1.6 Shock forces measured from the shock test, 3 continuous hits with a time interval of 0.4 seconds. The force peak values of these 3 hits are approximately 300N, 400N, and 500N. The bottom subplot is the view (zoomed in) of the second hit.

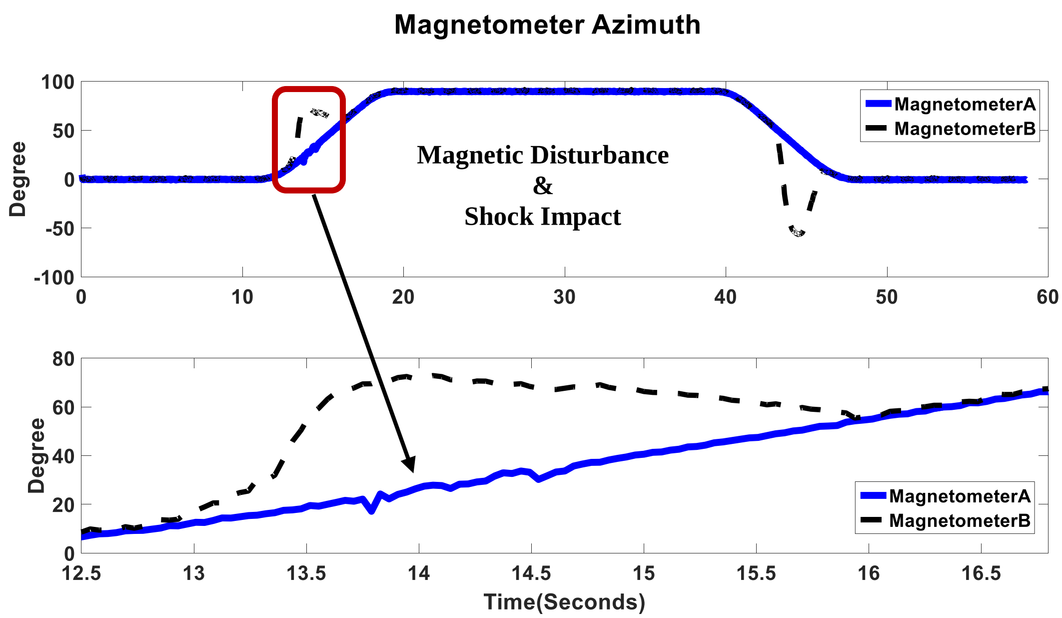

Figure 4.1.7 Data from two magnetometers from lab-scale tests.

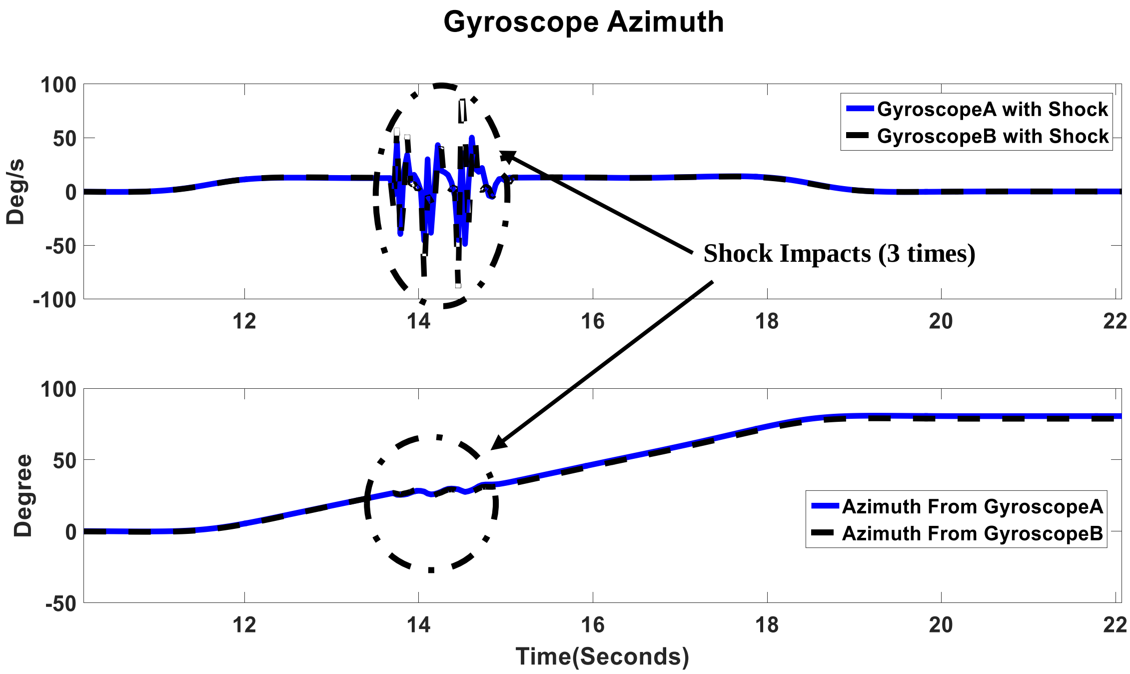

Figure 4.1.8 Gyroscope data from a shock test.

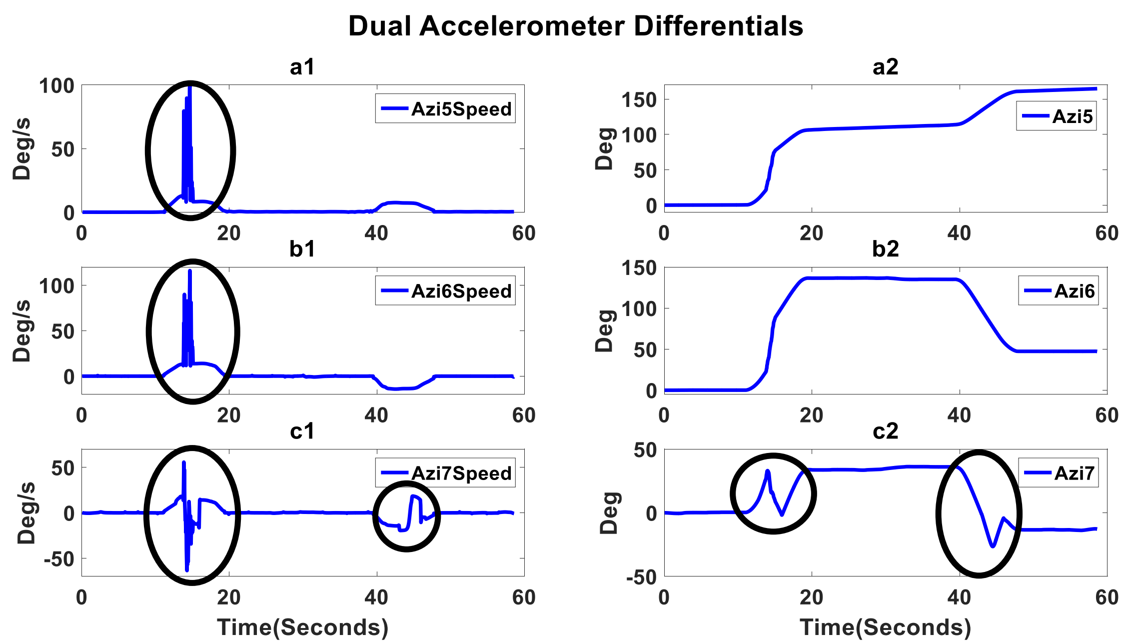

Figure 4.1.9 Data from dual accelerometer difference methods under a shock impact

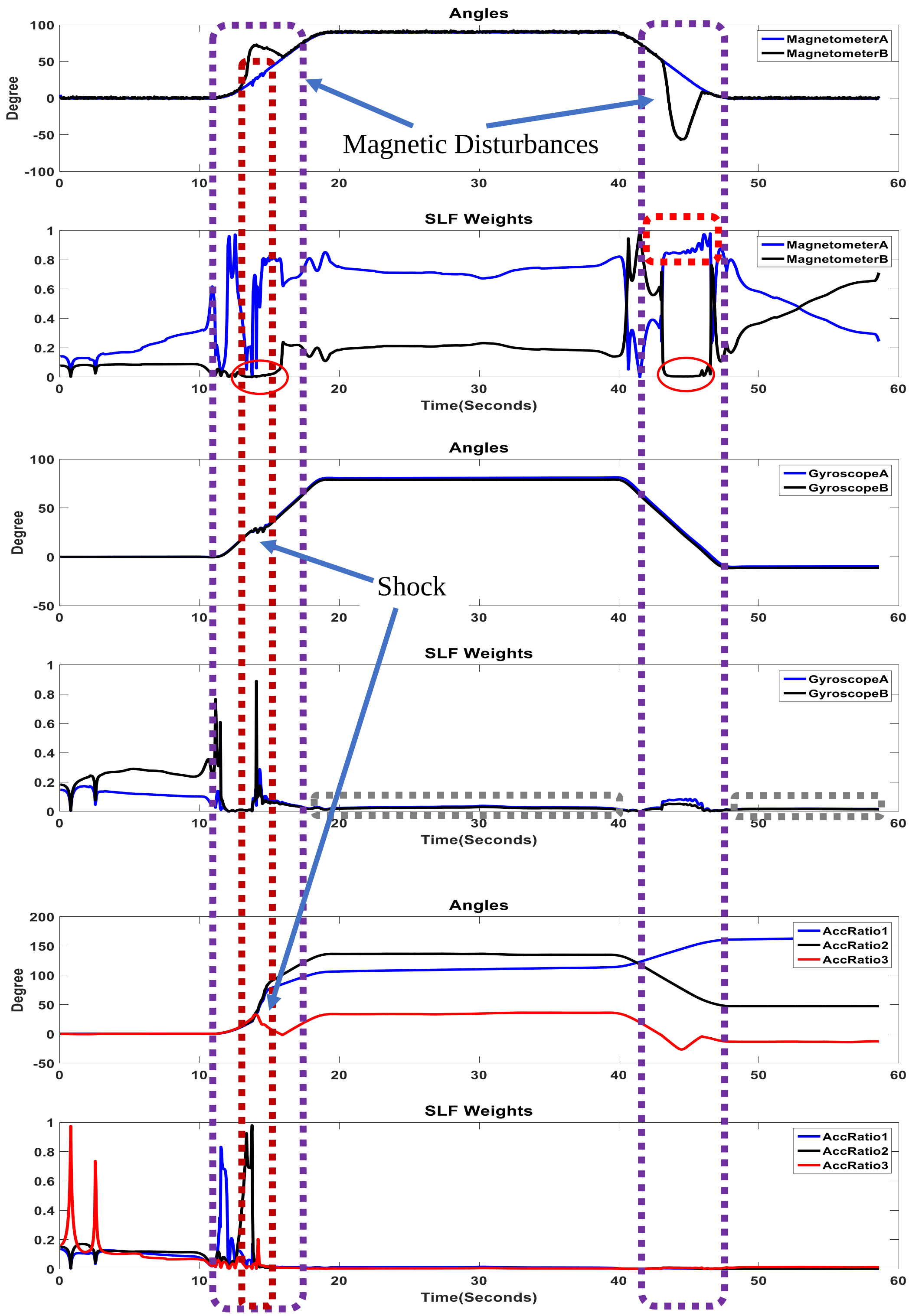

Figure 4.1.10 Sensor weights calculated by SLF

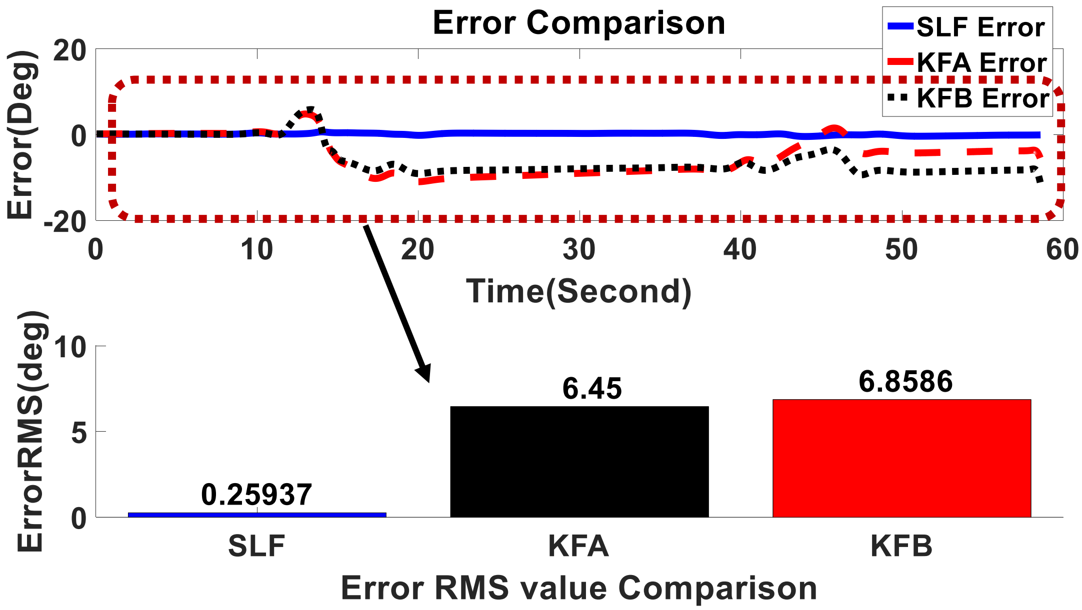

Figure 4.1.11 SLF compared with a KF (shock and magnetic disturbances)

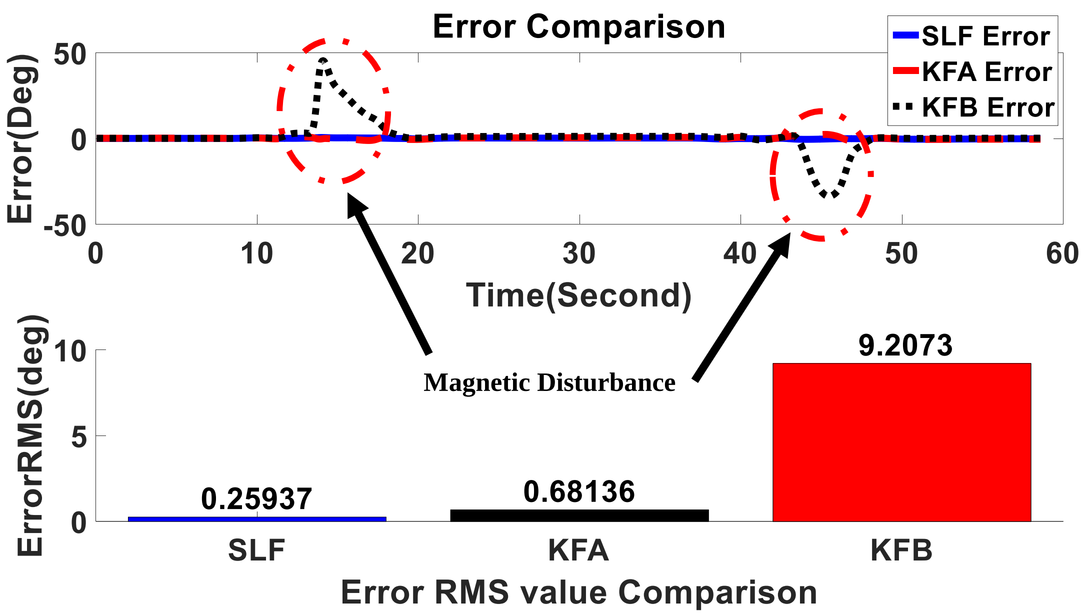

Figure 4.1.12 SLF compared with a KF (magnetic disturbances)

Figure 4.1.9 shows the angular speed from two accelerometers (disturbances were obtained from the same experiment) and their integral computation values (rotation angles). These results were calculated from Equation 4.1.4 with different ratio factors: a1&a2 shows the ratio factor obtained from tangential accelerations; b1&b2 shows the factor is from IMU_A, which is not affected by magnetic interferences; and c1&c2 shows the ratio factor calculated from the magnetometer azimuth and gravity inclination of IMU_B, which is affected by magnetic interferences. Dual accelerometers provided rotational information, but as shown from the final integrated results (second column of Figure 4.1.9), the angles drifted and jerked due to the shocks.

Figure 4.1.10 shows the values of the weights calculated by SLF as shown in Figure 4.1.3, which gives seven weights for the seven azimuth angles. The angles and weights were classified by sensor types of the same time-line. The SLF weights shown in the second subplot were the weights of the magnetometers when a magnetometer was affected by magnetic disturbances. As shown in the purple block, during the magnetic disturbances, the weight of the affected magnetometer was automatically tuned to zero (red circle in subplot 2), and as shown in the red square block (weight of $magnetometer_A$ in subplot 2), the weight of the other magnetometer was tuned to almost maximum because it was not affected by the magnetic disturbances. During the shock, the weight of $magnetometer_A$ was reduced (subplot 2, dark red block) because the errors from the other sensors were temporarily reduced by the shock. Also, after the shock impact, the angles from the gyroscopes drifted (around 10 degrees). Therefore, the weights of the gyroscopes were tuned to almost zero (grey blocks in subplot 4). Finally, the weights of the azimuth angles calculated from 3 different ratio factors were also automatically tuned (subplot 6 in Figure 4.1.10). In addition, subplot 2 in Figure 4.1.10 shows that after the shock impacts, the magnetometers shared large weights (because the other sensors drifted). The data of subplot 2 also show that after the shock, the weight of one magnetometer decreased while the other one's weight increased. The ratio of the training data to the verification data was 5:1.

Figure 4.1.11 shows the error between the proposed method and traditional KFs (the KF of IMU_A is indicated by the red dashed line, and the KF of IMU_B is the black dashed line). The covariance matrices *Q & R* were computed based on the standard deviation value of the first 1000 measurement datum from the gyroscope and magnetometer. The calculated variance values of the covariance matrices *Q & R* were constants during the KF computation process. The drift in the final KF outputs was due to the weight calculation based on the covariance matrices; KFs determined that the gyroscopes were more trustable than the magnetometers. Therefore, when the gyroscopes drifted (caused by the shock impacts), the final KF outputs drifted too. To investigate the influences of the magnetic interferences, we assumed the gyroscope error caused by the shocks was known and put the gyroscope error into the *Q* matrix. Figure 4.1.12 shows that KF_A was unaffected by the shock disturbances because the magnetometer provided relatively accurate information ($magnetometer_A$ was not affected by magnetic interferences). However, KF_B shows large errors caused by the unknown magnetic interferences because the errors were not put into the *R* matrix. The black dashed circles indicate the errors during the magnetic interferences. The absolute maximum error (AME) of SLF is 0.98 degrees, and the AME of KF is 11 degrees (Figure 4.1.11) and 47 degrees (Figure 4.1.12). With proper training, the redundant IMU design and proposed method are minimally affected by magnetic disturbances and shock impacts. However, the KFs are more affected by the unknown disturbances.

Magnetic Interference and Shock Impact (Second Case Study)

Figure 4.1.13 shows the SLF results of the second case study where all sensors are influenced; the red circles show the response of the filter to the magnetic disturbances.

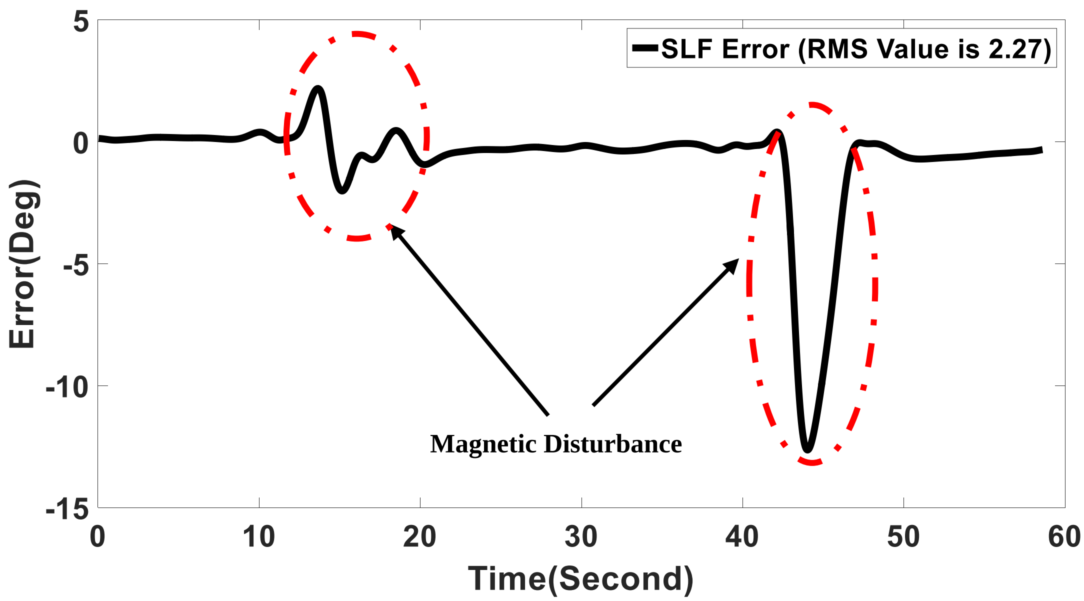

Figure 4.1.13 The proposed SLF method (if all sensors are not accurate, the performance of the ANFIS method is reduced)

The results show that the sensors were more affected in the second case study compared to the effect on the sensors in the first case study, as shown in Figure 4.1.13. During the disturbance time intervals (the red circles), the sensors did not compensate for one another because of the small weight caused by the large errors in all sensors.

4.1.4 Verification

To verify the proposed method, we used two additional sets of tests. The new cases were verified without further training. A single movement and disturbance were used to verify the performance of the SLF filter. The moving was divided into two single movements, one for inclination and one for azimuth (implemented at different times). Also, the shock and magnetic disturbances were added to the two single movements separately. For the first verification case, the magnetic disturbance was only added in the inclination movement, and the shock disturbance was only added in the azimuth movement. Then, for the second verification case, the magnetic disturbance was added to the azimuth movement, and the shock disturbance was added to the inclination movement.

Verification Case 1

For the first verification case (Figure 4.1.14), there were two movements: 90 degrees inclination (1^{st} step) and 90 degrees azimuth back and forth (2^{nd} step). First, the rotation arm was rotated from 0 degrees (vertical to the ground) to 90 degrees (horizontal) on the inclination plane. During this step, the azimuth angles were kept constant and only the inclination angles changed. In this inclination rotation, a magnetic disturbance was added to IMU_B. The magnetic disturbance (applied using a magnet) was perpendicular to the inclination plane with a distance 0.3 meters between the magnet and IMU_B. After the first step finished, the rotation arm only rotated around the rotation center of the horizontal plane from 0 degrees to 90 degrees (back and forth). Also, a shock hammer was used to simulate a shock impact at 0.15 meters distance from IMU_A during the azimuth rotation. The hit direction was horizontal to the azimuth rotational plane and vertical to the rotational arm. Figure 4.1.16 shows the shock force implemented by a shock hammer (PCB 208. A03). The magnitude of the force was about 500N with only one hit.

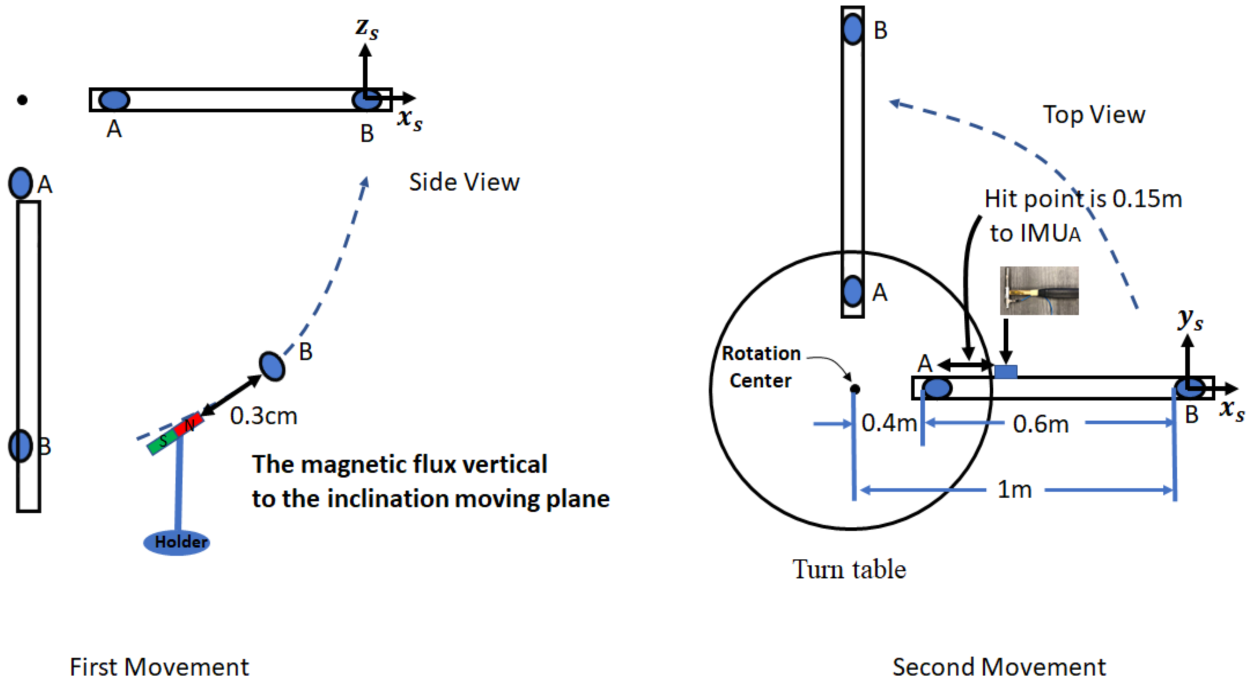

Figure 4.1.14 Movement plan of verification case 1

Figure 4.1.17 shows the results of the SLF azimuth estimation for verification case 1. The magnetic disturbance was implemented during the inclination process and caused a 40 degree deviation (Magnetometer$_B$, Figure 4.1.15); the SLF reduced the deviation from 40 to 1.5 degrees as shown in subplot 1 of Figure 4.1.17. In verification case 1 without training, the SLF performance degraded from 0.259 to 2.227 (RMS value), and the maximum value of the error was 14 degrees.

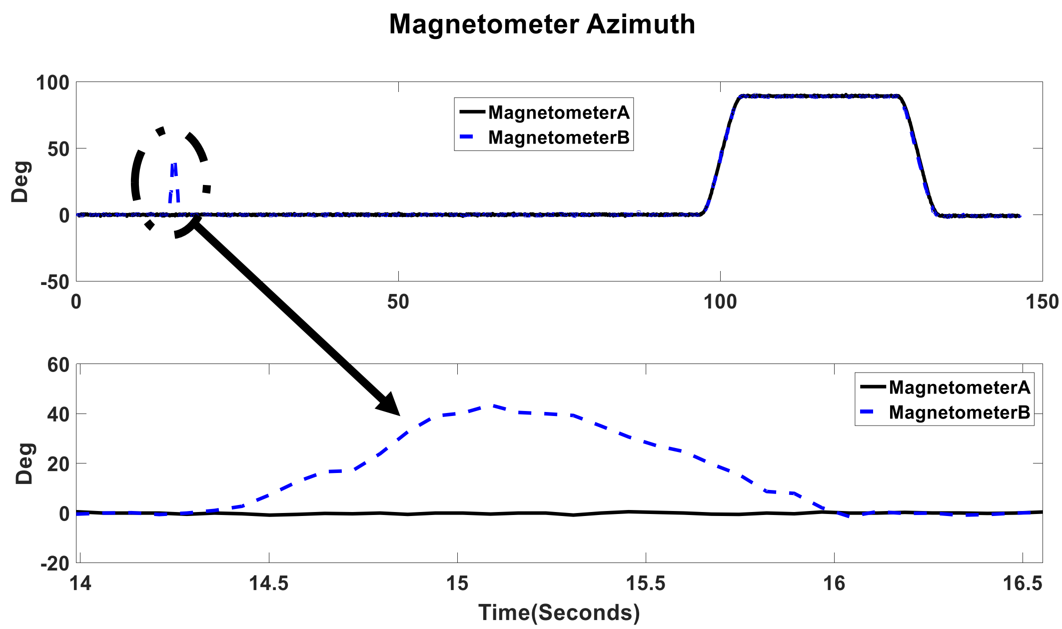

Figure 4.1.15 The magnetometers in verification case 1

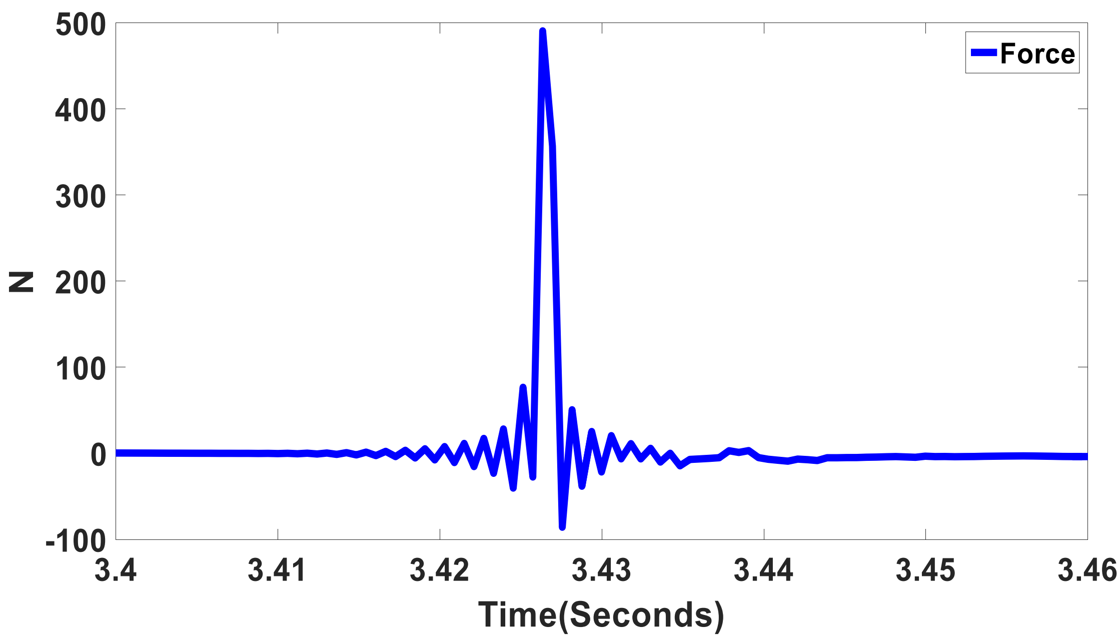

Figure 4.1.16 Shock force in verification case 1

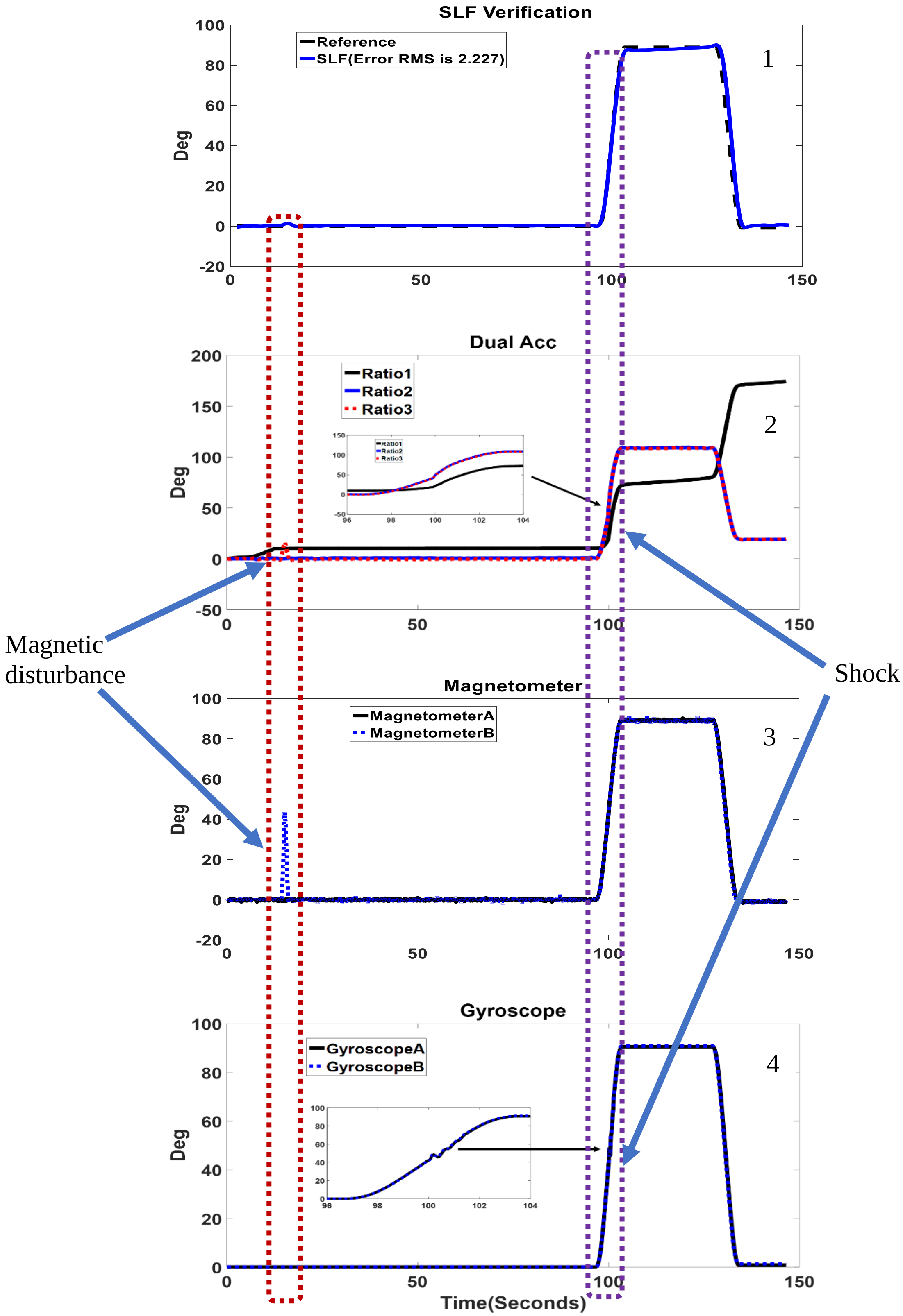

Figure 4.1.17 SLF performance in verification case 1

Verification Case 2

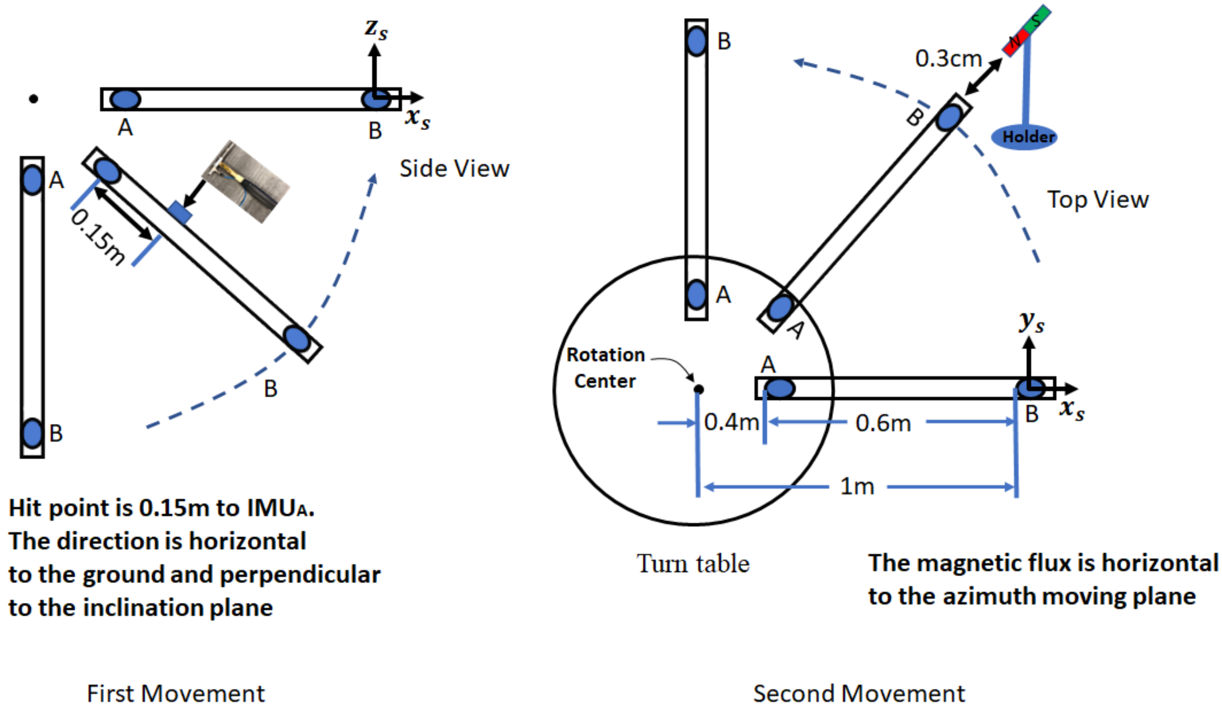

Figure 4.1.18 Rotational plan of verification case 2

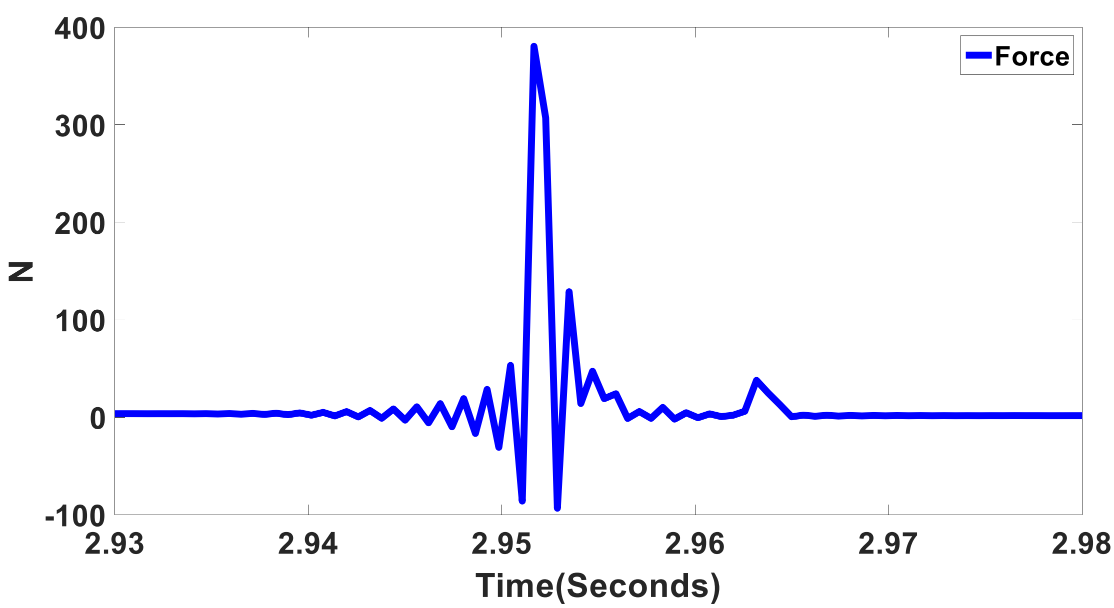

Figure 4.1.19 Shock force in verification case 2

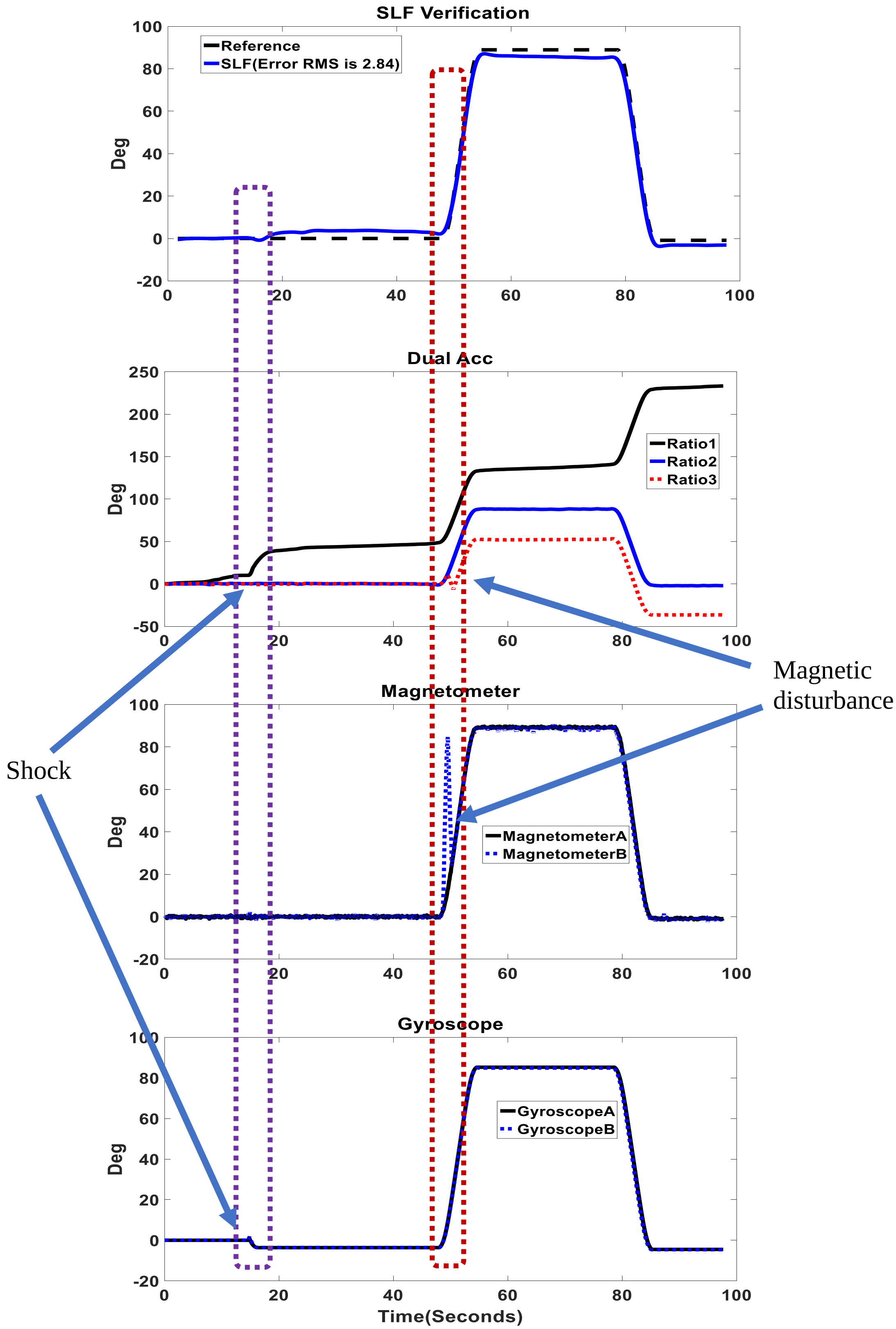

Figure 4.1.20 SLF performance in verification case 2

For the second verification case (Figure 4.1.18), there are two movements: 90 degrees inclination (1^{st} step) and 90 degrees azimuth back and forth (2^{nd} step). First, the rotation arm was rotated from 0 degrees (vertical) to 90 degrees (horizontal) on the inclination plane. During this step, the azimuth angles were kept constant and only the inclination angles changed. In this inclination rotation, a shock hammer was used to simulate an impact 0.15 meters from IMUA in the azimuth rotation. The hit direction was parallel to the azimuth rotational plane and was perpendicular to the inclination plane. After the first step finished, the rotation arm was only rotated around the rotation center of the horizontal plane from 0 degrees to 90 degrees (back and forth). Also, a magnetic disturbance (applied using a magnet) was added to IMU_B. The magnet was on the azimuth plane 0.3 meters from IMU_B.

Table 4.1.2 Verification Disturbances Specification

	Study Case1		Verification1		Verification2	
Disturbances	Shock	Magnetic	Shock	Magnetic	Shock	Magnetic
MagnetometerA	×	×	×	×	×	×
MagnetometerB	×	○	×	○	×	○
GyroscopeA	○	×	○	×	○	×
GyroscopeB	○	×	○	×	○	×
Dual Acc Ratio1	○	×	○	×	○	×
Dual Acc Ratio2	○	×	○	×	×	×
Dual Acc Ratio3	○	○	○	×	×	○

Figure 4.1.20 shows the results of the SLF azimuth estimation of verification case 2. The magnetic disturbance was implemented in the azimuth rotation and caused an 80 degree deviation

(Magnetometer$_B$). In verification case 2 without training, the SLF performance degraded from 0.259 to 2.84 (RMS value), and the maximum value of the error was 5 degrees.

Table 4.1.2 shows the effect of the shock and magnetic disturbance in case study 1 (with training) and verification case 1 and verification case 2 (without training). The O means with disturbance influence, and the × means without disturbance influence.

Comparing these two verification cases without further training shows the proposed SLF method performs less well in verification cases 1 and 2. Consequently, the disturbances in the verification cases are reduced under training conditions.

4.1.5 Summary

In this section, we first used two acceleration difference values to increase the redundant rotation information, similar to what gyroscopes can provide, in cases that have no gyroscopes. However, direct applications of this idea cause large errors because of accelerometer noise and low robustness to shock impacts. To improve accuracy and robustness, we proposed using an SLF. All azimuth angles from the magnetometers, gyroscopes, and accelerometers were compared, and their relative errors were put into the ANFIS to build error models. The final weights of each sensor were calculated according to the outputs of each error models.

The proposed method performs well under the assumed conditions: 1) the reference angle can be obtained, 2) only one magnetometer is affected by magnetic disturbances during a specific time interval, 3) two IMUs rotate at one end of the rotation center, and 4) this method is only applied under similar conditions in a training environment. The unknown magnetic and shock disturbances that caused angle errors are corrected by the proposed fusion method. However, under the worst conditions (all sensors are not accurate), the error cannot be sufficiently reduced.

The proposed method was verified using two verification cases. In unknown application environments, without further training, the performance of SLF degraded from 0.259 (RMS error value) to 2.227 (RMS error value of verification case 1) and 2.84 (RMS error value of verification case 2). This research outcome can be extended to industry level field applications. For example, the outcome can be combined with drilling survey data (used as a reference) to increase the continuous wellbore positioning accuracy.

4.2 Shock and Magnetic Robustness of SL-KF (Fusion Method 2)

MEMS sensors for subsurface navigation consist of accelerometers, gyroscopes, and magnetometers [Renaudin et al., 2014]. Combining these sensors with KFs reduces the effect of noise and known magnetic disturbances, allowing for accurate inclination and azimuth angles to be obtained [Qu et al., 2017]. In many situations, the magnetic disturbances are unknown, and traditional KFs cannot filter out unknown disturbances. Furthermore, shocks can cause drift displacements in integral computations of angular speed that are difficult to correct without an extra reference signal.

The problem of orientation estimation with MEMS IMUs is low robustness to magnetic and shock disturbances, especially in the case that all sensors are subjected to the disturbances. Section 4.1 introduced the SLF method, which had a high robustness to magnetic and shock disturbances. However, the limitation of the SLF method is that it may not perform well if all sensors are affected simultaneously. To increase robustness to these disturbances, we combined the proposed SLF method with a KF. In this design, ANFIS is also utilized to update adaptive covariance matrices of the KF to reduce the effect of unknown magnetic and shock disturbances on the KF. Finally, this proposed method is verified using a lab test rig.

4.2.1 SL-KF Design

For a traditional KF fusion design, gyroscope data integral computation are built as the system model of the KF; azimuth angles from magnetometers and inclination and roll measurements from accelerometers are used in the measurement model [Liu et al., 2018]. However, the gyroscopes are subjected to shock impacts, and the magnetometers are affected by magnetic disturbances. Without proper co-variance matrices, Q & R, the KF cannot accurately produce proper output values. Therefore, the ANFIS is applied to design the proper co-variance matrices of the KF to increase the robustness of the KF to shock and magnetic interferences.

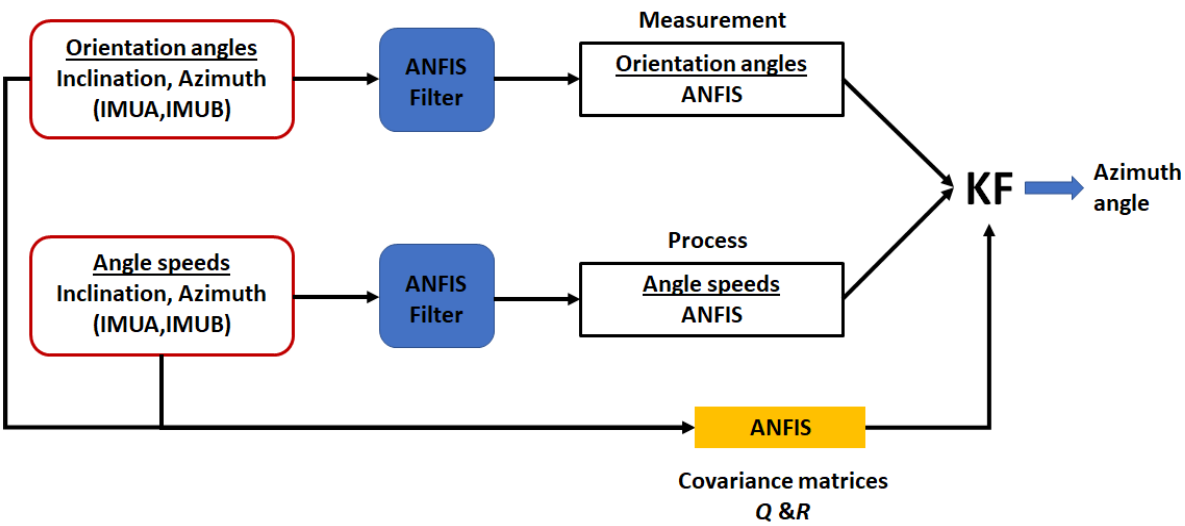

Figure 4.2.1 Supervised learning KF design

Measurement States Computation of Proposed KF

Unlike the inclination angles obtained from the gravity elements of accelerations, the azimuth angles from magnetometers suffer from magnetic disturbances. For MWD in directional drilling, the orientation angles can be measured using accelerometers (inclination), gyroscopes (inclination and azimuth angles through integral calculation) and magnetometers (azimuth). In addition, if gyroscopes are absent, several sets of rotational angles can be obtained using a dual acceleration difference method. The details of how to obtain the angles are presented in Section 4.1.

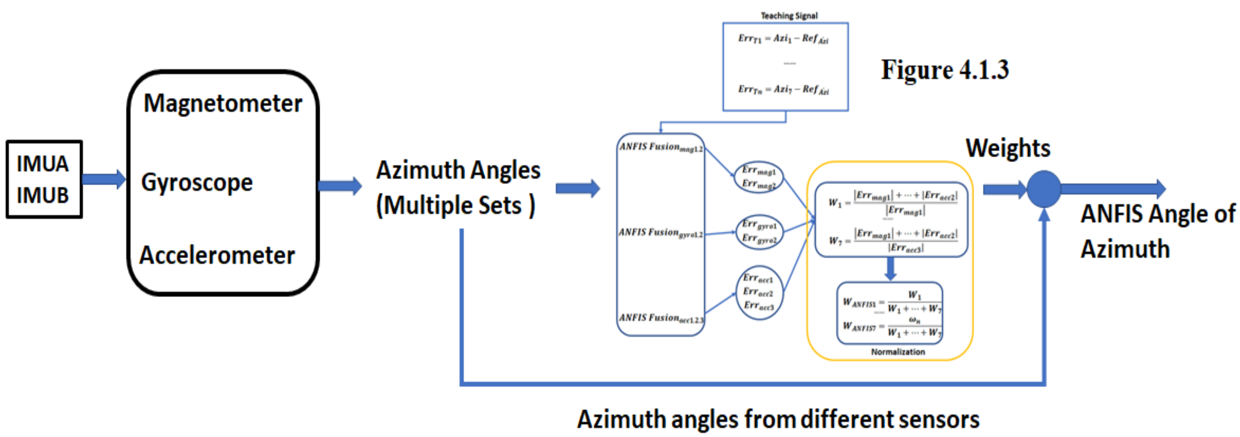

Figure 4.2.2 Measurement states calculation structure of the KF

For a traditional KF azimuth estimation, the measurement states are obtained from magnetometers, which are affected by magnetic disturbances. To reduce the effect of magnetic disturbances, we employ the azimuth information obtained from gyroscopes and two accelerometers; in addtion, we use redundant magnetometers (two sets) separated by a constant distance and located on a rigid body. The SLF method introduced in Section 4.1 is employed to calculate the proper weights of each azimuth angle from different sensors. In this method, when one magnetometer is influenced by magnetic interference, the weight of the magnetometer is tuned to be small, and the weights of the gyroscopes and accelerometers are set as heavier. However, if the gyroscopes and accelerometers suffer from shocks, the weights should be tuned to be small as well. In this situation, there is still one more magnetometer that can provide accurate values since the distance between these two magnetometers reduces the effect of the shock and, in addition, magnetometers are robust to shock impacts. Therefore, the weighted average of these azimuth angles from different kinds of sensors can remove the inaccuracy caused by magnetic and shock disturbances.

Figure 4.2.2 shows how to obtain the azimuth angles that are used as measurement states of the proposed KF, based on the ANFIS error models as shown in Figure 4.1.3. The angles from different sensors are estimated using the ANFIS error models; further, the weights are calculated using these error amplitude value ratios. Finally, these calculated weights are added to each orientation angle from different sensors to obtain the final fused azimuth and inclination.

The orientation angles measured from magnetometers, gyroscopes, and accelerometers are compared with a reference to calculate the errors as teaching data sets for training. For lab-scale tests, these reference signals are converted from the encoders of the motors mounted on the test rig.

Process States Calculation of Proposed KF

As shown in Figure 4.2.1, the rotational velocity information obtained from different sensors is compared to calculate the relative difference values; then, these difference values are input to ANFIS to build the angular velocity error model. The outputs of the ANFIS are the angular velocity errors of the sensors, and based on the magnitude of these errors the weight of each sensor can be calculated.

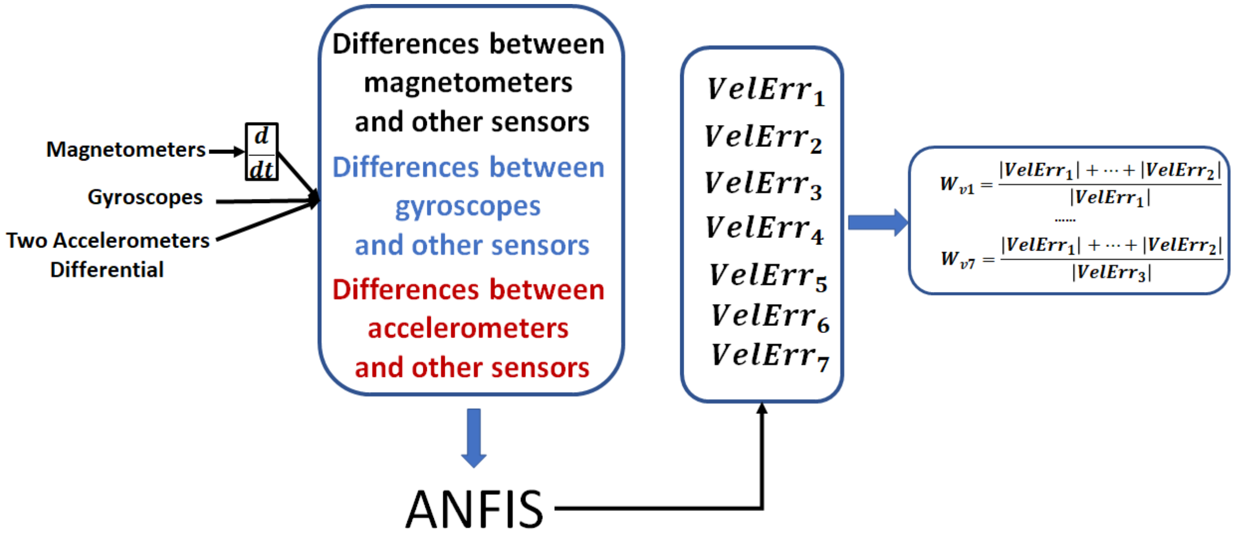

Figure 4.2.3 Designed fusion structure of rotational velocity (azimuth example)

The calculation is shown in Figure 4.2.3. First, angular velocity errors are outputted from ANFIS error models, and then the weight of each sensor is calculated. Finally, the calculated weights are put on different orientation angles to obtain the proper fused azimuth angle velocities, $\dot{\theta}_z$, which are used for the process states calculation of the proposed SL-KF.

<u>Covariance Matrices Q & R</u>

The final performance of a KF depends on the proper values of the co-variance matrices, Q & R, which are based on a priori information about the process and measurement noises [Basso et al., 2017]. However, unknown magnetic and shock disturbances are different from noise embedded in the sensor itself, which means the calculated error covariance matrices based on sensor noise could be inaccurate. If the reference values of both process and measurement states are known, then the process and measurement uncertainty errors can be derived and put into the KF co-variance matrices for proper weight calculation.

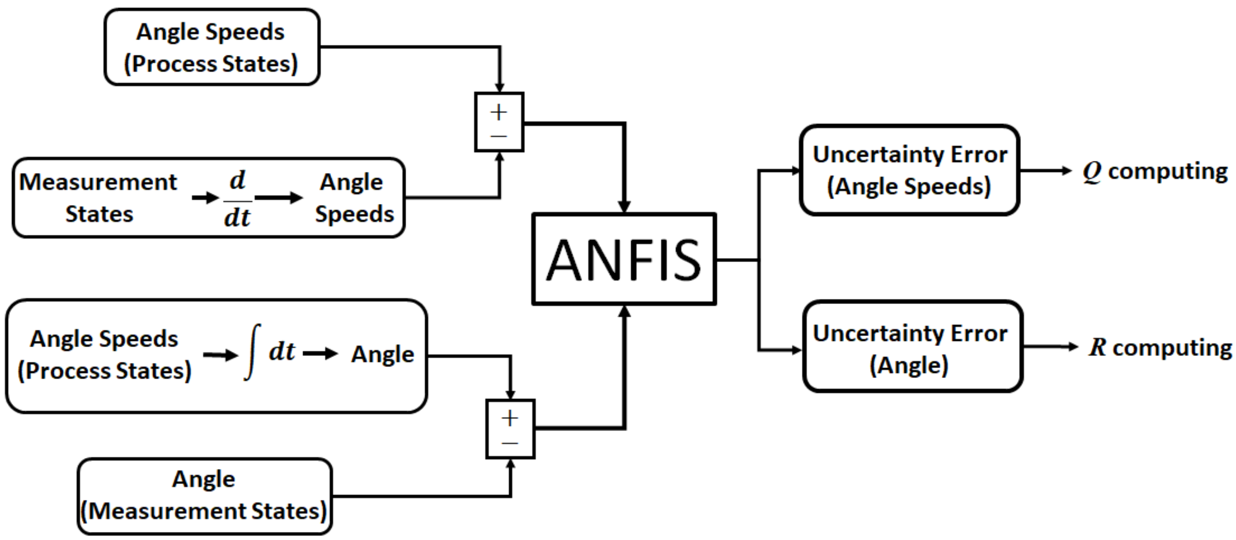

Figure 4.2.4 Uncertatinty error calculation for covariance matrices calculation

To address this problem, we employ ANFIS to build error models for obtaining the process and measurement uncertainty errors. As shown in Figure 4.2.4, the orientation angular speeds and angles from the process and measurement states are compared to obtain the differences between them; then, these differences are inputted into ANFIS to compute the uncertainty errors, which are then used in the co-variance matrices of the SL-KF.

4.2.2 Discussion of Lab-scale Evaluation and Results

<u>Movement Plan of Lab Test</u>

To compare the performance of the SL-KF with the SLF, we used the same experimental approaches (Section 4.1.3) to evaluate the SL-KF method. The test process is described here for a quick review. Two IMUs were mounted on the arm of a test rig a constant distance *D* (0.6 meters) apart. The orientation of each IMU was measured using tri-axes gyroscopes, accelerometers, and magnetometers; there were 3 of each kind of sensor, one located on each axis x_s, y_s, and z_s axes. The two IMUs were configured with a known distance *D* to reduce magnetic disturbances. Also, distance *D* was used to calculate the rotational angular speeds with two sets of tri-axes accelerometers.

To investigate this method, we designed a 3D test track that includes inclination and azimuth (Figure 3.3.5). This 3D movement trajectory was a combination of two 2D orientations on the azimuth or inclination plane. Two IMUs were located on the rotation arm of the test rig, and the arm moved from vertical (inclination=0 deg) to horizontal (inclination=90 deg) on the inclination plane as shown with the grass dashed line in Figure 3.3.5. The red and yellow points in the figure are the start positions of the azimuth and inclination. The purple point is the end position. At the same time, the center axis rotates 90 degrees on the horizontal plane as shown with the red dashed line (from yellow point to purple point). Both 2D rotational movements have the same rotational center (the black point). The black solid line is the combined 3D test track that includes the inclination and azimuth. The encoders mounted on the motors provide the reference signals that are compared with the measured orientation angles. Two IMUs (A & B) are mounted on the rotation arm of the rig. The IMU axis z_s is pointed to the sky, the axis x_s is pointed to the outside of the rotation center and the axis y_s is perpendicular to the x_s and z_s plane.

Lab-scale Test and Results Discussion

Without proper a priori information, a KF does not sufficiently filter out magnetic and shock disturbances. A hybrid with ANFIS and the *Q & R* matrices of the SL-KF can address this issue and obtain proper error information. Lab-scale tests with a test rig were implemented to evaluate the performance of the SL-KF. During the lab tests, the robustness of the method to magnetic and shock disturbances was investigated. The shock test data and the magnetic disturbance values are shown in Figure 4.1.5 in Section 4.1.

As in Section 4.1, two cases were studied. For the first case, it is assumed that at least one magnetometer is not negatively influenced because of the distance that separates the magnetometers. In the second case study, it is assumed that all sensors are influenced by disturbances (magnetometers are affected by magnetic disturbances and gyroscopes and accelerometers are affected by shocks), and no accurate measurement values are obtained from the sensors at the same time.

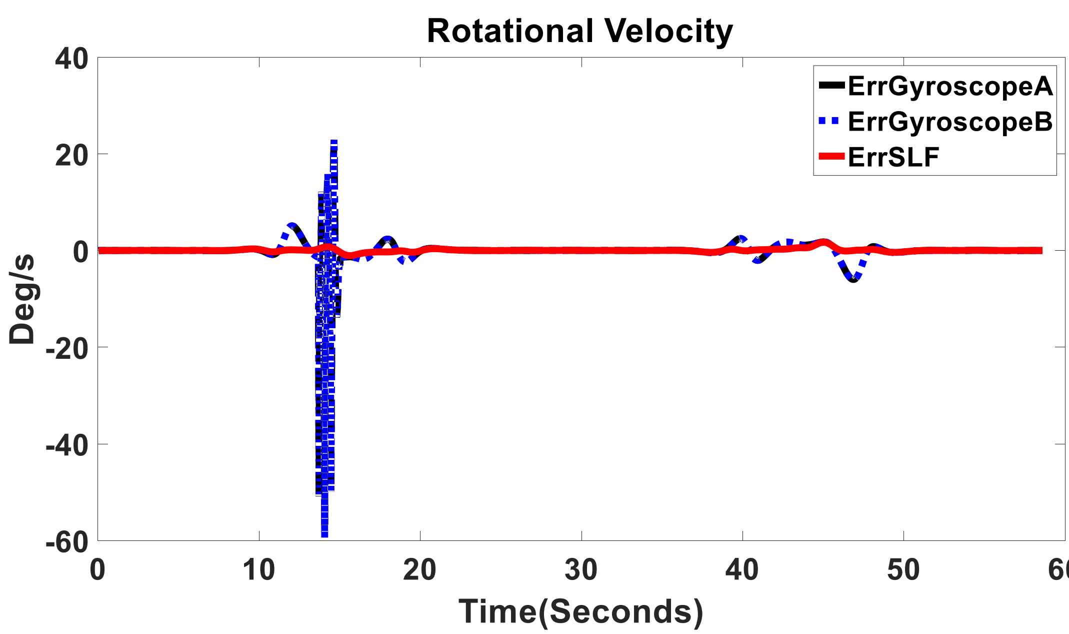

Figure 4.2.5 Speed error comparison (first case study)

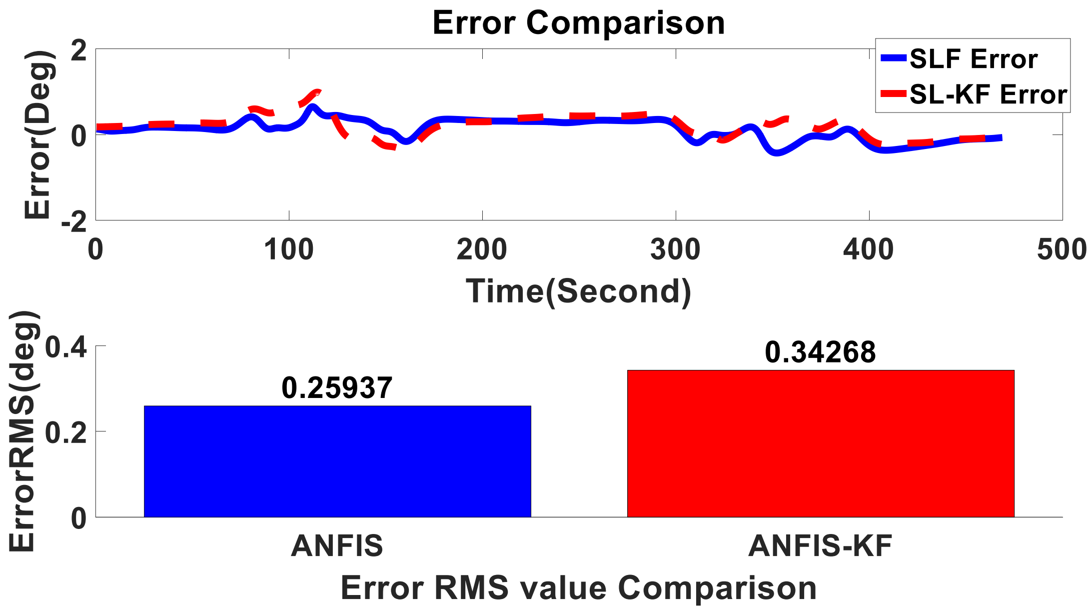

Figure 4.2.6 Final angle error comparison (first case study)

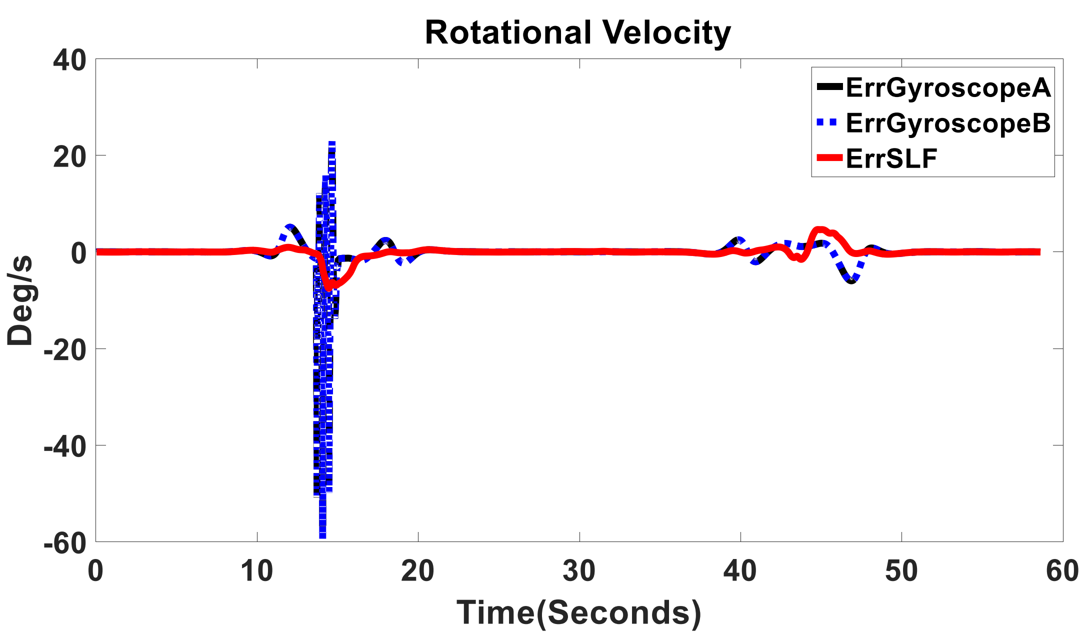

Figure 4.2.7 Speed error comparison (second case study)

Figure 4.2.5 shows the rotational speed error comparison of the SLF output and two gyroscopes in the first case. The SLF outputs corrected rotational speed because the magnetometer that is not exposed to magnetic interferences can correct the errors caused by the disturbances. Figure 4.2.6 shows the angle error comparison between SLF and SL-KF in the first case study. As shown, the SL-KF obtains proper error information to calculate the Q & R matrices and correct the magnetic and shock disturbances.

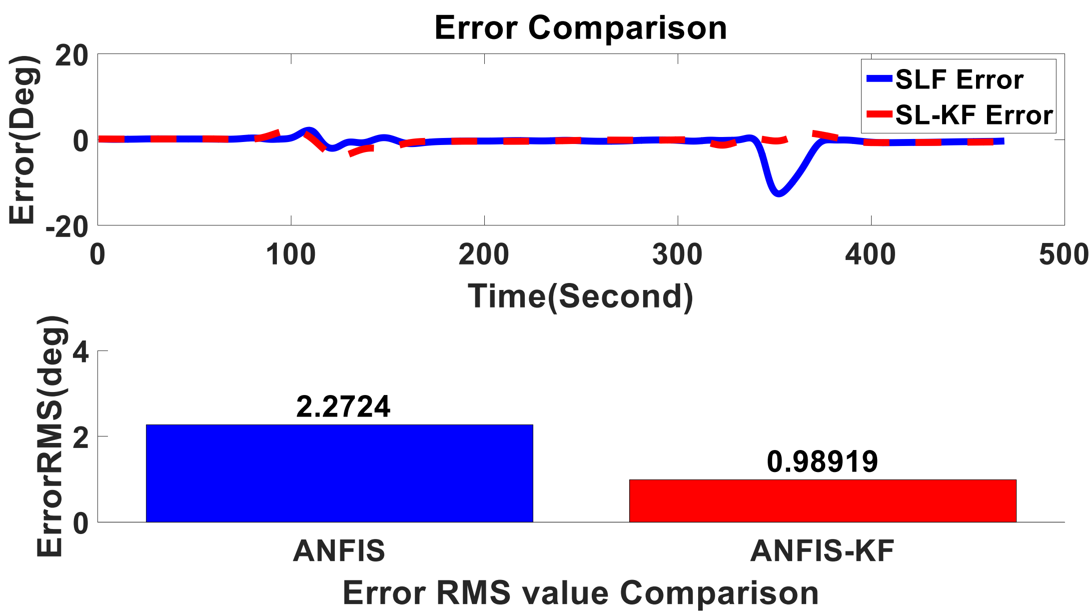

Figure 4.2.8 Final angle error comparison (second case study)

In the second case study, for rotational angle speed compensation, SLF does not properly correct the error caused by magnetic and shock disturbances, but it may reduce the negative influence as shown in Figure 4.2.7. Because of the limitation (all the sensors are affected), the SL-KF does not achieve the same performance as in the second case as it does in the first case study (first case: 0.34268). However, in the second case, the SL-KF performs better (56% better performance as indicated by the RMS value, Figure 4.2.8) compared to the SLF.

In this section, an SL-KF is proposed to increase robustness to magnetic and shock disturbances under the assumptions that all the sensors are affected. An SLF was employed as a local filter to determine the rotational angular speeds and angles that were used as inputs in the global filter (KF). All angles and angular speeds from the magnetometers, gyroscopes, and accelerometers were compared, and the relative errors were put into the ANFIS to build error models. The final weights of each sensor were calculated according to the outputs of the ANFIS error models.

The proposed SL-KF method performs better compared to the proposed SLF filter method, assuming the following conditions: 1) the reference angle can be obtained, 2) two IMUs rotate at one end of the rotation center, and 3) this method will be applied under similar conditions in a training environment. Even in the worst scenario (all sensors are inaccurate), the proposed SL-KF fusion method corrected 56% more errors caused by unknown magnetic and shock disturbances than in the SLF method.

4.2.3 Verification

To verify the SL-KF method, we used two case studies. First the SL-KF method was trained using a combined movement (inclination and azimuth move simultaneously) and a combined disturbance (simultaneous magnetic and shock disturbance). Therefore, to verify the performance of the SL-KF filter in different movements and disturbances, we divided the combined movement into two single movements that included inclination and azimuth (they were implemented at different times). Also, the shock and magnetic disturbances were applied to the two single movements separately. For the first verification case, the magnetic disturbance was only added in the inclination movement, and the shock disturbance was only added in the azimuth movement. For the second verification case, the magnetic disturbance was only added in the azimuth movement, and the shock disturbance was only added in the inclination movement.The details of the verification tests (1 & 2) were described in Section 4.1.4.

<u>Verification Case 1</u>

For the first verification case, there were two movements: 90 degrees inclination (1st step) and 90 degrees azimuth back and forth (2nd step). First, the rotation arm was rotated from 0 degrees (vertical to the ground) to 90 degrees (horizontal) on the inclination plane. During this step, the azimuth angles were kept constant, and only the inclination angles changed. For this inclination rotation, a magnetic disturbance was added to IMU_B. The magnetic disturbance (applied using a magnet) was perpendicular to the inclination plane and at a distance of 0.3 meters from IMU_B. After the first step finished, the rotation arm only rotated around the rotation center of the horizontal plane from 0 degrees to 90 degrees (back and forth). Also, a shock hammer was used to shock a point 0.15 meters from IMU_A during the azimuth rotation. The hit direction was horizontal to the azimuth rotational plane and vertical to the rotational arm.

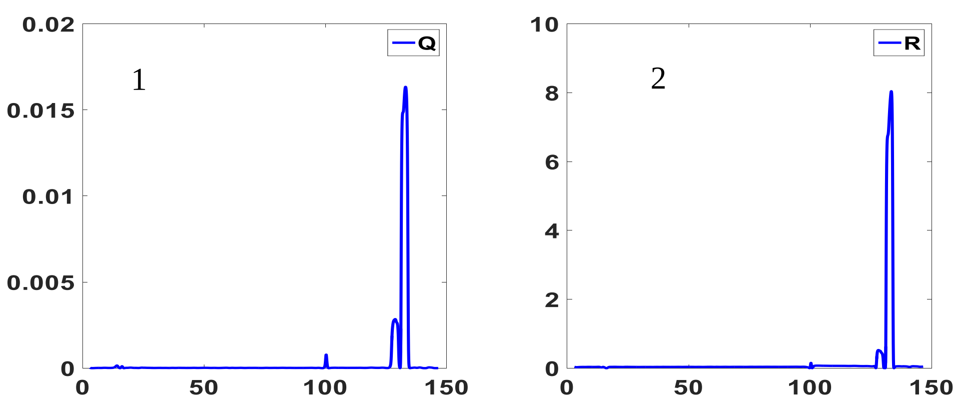

3

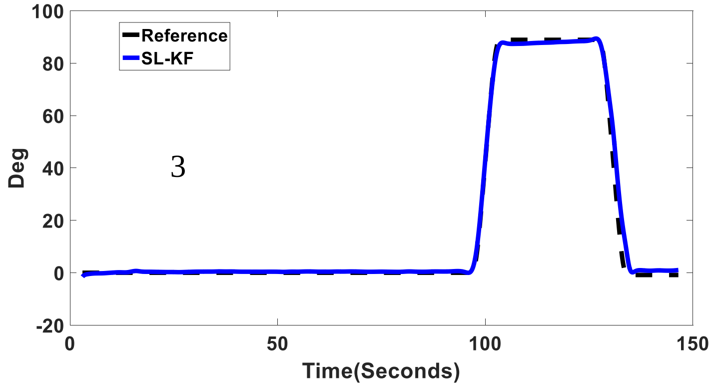

4

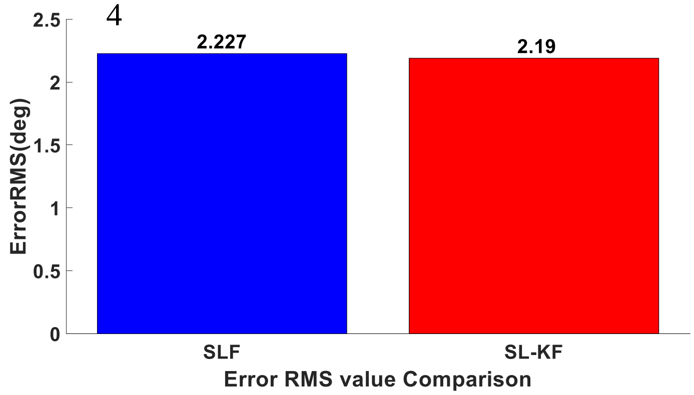

Figure 4.2.9 Performance of SL-KF (verification 1)

Figure 4.2.9 shows the performance of the SL-KF in verification1. Subplot 1 & 2 show the values of Q & R of the SL-KF. Subplot 3 shows the final output of the SL-KF in verification 1. Subplot 4 compares the error RMS values of SLF and SL-KF. The comparison shows that SL-KF performs as well as SLF in this scenario.

Verification Case 2

For the second verification case (Figure 4.1.18), there were two movements: 90 degrees inclination (1st step) and 90 degrees azimuth back and forth (2nd step). First, the rotation arm was rotated from 0 degrees (vertical) to 90 degrees (horizontal) on the inclination plane. During this step, the azimuth angles were kept constant, and only the inclination angles changed. In this inclination rotation, a shock hammer was used to hit a point 0.15 from IMU_A. The hit direction was parallel to the azimuth rotational plane and was perpendicular to the inclination plane. After the first step finished, the rotation arm only rotated around the rotation center of the horizontal plane from 0 degrees to 90 degrees (back and forth). Also, a magnetic disturbance (applied using a magnet) was added to IMU_B. The magnet was on the azimuth plane 0.3 meters from IMU_B.

Figure 4.2.10 shows the performance of the SL-KF in verification 2. Subplot 1 & 2 show the values of Q & R of the SL-KF. Subplot 3 shows the final output of the SL-KF in verification 2. Subplot 4 compares the error RMS values of SLF and SL-KF. The SL-KF performed better than the SLF (up 45%) based on the error RMS value comparison.

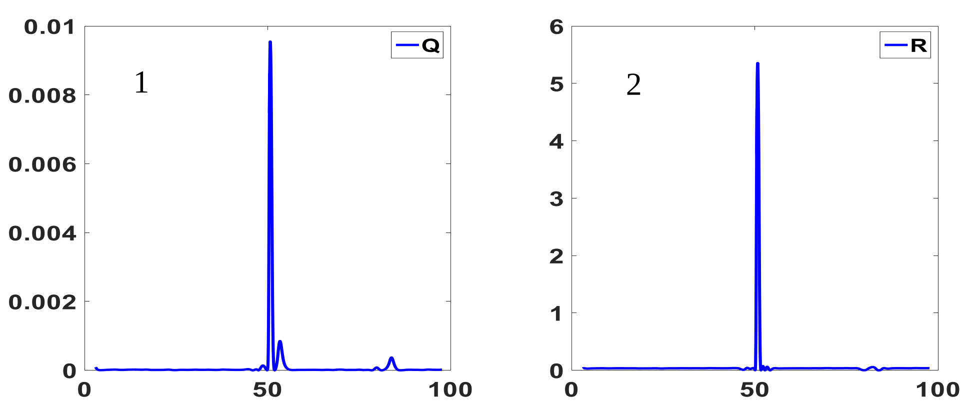

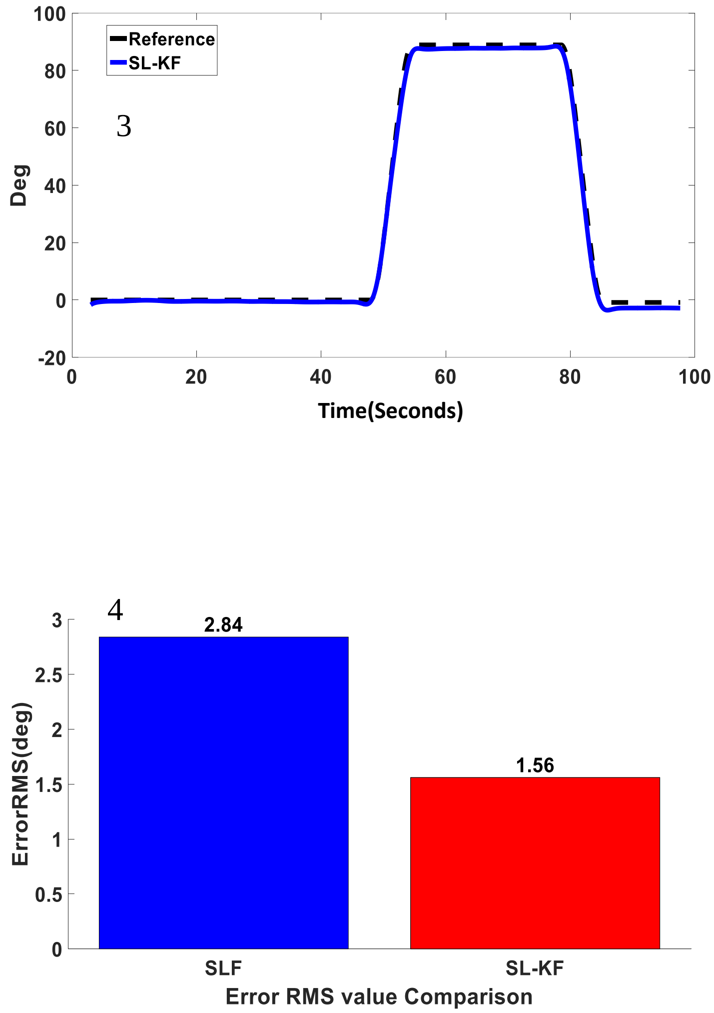

Figure 4.2.10 Performance of SL-KF (verification 2)

4.3 Summary

This chapter discusses how to increase robustness to magnetic and shock disturbances for subsurface orientation angle sensing. A two-level structure filter (local and global) with redundant IMUs (two sets) were used; these IMUs were mounted on a rigid body and were separated by a known distance *D* (0.6 meters). The traditional and supervised learning filter methods (KF and

SLF) were employed to achieve the research objectives. The advantages and disadvantages of these methods are summarized in Table 4.3.1.

Table 4.3.1 Pros and cons of SLF and SL-KF

Fusion Methods	Pros	Cons
SLF (1st)	*Dual acceleration difference method provides redundant rotation angular speeds. *High robustness to unknown magnetic and shock disturbances.	*When all sensors are disturbed, robustness degrades. *Need previous training.
SL-KF (2nd)	*Higher robustness (Up 56%) than SLF (1st).	*Extensive, complex calculations. *Need previous training.

To reduce the effect of magnetic and shock disturbances, we compared the angle errors from different sensors (magnetometers, gyroscopes, and accelerometers) under magnetic and shock disturbance conditions and employed ANFIS to obtain error models of each sensor (Section 4.1). Based on these error models, the proper weights of the sensors were computed and added to different sensors. It was assumed that at least one magnetometer was unaffected by interferences during the same time interval to achieve the best performance of the SLF. When both magnetometers were affected simultaneously, the performance of the SLF was degraded because the sensors could not provide accurate references since they were affected by the disturbances during the same time interval.

An SL-KF was designed to further increase robustness in the scenario where all sensors were affected, as shown in Section 4.2. First, the SLF method was used to compute the corrected rotational angles and angular speeds; these values were then fed into a KF (used as a global filter) for further corrections. The lab-scale test results showed that the proposed SL-KF increased robustness by up to 56% in the worst case (all sensors were affected) compared with the SLF method.

Lastly, we verified the designed filters (SLF and SL-KF) using two different case studies. The performance of both SLF and SL-KF was degraded in both cases because the ANFIS error models were without further training in these case studies. The SL-KF performed better than the SLF in both cases.

CHAPTER 5. POSITION FUSION METHODS

Subsurface sensing evaluates the performance of subsurface industry activities. The sensors used in subsurface industry activities must provide proper orientations and positions. For subsurface activities, orientation information is usually detected by one or more micro-electro-mechanical system (MEMS) inertial sensors, which consist of multi-axis accelerometers, gyroscopes, and magnetometers. The orientation information shows the sensor attitudes to the measurement process and reflect the changing states of the subsurface.

For a position measurement, accelerometers are primarily used to measure the dynamic acceleration; then, the acceleration measurements are used to compute the travel distance through double integral computation. The moving velocity can also be calculated during this integral calculation procedure [Axelsson et al., 2012]. For this traditional acceleration double integral calculation method, the DC components and disturbances embedded in the acceleration measurements may cause drift during the process of integral calculation [Latt et al., 2011].

In subsurface position tracking, it is difficult to utilize external location correction sensors such as GPS [Tarokh 2007]. Therefore, the biggest challenge to position tracking is dealing with insufficient information resources, for example, in the case of using accelerometers without the assistance of extra correction sensors such as GPS or cameras. In this case, noise and the DC components contained in acceleration signals and shocks on the accelerometers can cause drifts in position estimation in a long-term double integral calculation of accelerations.

5.1 Dual Acceleration Difference KF (Lab-scale Position)

The movements of an IMU sensor can be divided into translational and angular movements. Typical scenarios of application include longitudinal and lateral maneuvers. Unlike traditional methods that obtain position correction using GPS, the IMU is mainly used in subsurface environments where GPS signals are unavailable. In this scenario, translational movement displacement may only be calculated using double integral calculations of the acceleration signals. If the rotational movements are included, the accelerometers' measurements are classified into tangential and centripetal accelerations. The centripetal accelerations determine moving directions, and the tangential accelerations determine moving distances. Without identifying the centripetal and tangential elements of accelerations, the double integral calculation method may obtain incorrect results. Also, although the DC components embedded in accelerations may be removed using high pass filter, the drifts caused by shocks still remain.

To deal with these problems, this section develops a position measurement system using redundant sets of accelerometers and polar coordinates. A Kalman filter (DAD-KF) is proposed to improve the robustness to the shock disturbances for position estimations.

5.1.1 Displacement Calculation without Filter

The basic position calculation method for an IMU accelerometer is double integral computation. However, using double integral computation to obtain displacement requires identifying the tangential elements from the raw acceleration signals for a curvilinear movement. Without identification, the centrifugal elements of the accelerations can cause errors in position computations because centrifugal (or centripetal) accelerations only contribute to the change in the moving direction. The other method to calculate positions is based on the rotation radii estimation of the curvilinear movements. In a polar coordinates, the arcs of curvatures can be obtained from rotational radii and angles. In addition, the rotation radius ρ is crucial to convert polar coordinates to Cartesian coordinates. This section also shows how to calculate redundant positions using radius ρ from different sensors.

Polar Coordinates and Cartesian Coordinates

There are few cases in industry applications where a sensor's movement between two points is a straight line because curvilinear motions occur much more often than pure linear movements in reality. A curvilinear movement can be modeled as a trajectory that is approximated by a sequence of circular arcs. These circular arcs can be calculated using double integral calculations of tangential accelerations (the centripetal accelerations are not included). If GPS is used for corrections, identifying tangential accelerations is not necessary since the components that do not contribute to position change can be considered as noise and removed by filters. For applications that use only accelerometers, the influence of centripetal accelerations should be considered.

For a rotational motion in 3D spherical coordinates (Figure 5.1.1), the position values of an IMU are given as follows:

$$x = \rho sin\theta_y cos\theta_z \tag{5.1.1}$$

$$y = \rho sin\theta_y sin\theta_z \tag{5.1.2}$$

$$z = \rho cos\theta_y \tag{5.1.3}$$

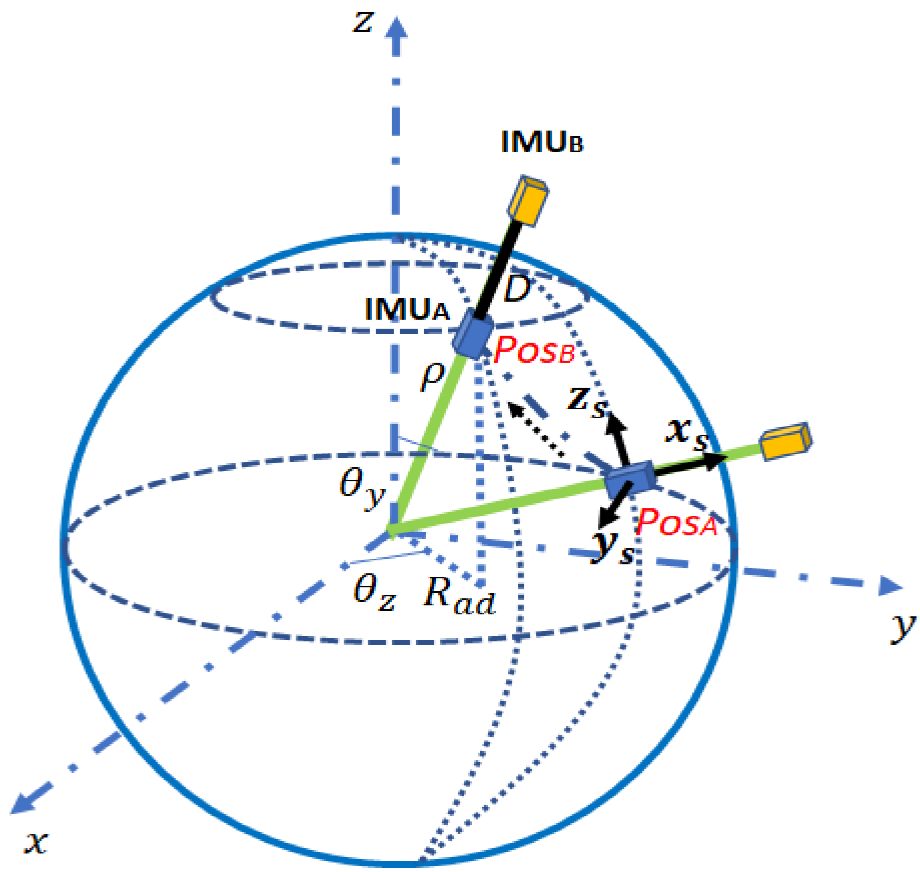

Figure 5.1.1 Moving displacement in polar coordinates

The spherical radius, ρ, shows the distance between a moving object and the rotational center, where θ_y (inclination angle) represents the angle between the positive *z*- axis and the line from the rotation center to the moving object. Also, θ_z (azimuth angle) is the angle between the positive *x*- axis and the line denoted by R_{ad}, which is the projection of ρ on the horizontal x, y plane. The following relations can be derived:

$$\rho = \sqrt{x^2 + y^2 + z^2} \tag{5.1.4}$$

As shown in the above equations, if the rotational radius (ρ) and orientation angles are known, the positions can be calculated. The different radius calculating methods from different sensors are discussed below.

<u>Radius Calculation Using Double Integral Calculation of Acceleration</u>

As shown in Figure 5.1.1, the movement of IMU_A from point A to B is based on the integral calculation of the tangential elements of accelerations (y_s, z_s), and the centrifugal element (x_s) does not contribute to the magnitude of the distance but only to the changes in direction. Therefore, the first set of positions is derived from the double integral computation of the tangential accelerations. The total moving distance is shown in Equation 5.1.5.

$$S_p = \sqrt{(\iint \ddot{y} dt)^2 + (\iint \ddot{z} dt)^2} \qquad (5.1.5)$$

However, this total moving distance S_p does not clearly show the positions on the *x*, *y*, and *z* axes in Earth coordinates since S_p is a series of arcs in polar coordinates. Therefore, it is necessary to calculate the radii to convert the polar coordinates to Cartesian coordinates. During each time interval, the moving distance is calculated as follows:

$$S_{p,\Delta t} = S_{p,t} - S_{p,t-1} \qquad (5.1.6)$$

For each time interval, the movement track is assumed to be an arc; therefore, the rotational radius is as follows:

$$\rho_{Tangen} = {S_{p,\Delta t}} \Big/ \sqrt{\left(\Delta\theta_y\right)^2 + \left(sin(\theta_y) \times \Delta\theta_z\right)^2} \tag{5.1.7}$$

$S_{p,\Delta t}$ can be obtained from the known measurement depth (drill string length) for directional drilling. For the lab-scale tests, the $S_{p,\Delta t}$ value is calculated using known orientational angles and radii.

<u>Radius Calculation Using Accelerometers and Gyroscopes</u>

As shown in Figure 5.1.1, two IMUs are mounted on a rigid body. The rotational radii are calculated using the measurements of one accelerometer and the rotational angular velocity information from a gyroscope:

$$\rho = \rho_{SingleAccA} = \ddot{x}_{sA} / \left(\dot{\theta}_z^2 + \dot{\theta}_y^2\right) \tag{5.1.8}$$

This calculation method is a combination of accelerometers and other kinds of sensors such as gyroscopes. However, sometimes the industry favors using only accelerometers rather than combining different types of sensors in subsurface activities [Shor et al., 2015]. Due to industry preferences, a radius calculation based on dual accelerometers was also proposed. Because of the configuration of the IMUs, we can obtain the redundant rotational radius from dual accelerometers as follows:

$$\rho = \rho_{DualAccA}, \qquad {(\rho_{DualAccA} + D)} \big/ {\rho_{DualAccA}} = {\ddot{x}_{sB}} \big/ {\ddot{x}_{sA}} \tag{5.1.9}$$

Position Calculation

After the radii are calculated based on Equation 5.1.9, the movement distances in Cartesian coordinates at each time interval are as follows:

$$dx = \rho \times \left[sin\left(\theta_{y,t}\right) \times cos\left(\theta_{z,t}\right) - sin\left(\theta_{y,t-1}\right) \times cos\left(\theta_{z,t-1}\right)\right] \tag{5.1.10}$$

$$dy = \rho \times \left[sin\left(\theta_{y,t}\right) \times sin\left(\theta_{z,t}\right) - sin\left(\theta_{y,t-1}\right) \times sin\left(\theta_{z,t-1}\right)\right] \tag{5.1.11}$$

$$dz = \rho \times \left\{\left[1 - cos\left(\theta_{y,t}\right)\right] - \left[1 - cos\left(\theta_{y,t-1}\right)\right]\right\} \tag{5.1.12}$$

After a sum calculation process, the movement positions in polar coordinates can be derived:

$$x_G = x_c + \sum_{i=1}^{n} dx_i \tag{5.1.13}$$

$$y_G = y_c + \sum_{i=1}^{n} dy_i \tag{5.1.14}$$

$$z_G = z_c + \sum_{i=1}^{n} dz_i \tag{5.1.15}$$

where the subscript c denotes the initial position value.

5.1.2 Displacement Calculation with DAD-KF

Process and Measurement Model of the DAD-KF

The integral calculation used as a process model of the DAD-KF is established from differential equations:

$$\dot{X}_{k+1} = FX_k + GU_k + w_k, w_k \sim N(0, \sigma^2) \tag{5.1.16}$$

$$X = \begin{matrix} [x_{sA} & y_{sA} & z_{sA} & \dot{x}_{sA} & \dot{y}_{sA} & \dot{z}_{sA} \\ x_{sB} & y_{sB} & z_{sB} & \dot{x}_{sB} & \dot{y}_{sB} & \dot{z}_{sB} \\ \Delta x_s & \Delta y_s & \Delta z_s & \Delta \dot{x}_s & \Delta \dot{y}_s & \Delta \dot{z}_s]^T \end{matrix} \tag{5.1.17}$$

where X is the state's vector composed of navigation information and two inertial sensor difference values, F is the system's dynamic matrix, G is the input and noise coefficient matrix, and w_n is the system noise vector of inertial accelerometers. Additionally, x_{sA}, y_{sA}, z_{sA} and $\dot{x}_{sA}$, $\dot{y}_{sA}$, $\dot{z}_{sA}$ are position and velocity values along the *x*, *y*, and *z* axes that are calculated from accelerations measured using accelerometer A. The difference values Δx_s, Δy_s, Δz_s, $\Delta \dot{x}_s$, $\Delta \dot{y}_s$, $\Delta \dot{z}_s$ represent the navigation position and velocity errors between the two accelerometers. The inputs (U) are the acceleration elements, which are double differential values of Equation 5.1.13-15 (the radius value is calculated from Equation 5.1.7; $S_{p,\Delta t}$ is not the measurement depth).

The detailed matrix of F and G are given in Equations 5.1.18-21:

$$F = \begin{bmatrix} F^1_{6\times6} & 0_{6\times6} & 0_{6\times6} \\ 0_{6\times6} & F^2_{6\times6} & 0_{6\times6} \\ I_{6\times6} & -I_{6\times6} & 0_{6\times6} \end{bmatrix} \tag{5.1.18}$$

$$F^1_{6\times6} = F^2_{6\times6} = \begin{bmatrix} 1 & 0 & 0 & dt & 0 & 0 \\ 0 & 1 & 0 & 0 & dt & 0 \\ 0 & 0 & 1 & 0 & 0 & dt \\ 0 & 0 & 0 & 1 & 0 & 0 \\ 0 & 0 & 0 & 0 & 1 & 0 \\ 0 & 0 & 0 & 0 & 0 & 1 \end{bmatrix} \tag{5.1.19}$$

$$I_{6\times 6} = \begin{bmatrix} 1 & 0 & 0 & 0 & 0 & 0 \\ 0 & 1 & 0 & 0 & 0 & 0 \\ 0 & 0 & 1 & 0 & 0 & 0 \\ 0 & 0 & 0 & 1 & 0 & 0 \\ 0 & 0 & 0 & 0 & 1 & 0 \\ 0 & 0 & 0 & 0 & 0 & 1 \end{bmatrix} \tag{5.1.20}$$

$$G_{18\times 6} = \begin{bmatrix} \frac{1}{2}d_t^2 & 0 & 0 & 0 & 0 & 0 \\ 0 & \frac{1}{2}d_t^2 & 0 & 0 & 0 & 0 \\ 0 & 0 & \frac{1}{2}d_t^2 & 0 & 0 & 0 \\ dt & 0 & 0 & 0 & 0 & 0 \\ 0 & dt & 0 & 0 & 0 & 0 \\ 0 & 0 & dt & 0 & 0 & 0 \\ 0 & 0 & 0 & \frac{1}{2}d_t^2 & 0 & 0 \\ 0 & 0 & 0 & 0 & \frac{1}{2}d_t^2 & 0 \\ 0 & 0 & 0 & 0 & 0 & \frac{1}{2}d_t^2 \\ 0 & 0 & 0 & dt & 0 & 0 \\ 0 & 0 & 0 & 0 & dt & 0 \\ 0 & 0 & 0 & 0 & 0 & dt \\ \frac{1}{2}d_t^2 & -\frac{1}{2}d_t^2 & 0 & 0 & 0 & 0 \\ 0 & 0 & \frac{1}{2}d_t^2 & -\frac{1}{2}d_t^2 & 0 & 0 \\ 0 & 0 & 0 & 0 & \frac{1}{2}d_t^2 & -\frac{1}{2}d_t^2 \\ dt & -dt & 0 & 0 & 0 & 0 \\ 0 & 0 & dt & -dt & 0 & 0 \\ 0 & 0 & 0 & 0 & dt & -dt \end{bmatrix} \tag{5.1.21}$$

In this section, the positions calculated from Equations 5.1.13-15 (the values of the radii are obtained using Equation 5.1.8 or Equation 5.1.9 when the measurement depth is unavailable; the values of the radii are obtained by Equation 5.1.7 when the measurement depth is available). The position values are then used as the measurement values of the DAD-KF.

<u>Covariance Matrices Q & R Design</u>

To increase the performance of the DAD-KF, we do not calculate the Q & R covariance matrices using the sensor noises since the sensor noises are different to the true error. As shown in Figure 5.1.1, while the two accelerometers are rotating in polar coordinates, there are known distance differences between the three axes and the distance D (0.6 meters in this thesis) between the two accelerometers. These position difference values are used as references.

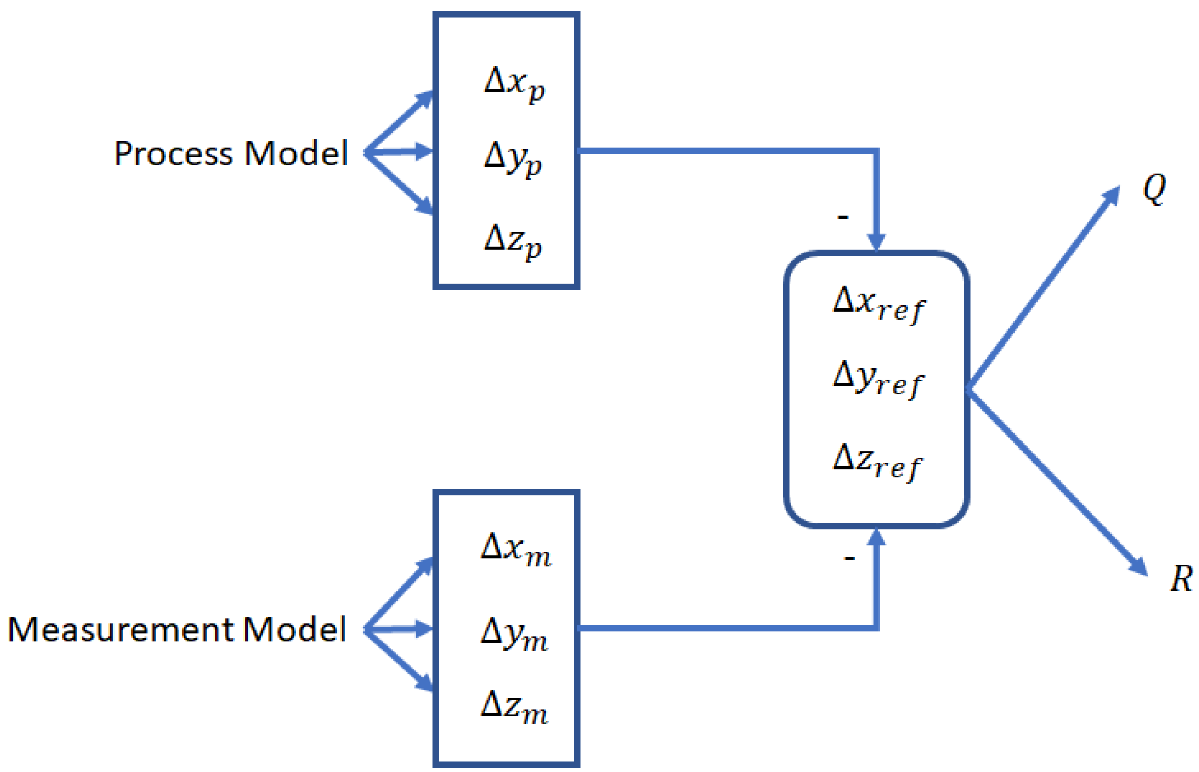

Figure 5.1.2 Covariance matrices Q & R calculation

$$\Delta x_{ref} = D \times sin(\theta_{y,t}) \times cos(\theta_{z,t}) \quad (5.1.22)$$

$$\Delta y_{ref} = D \times sin(\theta_{y,t}) \times sin(\theta_{z,t}) \quad (5.1.23)$$

$$\Delta z_{ref} = D \times cos(\theta_{y,t}) \quad (5.1.24)$$

Also, the position differences between the two accelerometers ($\Delta x_s, \Delta y_s, \Delta z_s$) are compared with the reference values to calculate the errors.

<u>DAD-KF Structure</u>

Time-update prediction: The time-update predicts the state and variance at time $k + 1$ dependent on the information at time t:

$$\begin{cases} \hat{X}_t^- = F\hat{X}_{t-1} + GU_t \\ P_t = F\hat{P}_{t-1}F^T + Q_{t-1} \end{cases} \quad (5.1.25)$$

Measurement Update: The measurement update revises the state and variance using a combination of the predicted state and actual observation.

First, compute the Kalman gain matrix:

$$K_t = P_t H^T (H P_t H^T + R)^{-1} \quad (5.1.26)$$

Then, update the estimate with measurement:

$$\hat{x}_t = \hat{x}_t^- + K_t(y_t - H\hat{x}_t^-) \tag{5.1.27}$$

Finally, update the error covariance:

$$\hat{P}_t = (I - K_t H)P_t \tag{5.1.28}$$

5.1.3 Results and Discussions

The proposed DAD-KF fusion method was tested using a lab-scale test rig. Detailed information about the test rig, the moving path plan, and the sensor setup is in Chapter 4. Dynamic accelerations are easily affected by shock impacts, and the shocks may cause drifts in the acceleration double integral calculation. In addition, a KF cannot filter out shock disturbances without proper a priori information. Therefore, in this section, we combine the known distance *D* between two IMUs (A&B) and the orientation angles to determine distance difference values (Δx_{ref}, $\Delta y_{ref}$and Δz_{ref}) for the two IMUs during rotational movements (Equations 5.1.22-24). After comparing with the known distance difference values (Equations 5.1.22-24), the errors of the process and measurement models of the DAD-KF are used to compute the proper values to design the *Q & R* matrices of the DAD-KF.

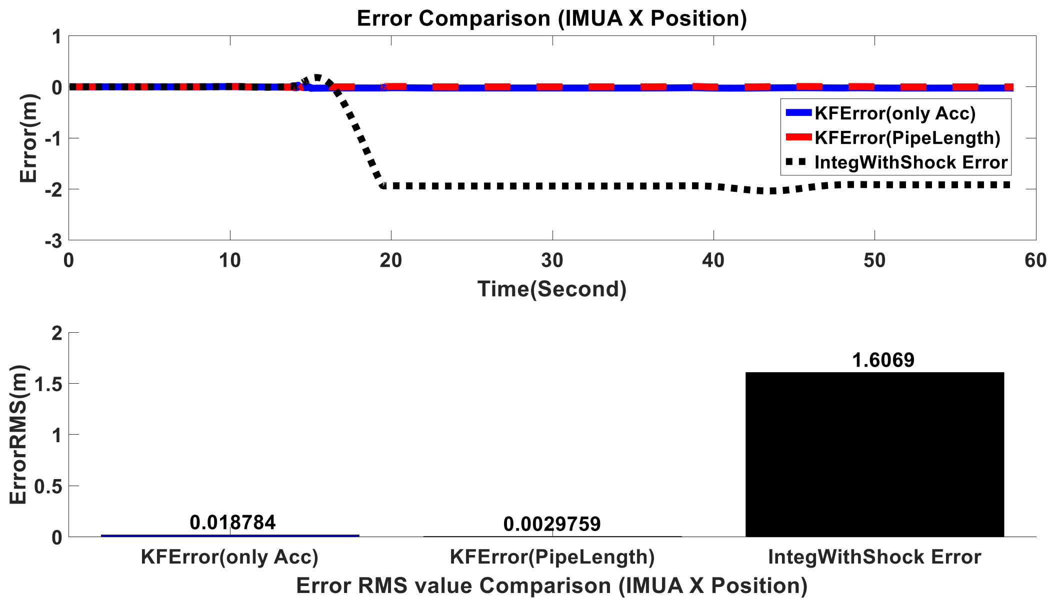

Figure 5.1.3 Error comparison of DAD-KF and acceleration integral calculation (IMU$_A$ X)

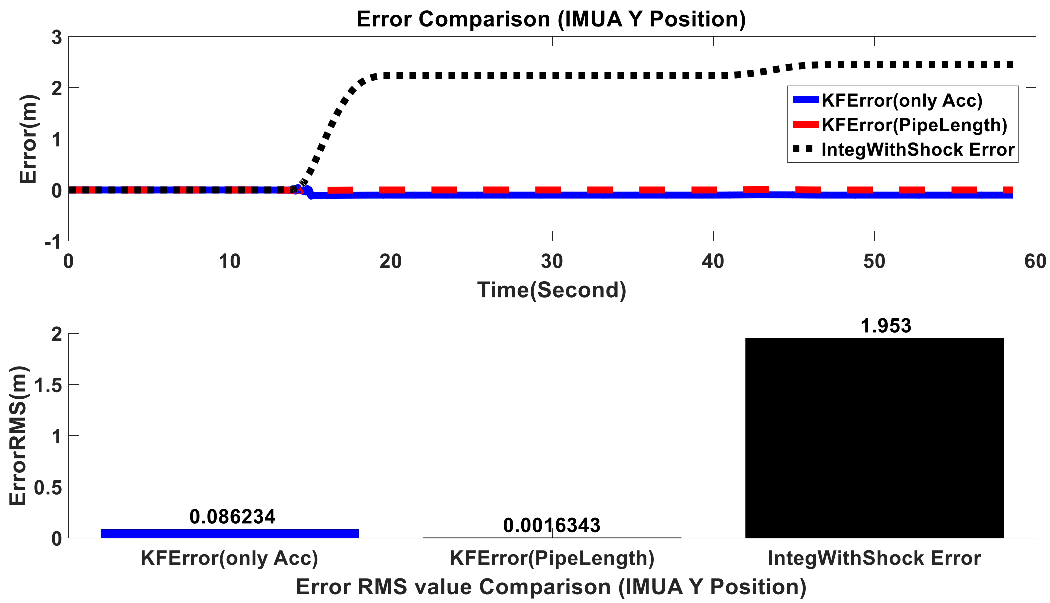

Figure 5.1.4 Error comparison of DAD-KF and acceleration integral calculation (IMU$_A$ Y)

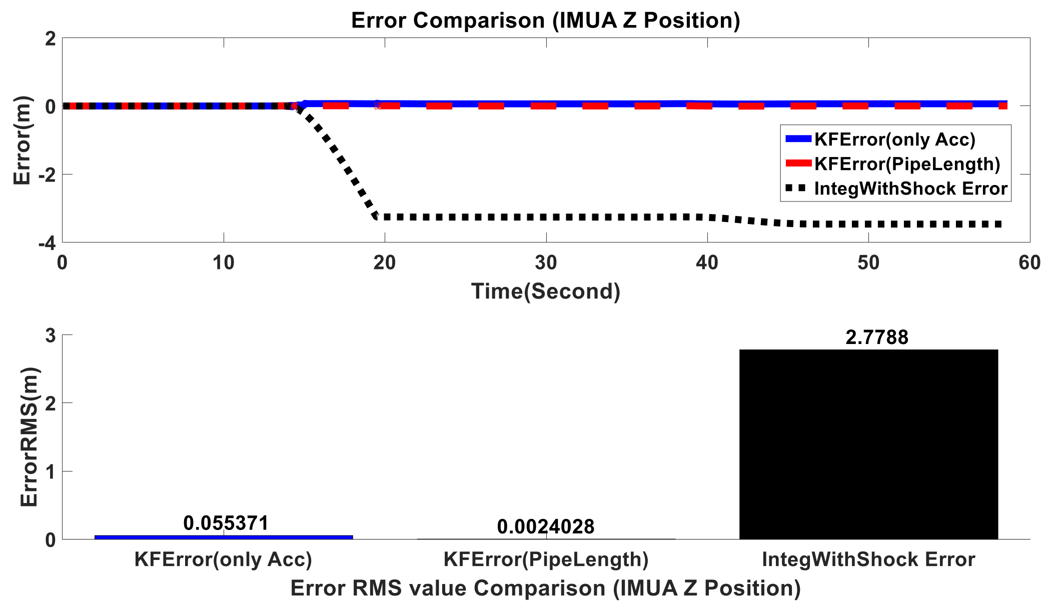

Figure 5.1.5 Error comparison of DAD-KF and acceleration integral calculation (IMU_A Z)

Table 5.1.1 The DAD-KF results: a comparison of IMU_A and IMU_B

	IMU_A(Error)			IMU_B(Error)		
	X(m)	Y(m)	Z(m)	X(m)	Y(m)	Z(m)
KF (Acc only)	0.019	0.086	0.055	0.017	0.086	0.057
KF (Drill string length correction)	0.003	0.0016	0.0024	0.008	0.004	0.007
Acc double integral calculation	1.607	1.953	2.779	15.08	18.113	25.668

To evaluate the performance of the DAD-KF and determine the robustness of the method to shock disturbances, we conducted lab-scale tests with a test rig. Figures 5.1.3-5 and Table 5.1.1 compare the results of DAD-KFs (with and without drill string length correction) and show the pure integral calculations of accelerations. The magnetic and shock robust orientation angles were calculated based on the design introduced in Section 4.1.

The position estimation comparison results of IMU_A and IMU_B on three directions (x, y, and z) show that the shocks caused large drifts (for example, the drift on the z position of IMU_B was up to 25.7 meters) in position estimations when only acceleration double integral calculations were used, as shown in Table 5.1.1. Table 5.1.2 shows the DAD-KF results in first and second case studies (Chapter 4). With the proposed DAD-KF method, the drifts were removed. With the drill string length correction, the error magnitude was reduced to millimeters; without the drill string length correction, the error magnitude was reduced to centimeters. Using the drill string length correction and accurate orientation angles, the DAD-KF showed high robustness to shocks.

Table 5.1.2 The DAD-KF results with drill string length correction: a comparison of IMU_A and IMU_B in the first and second case studies

	IMU_A Error			IMU_B Error		
	X(m)	Y(m)	Z(m)	X(m)	Y(m)	Z(m)
First Case	0.003	0.0016	0.0024	0.008	0.004	0.007
Second Case	0.007	0.0065	0.0024	0.0173	0.0163	0.007

The DAD-KF with drill string length correction reduces the effect of shocks if we assume the orientation angles are accurate. However, when the orientation angles are incorrect (second case study) the magnitude of the errors increased from millimeters to centimeters.

This section proposed a DAD-KF to increase robustness to shock disturbances during position estimation. The known distance *D* between two IMUs is combined with orientation angles (computed in Chapter 4) to provide the difference position references (Δx_{ref}, Δy_{ref} and Δz_{ref}) for the DAD-KF design. The outputs of the process and measurement models of the DAD-KF are compared with the position difference references and the errors are used to compute the Q & R matrices of the DAD-KF then calculate the proper weights. The calculated weights are added to the process and measurement outputs for the final DAD-KF output. Based on the lab-scale tests, the proposed DAD-KF shows high robustness to unknown shocks under the assumed conditions: 1) the acceleration can be corrected to a proper value; 2) the two IMUs' movements are curvilinear and rotate in polar coordinates; 3) two IMUs rotate at one end of the rotation center.

5.2 Two-level Structure (Position, Industry Application)

KFs remove noise and known magnetic disturbances, which allows accurate inclination and azimuth angles to be obtained. In many situations, however, the magnetic disturbances are unknown. Traditional KFs cannot reduce the effect of the unknown magnetic disturbances caused by iron materials or other magnetic resources. It is therefore not feasible to measure the Earth's magnetic field in the presence of iron materials, which include casings, drill strings, and iron ores that are scattered in the subsurface. Although the effect of this magnetic interference can be reduced by utilizing non-magnetic drill collars, this solution could be expensive [Noureldin 2002; Collins 2001; Russel et al., 1985; Zhang et al., 2016].

The orientation angles (inclination and azimuth) and drill string length are inputs of the minimum curvature method (MCM), which is the most common and considered the most accurate model from the defined algorithms used to compute wellbore trajectory. Another popular method is the advanced spline-curve (ASC) model [Abughaban et al., 2016]. The MCM assumes that the arc between survey stations is a constant curvature. However, high resolution surveys show that this assumption is not true because of the sliding/rotating pattern of drilling [Lentsch et al., 2012].

This assumption miscalculates the actual true vertical depth (TVD) and underestimates of torque and drag (T&D) because MCM tends to create an artificially low tortuosity by mathematically smoothing the well path between survey stations. To overcome these limitations, Abughaban et al. developed the ASC model to provide realistic results and accurately calculate the spatial course of a well path [Abughaban et al., 2016].

These methods are sufficiently accurate [Amorin et al., 2010; Sampaio 2007]; however, the accuracy of both MCM and ASC depends on their inputs: orientation angles and measured depth. The inclination angles and TVD calculated from accelerometers and measured depth calculated from drill string length have relatively minimal errors because of the stable gravity field and known drill string length measurements. However, the position estimations of North and East depends on the performance of magnetometers and a low magnetic disturbance environment.

5.2.1 Two-level Structure Filter For Industry Application

For well path estimation, it is necessary to consider the travel distance in x(easting), y(northing), and z(true vertical depth) axes. The traditional industry standard method to calculate wellbore trajectory is the MCM method MCM combined with KFs. For this kind of KF design, the MCM calculation value is used as measurement model information, and the double integral calculation of acceleration is used as process model information. [ElGizawy et al., 2010; Zhang et al., 2016]. Although MCM is a successful method, the accuracy can be improved using ASC because MCM is limited due to its assumption that the arc between survey stations is smooth [Abughaban et al., 2016]. However, the accuracy of the wellbore trajectory estimation depends on a complex well path model and accelerometer and magnetometer signals having minimal errors, which is difficult to obtain during drilling processes. Finally, both MCM and ASC are affected by magnetic interferences, which can cause errors in azimuth angle measurements from magnetometers.

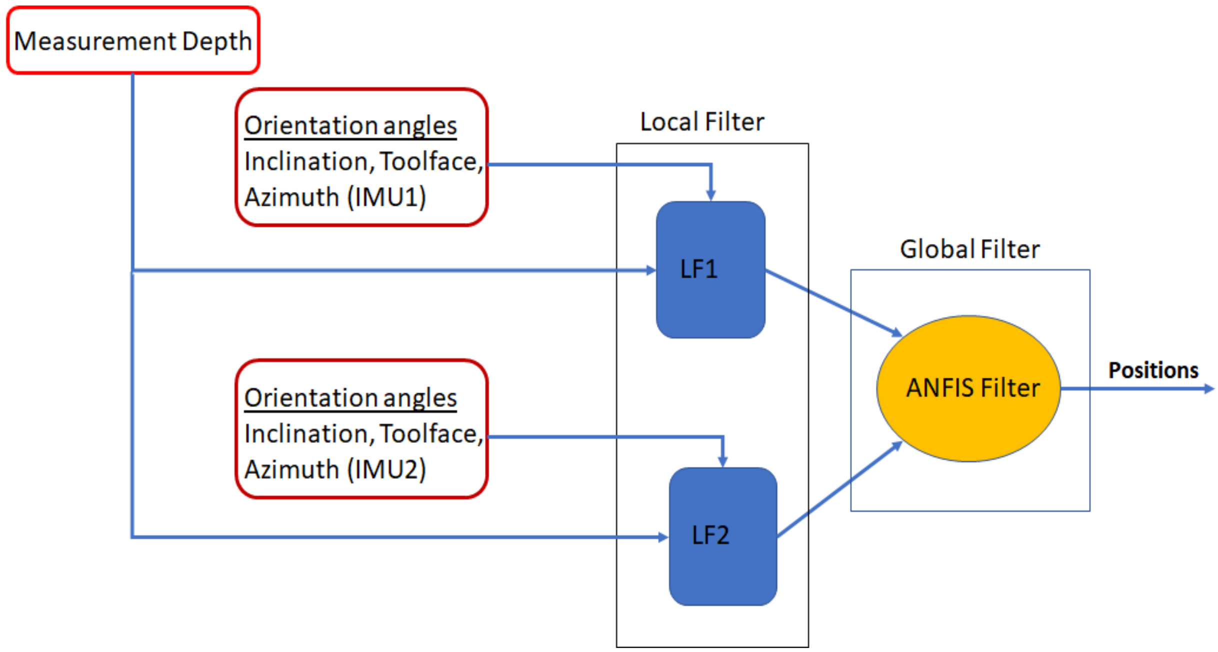

Figure 5.2.1 The extended filter structure for industry application

A two-level filter is extended for well path position estimation [Liu et al., 2018]. In the first level (local), ANFIS is used to filter out the position errors caused by the sensor error; then, the outputs of the local filters are entered into the global ANFIS filter to reduce the effect of magnetic interferences.

5.2.2 Local Filter (Splines and ANFIS)

Spline Method

The position of a wellpath trajectory can be calculated from an approximate spline [Abughaban et al., 2016]:

$$\begin{bmatrix} Pos_{E(i)} \\ Pos_{N(i)} \\ Pos_{TVD(i)} \end{bmatrix} = \sum_{i=1}^{n} \begin{bmatrix} l_i A_{E(i)} + \frac{l_i^2}{2} B_{E(i)} + \frac{l_i^3}{3} C_{E(i)} + \frac{l_i^4}{4} D_{E(i)} \\ l_i A_{N(i)} + \frac{l_i^2}{2} B_{N(i)} + \frac{l_i^3}{3} C_{N(i)} + \frac{l_i^4}{4} D_{N(i)} \\ l_i A_{TVD(i)} + \frac{l_i^2}{2} B_{TVD(i)} + \frac{l_i^3}{3} C_{TVD(i)} + \frac{l_i^4}{4} D_{TVD(i)} \end{bmatrix} \tag{5.2.1}$$

Here,

$$l_i = MD_{i+1} - MD_i \tag{5.2.2}$$

where MD_i are values of measurement depth.

$$\begin{bmatrix} A_{E(i)} \\ A_{N(i)} \\ A_{TVD(i)} \end{bmatrix} = \begin{bmatrix} sin\theta_{inc(i)} sin\theta_{azi(i)} \\ sin\theta_{inc(i)} cos\theta_{azi(i)} \\ cos\theta_{inc(i)} \end{bmatrix} \tag{5.2.3}$$

$$\begin{bmatrix} B_{E(i)} \\ B_{N(i)} \\ B_{TVD(i)} \end{bmatrix} = \begin{bmatrix} \frac{A_{E(i+1)} - A_{E(i)}}{l_i} - \frac{l_i}{6} z_{(i+1)} - \frac{l_i}{3} z_{(i)} \\ \frac{A_{N(i+1)} - A_{N(i)}}{l_i} - \frac{l_i}{6} z_{(i+1)} - \frac{l_i}{3} z_{(i)} \\ \frac{A_{TVD(i+1)} - A_{TVD(i)}}{l_i} - \frac{l_i}{6} z_{(i+1)} - \frac{l_i}{3} z_{(i)} \end{bmatrix} \tag{5.2.4}$$

$$\begin{bmatrix} C_{E(i)} \\ C_{N(i)} \\ C_{TVD(i)} \end{bmatrix} = \begin{bmatrix} \frac{z_{(i)}}{2} \\ \frac{z_{(i)}}{2} \\ \frac{z_{(i)}}{2} \end{bmatrix} \tag{5.2.5}$$

$$\begin{bmatrix} D_{E(i)} \\ D_{N(i)} \\ D_{TVD(i)} \end{bmatrix} = \begin{bmatrix} \frac{z_{(i+1)}-z_{(i)}}{6l_i} \\ \frac{z_{(i+1)}-z_{(i)}}{6l_i} \\ \frac{z_{(i+1)}-z_{(i)}}{6l_i} \end{bmatrix} \tag{5.2.6}$$

The details of how to calculate $z_{(i)}$ are shown in [Abughaban et al., 2016].

<u>ANFIS</u>

Traditional MCM and spline methods are limitated in terms of the accuracy of well path estimations because of sensor measurement uncertainty and the methods themselves: both methods assume the arc between survey stations is smooth, and therefore, nonlinear features are not considered. Here, the ANFIS method was employed to build a model of orientation angles, measurement depth and the well path positions.

With proper wellbore survey data, the ANFIS can be trained as a 3D model with inclination and azimuth. If survey data is not available, the inclination cannot be modeled properly; however, a horizontal path model can be built using ANFIS with the assistance of GPS data training. Since GPS cannot provide subsurface position information, it is limited in terms of building an inclination model.

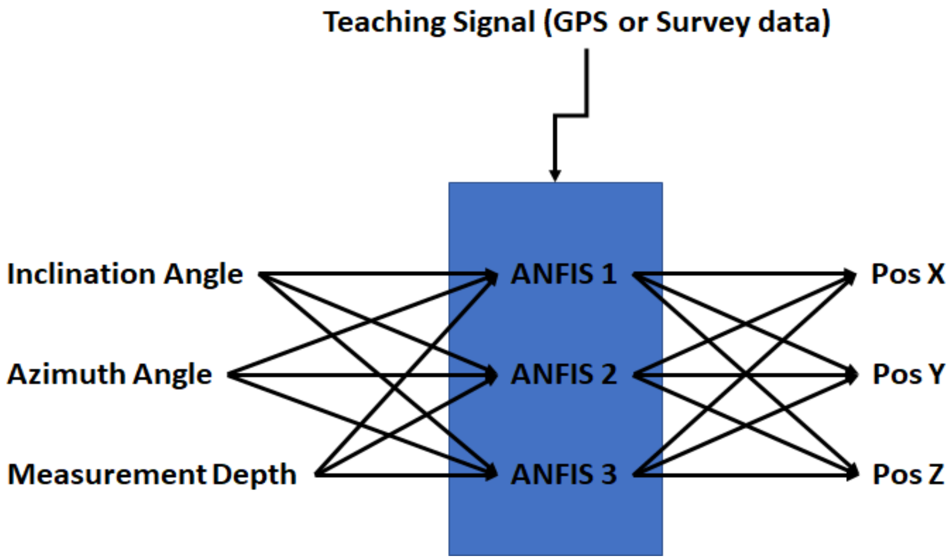

Figure 5.2.2 ANFIS design for position estimation

For accuracy of the horizontal plane, ANFIS can be used to build an input/output relationship between orientation angles, measured depth, and positions using GPS data as a teaching signal. With the GPS correction, the position uncertainties caused by sensor errors and the calculation method itself are filtered out. The ANFIS model design of a local filter is shown in Figure 5.2.2. As shown in the figure, if the teaching signal is GPS data, the ANFIS represents a 2D position model of the horizontal plane; if the teaching signal is survey data, the ANFIS represents a 3D position model that includes inclination. ANFIS can model a proper relationship between inputs and output positions, but the azimuth angle is distorted due to magnetic disturbances. This error leads both the spline and local ANFIS methods to output wrong values. A global ANFIS filter is proposed to reduce the effect of magnetic disturbances in this situation.

5.2.3 Global Filter (ANFIS)

Input Design of Global ANFIS

Two IMUs are mounted on a rigid body a known distance apart to reduce the influence of magnetic disturbances. In this scenario, we assume a single source of magnetic interference, such that one IMU is perturbed while the other is not due to the longer distance from the disturbance. The idea is to weigh the information obtained from the two IMUs to estimate the orientation angle. A weighted average of $LF1$ and $LF2$ can provide an appropriate estimation despite magnetic disturbances. The inputs of the artificial intelligence (AI) filter system should be set up appropriately to determine the weights of each IMU. If the output values of $LF1$ and $LF2$ are similar, then either both IMUs are reliable under clean conditions (without interferences) or they experience the same level of interference. In this situation, it is difficult to say which of these cases is true, so both are considered untrustworthy. In this situation, the weights w_1 and w_2 should be equal.

If there is a large difference between the two values, that means magnetic disturbances are affecting one sensor greatly. In this case, new variables are needed as additional inputs to decide the weights of the orientation outputs of both local filters. In this research, deviation degree of total geomagnetic field strength (DDTGFS) and deviation degree of geomagnetic field horizontal intensity (DDGFHI) are used to calculate these new weights.

Without magnetic disturbances, the total magnetic field strength measured by the magnetometer (B_{sx}, B_{sy}, B_{sz}) should be $B\left(B_x, B_y, B_z\right)$. The deviation value depends on the sensor's quality. Magnetic disturbances draw the sensor value away from the real magnetic field strength. The deviations caused by the magnetic disturbances are defined as follows:

$$DDTGFS = \left|\sqrt{B_{sx}^2 + B_{sy}^2 + B_{sz}^2} - B\right| \tag{5.2.7}$$

$$DDGFHI = \left|\sqrt{B_{sx}^2 + B_{sy}^2} - B_h\right| \tag{5.2.8}$$

where the values of B (total magnetic field strength) and B_h (horizontal magnetic field strength) are different based on their physical location. Local values can be obtained from the database of the international geomagnetic reference field; according to this database, the total magnetic field strength for Calgary, Alberta, Canada is $B = 56125\ nT$, and that the horizontal magnetic field strength is $16115\ nT$.When the DDTGFS of IMU_A is bigger than that of IMU_B, IMU_A is more affected than IMU_B. IMU_B should be trusted more, and the weight assigned to IMU_A should be small. When the DDTGFS values of both sensors are similar, then DDGFHI is used. We assume that one sensor is exposed to magnetic disturbances and the other is not; therefore, the differences between the two sensors are used as input values.

ANFIS Structure

ANFIS is an algorithm that combines neural network and fuzzy logic approaches to obtain more accurate results. In this section, there are three input values and three MFs that serve as ANFIS inputs. Bell-shaped membership functions are chosen with a maximum equal to one and a minimum equal to zero. The fuzzy logic toolbox in MATLAB was used for training and evaluating the fuzzy inference system. As shown in Figure 5.2.3, two azimuth angles calculated from IMU measurements are compared with a reference azimuth angle to obtain the teaching weights for training the ANFIS fusion model. Then, the ANFIS fusion model provides proper weights of these two IMUs based on the magnetic disturbance magnitudes. After the magnetic disturbances are removed, the final azimuth angle is obtained and then input into the ANFIS position model together with inclination angle and measurement depth to output the 3D positions.

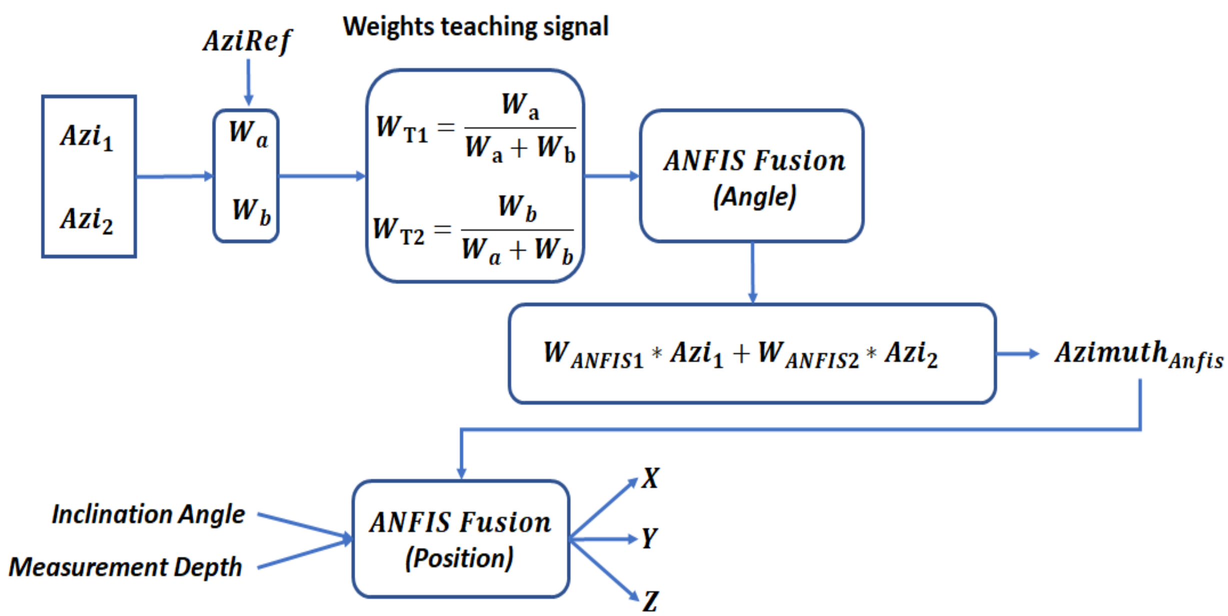

Figure 5.2.3 ANFIS filter for position estimation

5.2.4 Experimental Results (GPS Comparison)

To evaluate the performance of the proposed local filter, we designed and implemented a horizontal field test, at the University of Calgary and compared the results with GPS reference data. The sensor was first moved on the ground, at the same time the measurement data were recorded to calculate the orientations. Then, GPS data was used as a teaching signal to train the ANFIS models. The moving area was selected on an almost flat ground with small inclinations. As shown in Figure 5.2.4, two IMU sensors were put on a cart and moved along a path indicated by the red line shown on the map in Figure 5.2.5. Sixty-five stops were chosen at one meter intervals to simulate the survey stations in horizontal drilling processes. A roll measure was used to provide the measured depth, and the orientation angles (inclination and azimuth) were obtained from the IMUs. First, the results of one IMU were compared with a GPS reference that was obtained using a Trimble R10 GNSS receiver with an accuracy of 8 mm for horizontal and 15 mm for vertical position measurements (Trimble 2012). Figure 5.2.6 shows the azimuth and inclination angles calculated from the two calibrated IMUs. Differences in the measurements were due to manufacturing and could not be avoided even with careful calibration, and these differences caused errors in the spline calculations as shown in Figures 5.2.6-7.

Figure 5.2.4 Horizontal field test setup

To evaluate the global filter, we manually added three magnetic disturbances that affected IMU_A, and these disturbances caused a deviation in the azimuth angles. This deviation is shown in Figure 5.2.8 where the blue dashed line is the disturbed azimuth angle, and the red dashed line is the azimuth angle measured by IMU_B without magnetic disturbances. The three magnetic disturbances were put at station 10, 30, and 50 (one at each station). Also, as shown in Figure 5.2.8, the magnetic disturbances caused large deviations in the azimuth angles. Further, these azimuth angle errors caused horizontal position errors when the spline method was used as shown in Figure 5.2.9. The error in the vertical position remained the same since the azimuth angle was not used in the vertical position calculation in the spline method.

Figure 5.2.5 Above ground test path

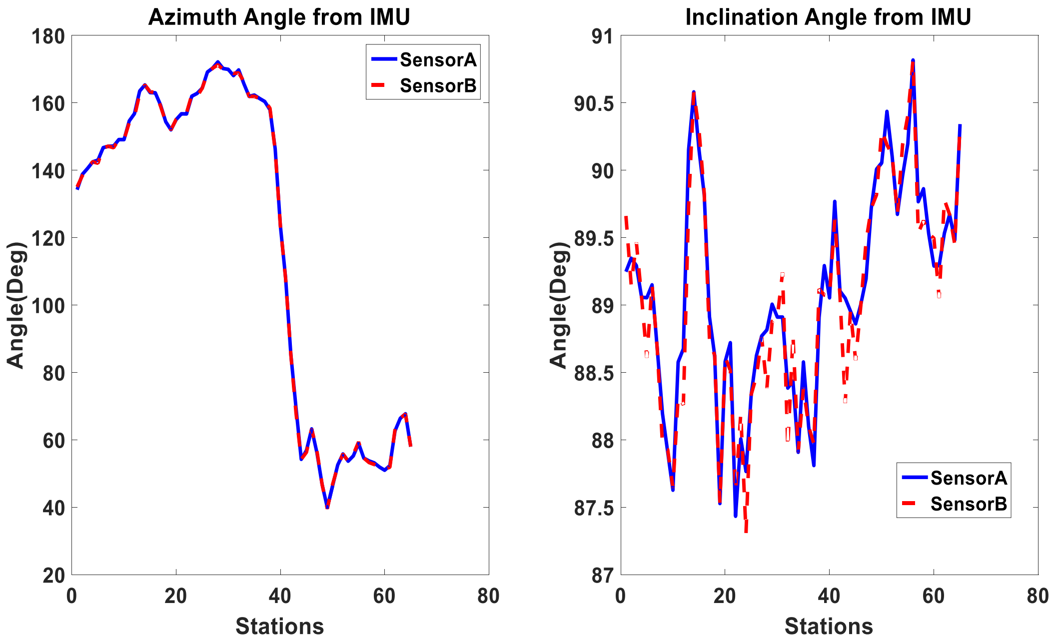

Figure 5.2.6 Azimuth and inclination IMU measurement difference

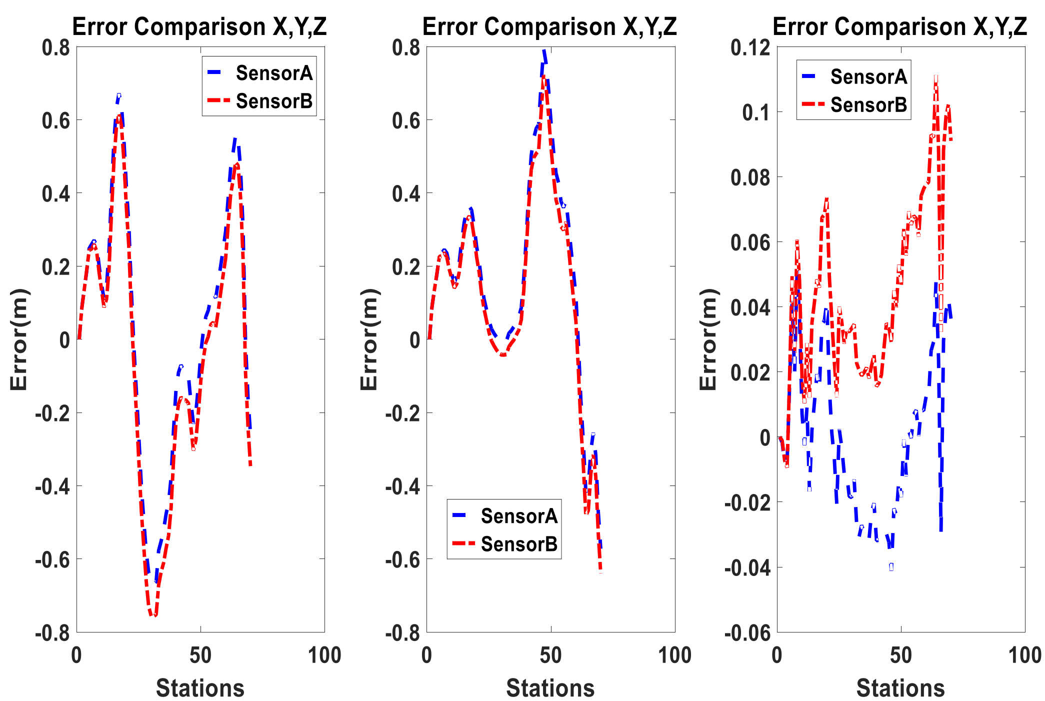

Figure 5.2.7 Spline error difference caused by IMU uncertainty

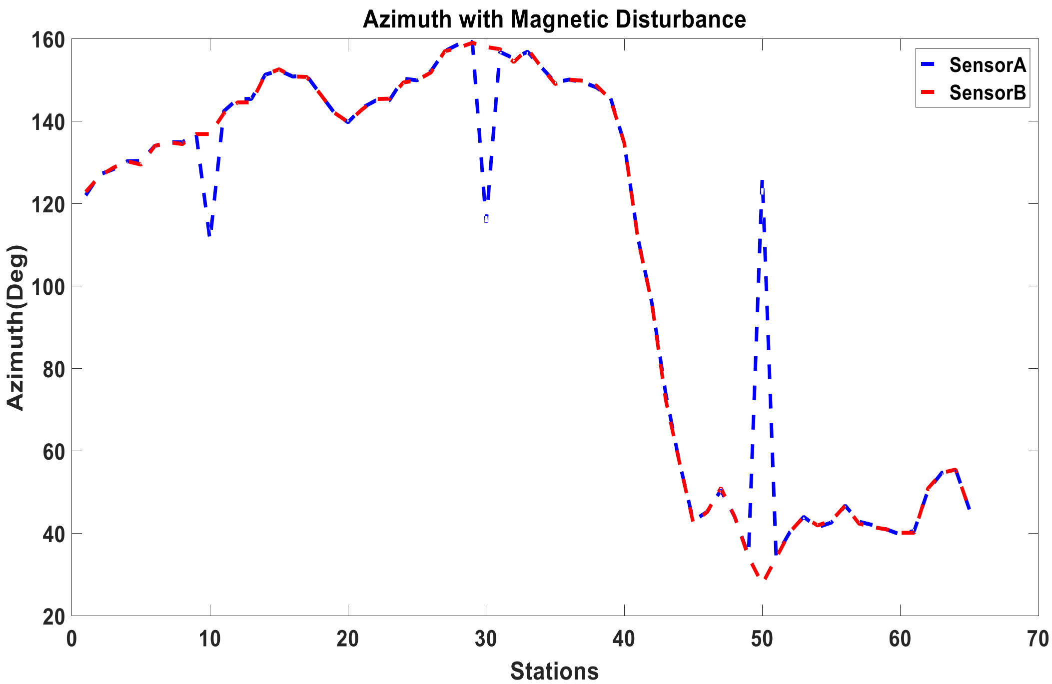

Figure 5.2.8 Azimuth angle with magnetic disturbance

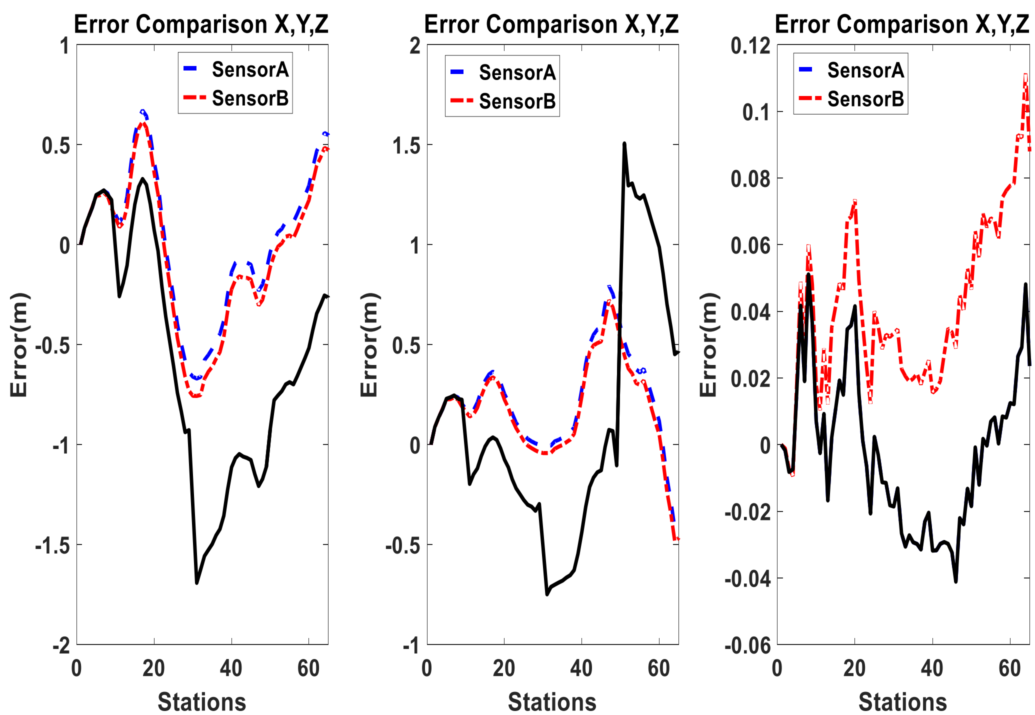

Figure 5.2.9 Position error caused by azimuth angle drift

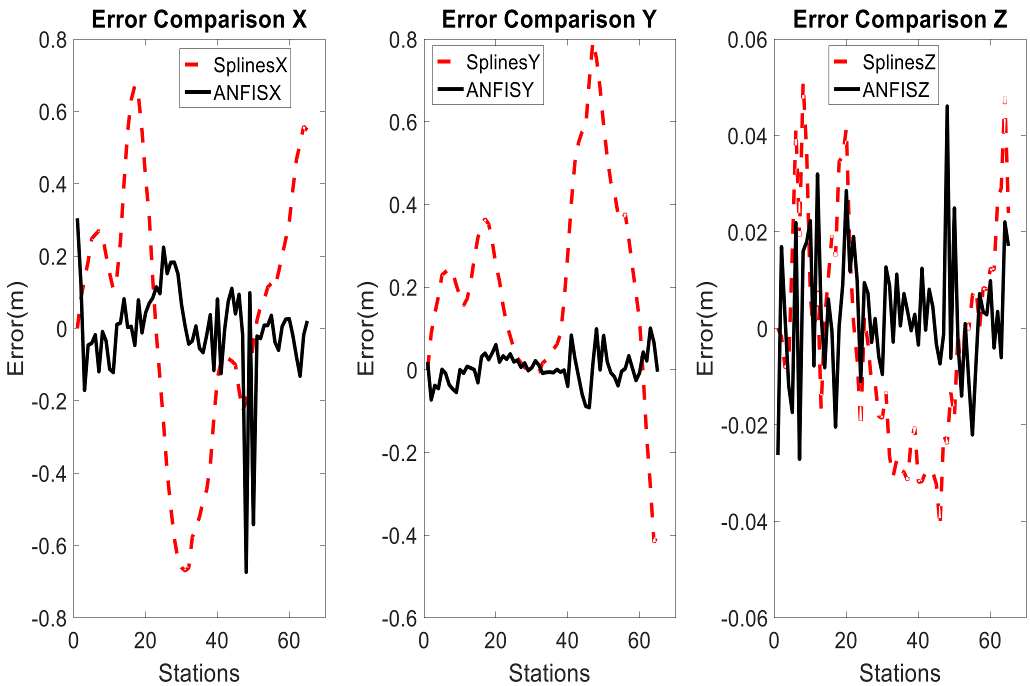

Figure 5.2.10 ANFIS vs. spline method

The performance of the proposed ANFIS filter in an environment with magnetic disturbances is shown in Figure 5.2.10. The red dashed line is the error of the spline method without the azimuth angle deviation. The ANFIS shows high robustness to magnetic disturbances and performs better than the spline method without magnetic disturbances.

High accuracy wellbore positioning is important to the directional drilling process. Current methods used in the industry include well path calculations using the MCM and splines. These methods are sufficiently accurate for survey activities; however, the accuracy of these methods is dependent on the performance of measurement sensors. In addition, the current horizontal position estimation is significantly affected by magnetic disturbances. A two-level structure ANFIS filter design was proposed to address the drawbacks in the current wellbore trajectory estimation methods.

- The ANFIS filter has a two-level structure (local and global). The local filters employ ANFIS to model the wellbore trajectory and, to remove the position errors caused by poor measurement sensor performance. In this local level design, magnetic disturbances are not considered.

- The local ANFIS needs teaching signals to train it. The teaching signals can be obtained from survey data, or for horizontal drilling path estimations, they can be obtained from GPS data. There is no reference to correct underground horizontal estimations and current subsurface position estimation accuracy only depends on the performance of magnetometers. If it is assumed that magnetometers experience the same situation in above ground and underground environments, GPS and ANFIS can be used to correct the magnetometer errors in underground environments given a similar route above ground. The key factor of this design is the accuracy of ANFIS estimations. A GPS comparison test conducted at the University of Calgary, with GPS correction, showed that the proposed local ANFIS performed well and was sufficiently accurate.

- The outputs of two local filters were input into a global ANFIS filter, which adjusted the proper weights of the two local filters based on the strength of the magnetic disturbances. This design assumed that both sensors were not disturbed simultaneously; therefore, depending on the deviation strength of the two magnetometers to magnetic disturbances, the global ANFIS makes proper adjustments.

- From the evaluation results of the GPS test data, the proposed design showed a marked reduction in estimation errors and increased robustness to sensor noise and disturbances.

5.3 Summary

This chapter introduced a newly designed KF to estimate positions with high robustness to shock impacts. The *Q & R* matrices of traditional KFs require a priori error information, which is difficult to obtain in real applications. Consequently, the known distance *D* between two IMUs was combined with orientation angles and then used as a reference for *Q & R* computing to allow the KF to update the *Q & R* matrices so that the matrices could be computed without a priori error information. The lab-scale tests showed this newly designed KF had high robustness to shock disturbances.

In addition, a real drilling industry process was simulated at the University of Calgary. Two-level structure position fusion (global: ANFIS; local: ANFIS or industry favored spline position estimation method) was introduced to reduce the effect of magnetic disturbances and sensor uncertainties. The results of the two-level structure position estimation method were evaluated using GPS data as a reference, and they showed what this method performed better.

CHAPTER 6. CONCLUSIONS

Improving the accuracy of sensors for underground orientation is crucial. Subsurface industry activities, such as monitoring a reservoir's leakage or directional drilling, need to be oriented correctly (inclination and azimuth) and have accurate locations (north, east, and vertical). Magnetic disturbances need to be identified and suppressed to achieve higher orientation accuracy during the sensing process. GPS is typically used for this purpose, but signals are difficult to obtain beneath the surface. Therefore, high precision in position sensing with IMUs must be achieved without GPS.

Different methodologies for improving the accuracy of underground orientation and displacement measuring are proposed in this research. The orientation angle fusion methodologies are divided into two main types: SLF and SL-KF.

SLF: to reduce the effect of unknown magnetic and shock disturbances, we use ANFIS to build error models of each IMU sensor (magnetometer, gyroscope, and accelerometer) under working conditions with magnetic and shock disturbances; based on these error models, the proper weights are calculated and added to the IMU sensors for the final output.

SL-KF: SLF designs the process and measurement inputs of a KF, and ANFIS is used to build error models for covariance matrices to increase the ability of KF to recognize errors since the performance of a KF depends on the proper design of covariance matrices. Finally, the orientation angles computed from the above-mentioned fusion methods are used for position fusion.

The orientation angles are robust; however, the position estimation calculated using double integral calculations of dynamic accelerations are still affected by shocks. The dual acceleration difference method is proposed to build reference values of covariance matrices (Q & R) of a position fusion KF, called DAD-KF. Based on the reference values, the proper covariance matrices are computed and used to recognize shock interferences. The adapted covariance matrices increase the shock robustness of the DAD-KF. Finally, a two-level positioning fusion structure that uses ANFIS is also proposed and evaluated using a simulated drilling process. The local-level ANFIS models the wellbore path using orientation angles (azimuth and inclination) and measurement depth as inputs. Then, the global-level ANFIS removes the unknown magnetic disturbances.

This chapter provides a summary of the presented works and the novel contributions of this research. The limitations and assumptions associated with the proposed methods are also discussed. Future works are discussed in the last section of this chapter.

6.1 Expected Scientific Contributions

The novel contributions of this research fall into three categories. First, a special IMU configuration is proposed. Then, the supervised learning filter (SLF) is proposed to increase a sensor's orientation angle fusion robustness to unknown magnetic and shock disturbances. Finally, a dual acceleration difference method is proposed to compute the reference values for covariance matrices of a position fusion KF (DAD-KF).

Subsurface Sensing System Configuration

This configuration consists of two redundant IMUs that are located on a rigid body separated by a known distance D; the distance D reduces the negative influence of magnetic disturbances. This configuration allows for the identification of unknown magnetic disturbances assuming that the two IMUs are not exposed to magnetic disturbances at the same time (because of *D*, when one IMU is close to a magnetic disturbance, the other IMU is far from the magnetic disturbance). Also, IMU accelerometer measurements can be corrected using the dual acceleration difference method and *D* and the orientation angles in environments with insufficient GPS data, such as underground. The two redundant accelerometers have a difference value *D* as the sensor system moves (assuming the movement has a curvilinear trajectory with polar coordinates). The different position values on the *x*, *y*, and *z* axes can be calculated using *D* multiplied by orientation angles (azimuth and inclination). The proposed design uses these different positions to correct the positions calculated from double integral calculation of accelerometers' measurements. The corrections are reliable because *D* is a constant value and the orientation angles are accurate.

Supervised Learning Filter for Orientation Design

The second contribution is the creation of an identification technique that detects unknown magnetic and shock disturbances. This technique predicts the deviation strength of the magnetic and shock interferences from the error models built by ANFIS. The measurements from all sensors (magnetometer, gyroscope, and accelerometer) are compared to calculate the relative errors that are then used as the inputs of the ANFIS. After a training process that uses teaching signals, the proper error models are built and used to calculate the weights for the final angle fusion outputs. The error can be reduced to smaller than 0.26 degrees through RMS value evaluation.

Also, the supervised learning method can be used to enhance the performance of an orientation fusion KF named SL-KF. With a priori noise information and the proper covariance matrices, KFs work properly. However, measuring noises properly is a problem of the KF design, especially in the presence of magnetic and shock disturbances with random strengths. The ANFIS error models can identify unknown magnetic and shock disturbances. Therefore, ANFIS is used to compute the errors to design the covariance matrices of the SL-KF. For the first step, SLF models the errors of the process and the measurement inputs of the KF. Then, these modeled errors are put into the covariance matrices to compute the proper weight of the final SL-KF output. The robustness of the SL-KF increased approximately 56% compared with the SLF approach in the case where all sensors were negatively affected.

Dual Acceleration Difference Method

Another research contribution is recognizing the usefulness of acceleration information in obtaining accurate displacement measurements. Almost all traditional methods rely on external correction aids such as GPS. These methods limit the application fields, especially for subsurface environments.

This thesis proposes how to overcome this limitation using alternate methods. Instead of using real external position measurement signals, such as those obtained from GPS, it uses correction signals designed based on the dual acceleration difference method to correct the velocities and positions. The distance D between the two accelerometers and the rotation information are used for real correction signal computation.

A polar coordinates system is introduced to build a movement model that reduces the influence of centrifugal accelerations, which do not contribute to the displacement magnitude calculation. The experimental results show the effectiveness of the proposed method (the position errors are reduced from meters to millimeters).

6.2 Limitations and Assumptions

A subsurface sensor system with original fusion methodology is introduced in this thesis. The sensor fusion system is designed to increase robustness to unknown magnetic and shock disturbances during orientation estimation and to obtain accurate positions using only acceleration information.

The SLF is proposed to improve the robustness to magnetic and shock disturbances. All angles obtained from magnetometers, gyroscopes, and accelerometers are compared, and their relative errors are put into the ANFIS to build error models. The final weight of each sensor is calculated according to the outputs of each error model. The proposed method performs sufficiently under the assumed conditions: 1) the reference angle can be obtained, 2) only one magnetometer is affected by magnetic disturbances at the same time, 3) two IMUs rotate at one end of the rotation center, and 4) this method is only applied under similar conditions in a training environment. The angle errors caused by unknown magnetic and shock disturbances are corrected by the proposed fusion method. However, the errors cannot be satisfactorily reduced in the scenario where all sensors are inaccurate. Also, the SLF uses two accelerometer difference values to increase the redundant rotation information to be a backup for a gyroscope in the cases where a gyroscope is absent. However, direct applications of this setup (dual accelerometer difference) cause large errors because of the accelerometer noise. This setup has low robustness to shocks as well.

A KF combined with the SLF is proposed to increase the performance in the case where all sensors are inaccurate. SLFs are used as local filters to determine the rotational angular speeds and angles to be used as inputs for the global filter (SL-KF). All angles and angular speeds from magnetometers, gyroscopes, and accelerometers are compared, and their relative errors are put into

ANFIS to build the error models of the covariance matrices of the SL-KF. Analyzing the results shows the SL-KF's robustness increases 56% compared with the SLF. However, SL-KF has the limitations of the SLF and more complex calculations than the SLF.

This thesis proposes a position fusion named DAD-KF based on the dual acceleration difference method designed for position correction instead of using a GPS correction signal to reduce the errors caused by shock to the accelerometers. The distance *D* between the two redundant IMUs combined with the rotation information obtained from the SLF is used to design a new real correction signal. The application of this redundant data correction method requires special assumptions: 1) the rotation center of both IMUs must be at one end of a straight line, and 2) the movement is along a curvilinear path in polar coordinates. It is only in this situation that the dual acceleration difference method can provide accurate correction information.

6.3 Future Works

This study develops different, effective methods for subsurface orientation angles and position fusion that is robust to shock and magnetic disturbances. However, the accuracy of the fusion results can be improved if the limitations and assumptions associated with each method are addressed. Further research can be divided into two main categories: (a) using geomagnetic information as a reference to reduce magnetic disturbances and (b) developing the SLF to semi-supervised learning.

<u>Geomagnetic Reference Design</u>

Sensor errors were used in this study, which means that there were no trustworthy references to judge the reliability of each sensor. Therefore, the SLF was employed to decide the reliability. However, the SLF is limited in that it requires teaching signals for training, but these teaching signals are difficult to obtain during real field applications, especially in subsurface sensing. Geomagnetic field information may be a good candidate to address this limitation.

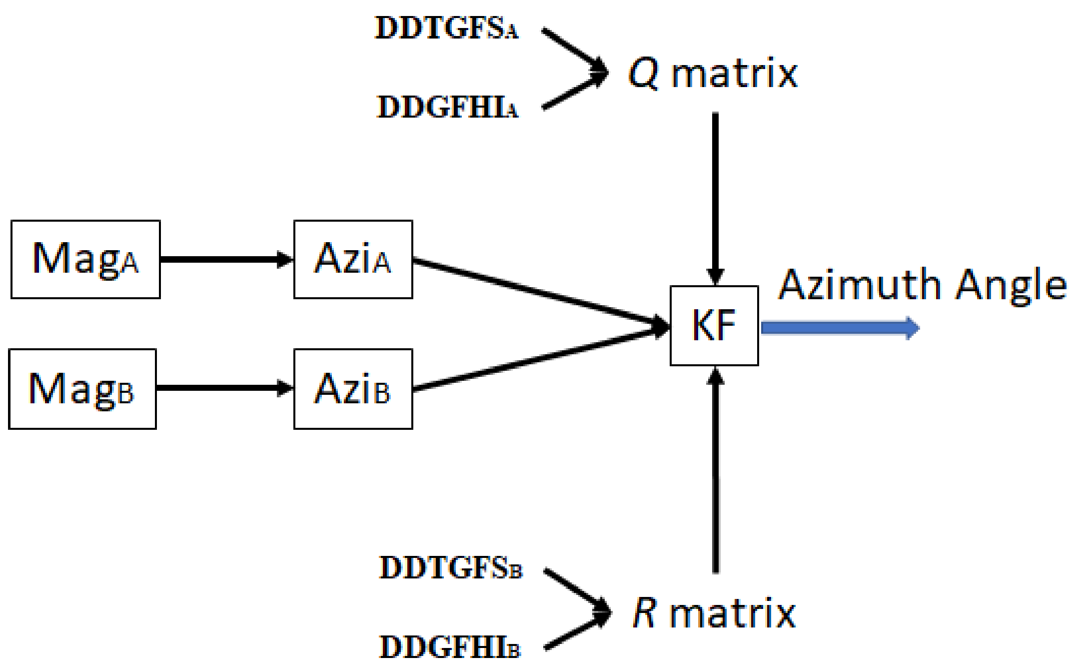

Figure 6.1.1 Reference angle computing based on a geomagnetic reference

As shown in Liu et al. [2018], two redundant IMUs (IMU_A and IMU_B) are mounted on a rigid body with a known distance, and the weight information obtained from these sensors is used to estimate orientation angles. A weighted average of azimuth angles obtained from IMU_A and IMU_B can provide an appropriate estimation despite magnetic disturbances. If the output values of IMU_A and IMU_B are very close, both IMUs are unaffected by magnetic interferences or they experience the same level of interference. In this situation, it is difficult to say which of these cases is true, so both are considered untrustworthy.

If there is a large difference between the two values of IMUs, magnetic disturbances affect one sensor greater than the other sensor. In this case, new variables are necessary. Two values, deviation degree of total geomagnetic field strength (DDTGFS) and deviation degree of geomagnetic field horizontal intensity (DDGFHI) are proposed. The values of DDTGFS and DDGFHI can be calculated using Equations 5.2.7 and 5.2.8. These two kinds of values can be used to compute the covariance matrices for a KF.

The azimuth angle, calculated from the KF (Figure 6.1.1), is used as a teaching signal for the proposed SLF and SL-KF approaches.

Semi-Supervised Learning Design

This thesis proposes using one sensor, for example a magnetometer, as a reference to obtain errors by comparing this reference sensor with other different sensors. Then, these error groups are labeled as different groups, for example small error groups or big error groups, using a supervised learning method (ANFIS was used to build error models in this thesis). Neural networks (NN) are also good candidates to build the error model of the proposed SLF method. The basic function of the NN is to build a model using input/output data sets [Farias et al., 2018]. Another well-known supervised learning method is called random forests (RF). RF is a proven method for regression and classification [Cutler 2010]; therefore, RF can also build the error model of the proposed SLF approach. The thesis shows that the SLF performs well with a training process. However, training data is insufficient in real applications, such as subsurface sensing.

Output values are not necessary for an unsupervised learning method to label group data. As introduced in Ghahramani [2004], the unsupervised learning module receives input i_1, i_2,…,

i_n, but no teaching signals are obtained. Therefore, the main function of the unsupervised learning method is clustering; however, it is difficult to do the labelling [Lyons et al., 2018].

A semi-supervised learning method has been proposed by researchers to combine the benefits of both supervised and unsupervised learning [Chapelle 2006]. In this method, the labeled data (training data) and unlabeled data is mixed to build a new model. The advantages of semi-supervised learning include reducing the training data amount and improving the model robustness because of a more precise decision boundary [Jain 2017]. Therefore, when the training data are not sufficient for training the SLF, the following process may address this problem. First, the SLF is trained using lab-scale test data or partial field data to build the initial error models of magnetic and shock disturbances; then, the new unlabeled data is labeled by semi-supervised methods, such as K-means, to update the new error models.

REFERENCES

Abdulrahim, K., Moore, T., Hide C., Hill C., 2014, "Understanding the Performance of Zero Velocity Updates in MEMS-based Pedestrian Navigation", International Journal of Advancements in Technology, Vol.5, No.2, pp.53-60.

Abughaban, M. F., Bialecki, B., Eustes, A.W., Wardt, J.P.de, Mullin, S., (2016). Advanced Trajectory Computational Model Improves Calculated Borehole Positioning, Tortuosity and Rugosity. IADC/SPE Drilling Conference and Exhibition, Texas, USA.

Abbott, J.J., Ergeneman, O., Kummer, M.P., Hirt, A.M., Nelson, B.J., 2007, "Modeling Magnetic Torque and Force for Controlled Manipulation of Soft-Magnetic Bodies", IEEE Transactions on Robotics, Vol.23, No.6, pp.1247-1252.

Akhlaghi, S., Huang, Z., 2017, "Adaptive Adjustment of Noise Covariance in Kalman Filter for Dynamic State Estimation", Online available: https://arxiv.org/ftp/arxiv/papers/1702/1702.00884.pdf.

Alatise, M.B., Hancke, G.P., 2017, "Pose Estimation of a Mobile Robot Based on Fusion of IMU Data and Vision Data Using an Extended Kalman Filter", Sensors (Basel), 17(10):2164.

Ali, A.S.A., 2013, "Low-Cost Sensors-Based Attitude Estimation for Pedestrian Navigation in GPS-Denied Environments", Doctoral thesis.

Amorin, R. and Broni-Bediako, E., (2010). Application of Minimum Curvature Method to Wellpath Calculations. Research Journal of Applied Sciences, Engineering and Technology 2(7): 679-686.

Analog device, "ADIS16448 data sheet", [Online] Available: https://www.analog.com/media/en/technical-documentation/data-sheets/adis16448.pdf"

Arsava, K.S., Kim, Y., EI-Korchi, T., and Park, H.S., 2013, "Nonlinear system identification of smart structures under high impact loads", Smart materials and structures, 22, pp.1-30.

Assa, A., Plataniotis, K.N., 2017, "Adaptive Kalman Filtering by Covariance Sampling", IEEE signal processing letters, Vol.24, No.9, pp.1288-1292.

Axelsson, P. and Norrlöf, M., 2012, "Method to Estimate the Position and Orientation of a Triaxial Accelerometer Mounted to an Industrial Manipulator", 10th International IFAC Symposium on Robot Control, Vol.45, pp. 283-288.

Ayaz, E., 2014, "A review study on mathematical methods for fault detection problems in induction motors", Balkan journal of electrical & computer engineering, Vol.2, No.3, pp.156-165.

Aydin, I., Celebi,B., S., Barmada, S., and Tucci,M., 2018, "Fuzzy integral-based multi-sensor fusion for arc detection in the pantograph-catenary system", Proc IMechE Part F: J Rail and Rapid Transit Vol. 232(1) 159–170.

Arachie, C., Huang, B., 2019, "Adversarial Label Learning", Association for the Advancement of Artificial Intelligence, Online available, http://people.cs.vt.edu/~bhuang/papers/arachie aaai19.pdf

Bancroft, J.B. and Lachapelle, G., 2011, "Data Fusion Algorithms for Multiple Inertial Measurement Units", Sensors, Vol.11, pp.6771-6798.

Basso, G.F., Amorim, T.G.S.D, Brito,A.V., Nascimento, T.P., 2017, "Kalman Filter with Dynamical Setting of Optimal Process Noise Covariance", IEEE Access, Vol.5, pp.8385-8393.

Bergamini, E., Ligorio, G., Summa, A., Vannozzi, G., Cappozzo, A. and Sabatini, A. M., 2014, "Estimating Orientation Using Magnetic and Inertial Sensors and Different Sensor Fusion Approaches: Accuracy Assessment in Manual and Locomotion Tasks", Sensors, Vol.14, pp. 18625-18649.

Bhuiyan, M.Z.H., Kuusniemi, H., Chen, L., Pei, L., Ruotsalainen, L., Guniness, R., Chen, R., 2013, "Performance Evaluation of Multi-Sensor Fusion Models in Indoor Navigation", Europian Journal of Navigation, Vol. 11 Number 2, pp.20-28.

Bistrovs, V., Kluga, A., 2010, "Distance Estimation using Intelligent Fusion of Navigation Data", Electronics and Electrical Engineering, No.5(101).

Bistrovs, V., Kluga, A., 2011, "MEMS INS/GPS Data Fusion using Particle Filter", Electronics and Electrical Engineering, No.6, 112, pp. 77-80.

Borenstein, J., Ojeda, L., Kwanmuang, S., 2009, "Heuristic Reduction of Gyro Drift For Personnel Tracking Systems", Journal of Navigation, Vol 62, No 1, pp.41-58.

Bourke, A. K., and Lyons, G. M., 2008, "A threshold-based fall-detection algorithm using a bi-axial gyroscope sensor," Med. Eng. Phys., vol. 30, no. 1, pp. 84–90.

Brigante, C.M.N., Abbate, N., A. Basile, Faulisi, A.C., and Sessa, S., 2011, "Towards Miniaturization of a MEMS-Based Wearable Motion Capture System", IEEE Trans. Ind. Electron., vol. 58, No. 8, pp. 3234–3241.

Brossard, M., Barrau, A., Bonnabel, S., 2019, "AI-IMU Dead-Reckoning", Online available: https://arxiv.org/pdf/1904.06064.pdf.

Buchanan, A., A.Finn, C., J.Love, J., Worthington, W.E., Lawson, F., Maus, S., Okewunmi, S., Poedjono, B., 2013, "Geomagnetic Referencing- The Real-Time Compass for Directional Drillers", Oilfield Review Autumn 2013:25, No.3.

Butta, M., and Sasada, I., "Sources of Noise in a Magnetometer Based on Orthogonal Fluxgate Operated in Fundamental Mode", IEEE TRANSACTIONS ON MAGNETICS, VOL. 48, NO. 4, APRIL 2012.

Cao, J., Zhu,X., Wu,H., and Zhang.,L., 2017, "A novel method of measuring spatial rotation angle using MEMS tilt sensors", Meas. Sci. Technol. 28 105907.

Cappello, F., Ramasamy, S., Sabatini, R., and Liu, J., 2015 "Low-Cost Sensors based Multi-sensor Data Fusion Techniques for RPAS Navigation and Guidance", International Conference on Unmanned Aircraft Systems (ICUAS), Denver, Colorado, USA, pp.714-722.

Casanova, O., Marichal, G.N., Gonzalez Mora, J.L., Hernandez, A., 2011, "A Low Cost Intelligent Localization System Based on a Camera and an Inertial Measurement Unit (IMU)", Proc. 7th conf. European Society for Fuzzy Logic and Technology, pp.705-711.

Chang, H.W., Chen, K.Y., Chiang, K.W., El-Sheimy, N., 2010, "Intelligent Sensor Positioning and Orientation using a SGN Embedded Fusion Algorithm for a MEMS IMU/GPS Integrated System", Canadian Geomatics Conf./Symposium of Commission I, Vol. 38, No.1, 7pp.

Chapelle, O., Scholkopf, B., Zien, A., 2006, "Semi-Supervised Learning", The MIT Press, Cambridge, Massachusetts, London, England

Chavez-Garcia, R. O., 2014, "Multiple Sensor Fusion for Detection, Classification and Tracking of Moving Objects in Driving Environments", Robotics Universit´e de Grenoble.

Chavez-Garcia, R.O., Aycard, O., 2016, "Multiple Sensor Fusion and Classification for Moving Object Detection and Tracking", IEEE Transactions on Intelligent Transportation Systems, Vol. 17, pp.525-534.

Choukroun, D., Weiss, H., Bar-itzhack, I.Y., Oshman, Y., 2008, "Direction Cosine Matrix Estimation from Vector Observations using a Matrix Kalman Filter", IEEE Transactions on aerospace and electronic systems, VOL.46, NO.1.

Chova, L.G., Moser, G. and Valls, G. C., 2015, "Multimodal Classification of Remote Sensing Images: A Review and Future Directions", Proc. IEEE, Vol.103, No.9, pp.1560-1584.

Collins, T., (2001). Corrosion resistance of non-magnetic drill collars. NACE International Corrossion, Houston, Texas

ElGizawy, M., (2009). Continuous Measurement-While-Drilling surveying system utilizing MEMS inertial sensors. UCGE Report.

Creal, D., 2011, "A Survey of Sequential Monte Carlo Methods for Economics and Finance", Econometric Reviews, Vol.31, 3, pp. 245-296.

Cutler, A., 2010, "Random Forests for Regression and Classification", [Online]. Available: http://www.math.usu.edu/~adele/RandomForests/Ovronnaz.pdf

Denoual, M., Fodil, K., Dolabdjian, C., Kauffmann, F., "Magnetic sensor noise impact on the evaluation of magnetorelaxometry experiments", International Conference on Noise and Fluctuations (ICNF), 2013, Montpellier, France.

Diebel, J., 2006, "Representing Attitude: Euler Angles, Unit Quaternions, and Rotation Vectors", [Online]. Available: https://www.astro.rug.nl/software/kapteyn-beta/_downloads/attitude.pdf .

Docebo, 2019, "Earth's Magnetic Field", [Online]. Available: https://studylib.net/doc/18915682/earth-s-magnetic-field

Dong, J., Zhuang, D., Huang, Y. and Fu, J., 2009, "Advances in Multi-Sensor Data Fusion: Algorithms and Applications", Sensors, Vol.9, pp.7771-7784.

Du, J., Gerdtman, C., Lindén, M., 2018, "Signal Quality Improvement Algorithms for MEMS Gyroscope-Based Human Motion Analysis Systems: A Systematic Review", Sensors, V.18 (4), 18 pages.

Du, S., 2010, "Integration of Precise Point Positioning and Low Cost MEMS IMU", Ph.D Thesis, University of Calgary.

Edvardsen, I., Nyrnes, E., et al, 2014, "Improving the Accuracy and Reliability of MWD/Magnetic-Wellbore-Directional Surveying in the Barents Sea", 2014 SPE Drilling & Completion, pp.215-225

Eldesoky, A., Kamel,. A.M., Elhabiby, M., Elhennawy, H., 2017, "Performance enhancement of low-cost MEMS inertial sensors using extensive calibration technique", IEEE 34th National Radio Science Conference (NRSC), Alexandria, Egypt.

ElGizawy, M. L., 2009, "Continuous Measurement-While-Drilling Surveying System Utilizing MEMS Inertial Sensors", UCGE Report.

ElGizawy, M., Noureldin, A., Georgy, J., U. Iqbal and El-Sheimy, N., 2010, "Wellbore Surveying While Drilling Based on Kalman Filtering", American J. of Engineering and Applied Sciences, Vol.3, pp. 240-259.

Elshafei, M., Baig, M.M., Mysorewala, M.,F., AI-Majed, A.A., (2015). Control and optimization of directional drilling system. SPE Middle East Intelligent Oil and Gas Conference and Exhibition, 15-16 September, Abu Dhabi, UAE, pp.10.

EMFSinfo, 2019, Online available: http://www.emfs.info/what/distance/

Fan, B., Li, Q., Liu, T., 2017, “How Magnetic Disturbance Influences the Attitude and Heading in Magnetic and Inertial Sensor-Based Orientation Estimation”, Sensors, 18, 76, 27 pages.

Fang, H., Tian, N., Wang, Y., Zhou, M.C., Haile, M.A., 2017, “Nonlinear Bayesian Estimation: From Kalman Filtering to a Broader Horizon”, Online available: https://arxiv.org/pdf/1712.01406.pdf.

Farias, G., Fabregas, E., et al. 2018, “A Neural Network Approach for Building an Obstacle Detection Model by Fusion of Proximity Sensors Data”, sensors, 18, 683.

Ferguson, J., 2015, “Calibration of Deterministic IMU Errors”, http://commons.erau.edu/pr-honors-coe/2.

Feng, K., Li, J., Zhang, X., Shen, C., Bi,Y., Zheng, T., Liu, J., 2017, “A New Quaternion-Based Kalman Filter for Real-Time Attitude Estimation Using the Two-Step Geometrically-Intuitive Correction Algorithm”, Sensors, 2017, 17, 21 pages.

Gaedeke, T., Hohnson, M., Hedley M., and Stork, W., 2014, “Fusion of Wireless Ranging and Inertial Sensors for Precise and Scalable Indoor Localization”, Proc. IEEE Int. Conf. Communications Workshops, pp. 138-143.

Gao, B., Hu, G., Gao,S., Zhong, Y., and Gul, C., 2018 “Multi-Sensor Optimal Data Fusion Based on the Adaptive Fading Unscented Kalman Filter”, Sensors, 18, 488, pp. 22.

Ghanbari, M., Yazdanpanah, M.J., 2015, ”Delay Compensation of Tilt Sensors Based on MEMS Accelerometer using Data Fusion Techniques”, IEEE Sensors J., Vol.15, No.3, pp. 1959-1966.

Girard, G., Côté, S., Zlatanova, S., Barette, Y., St-Pierre, J. and Oosterom, P., 2011, "Indoor Pedestrian Navigation Using Foot-Mounted IMU and Portable Ultrasound Range Sensors", Sensors, Vol.11, pp. 7606-7624.

Glueck, M., Oshimubi, D., Manoli, Y., 2015, “Automatic Real-Time Offset Calibration of Gyroscopes”, Microsyst Technol, 21, 429-443.

Goodall, C.L., 2009, “Improving Usability of Low-Cost INS/GPS Navigation Systems using Intelligent Techniques”, UCGE Report.

Gooneratne, C.P., Li, B., and Moellendick, T.E., “Downhole Applications of Magnetic Sensor”, Sensors, 17, 2384, 32 pages, 2017.

Gebre-Egziabher, D., Hayward, R.C. Powell,J.D., 2004 “Design of Multi-Sensor Attitude Determination Systems”, IEEE TRANSACTIONS ON AEROSPACE AND ELECTRONIC SYSTEMS VOL. 40, NO. 2 APRIL 2004, pp.627-649

Geomagnetism Canada, [Online]. Available: https://geomag.nrcan.gc.ca/index-en.php.

Ghahramani, Z., 2004, “Unsupervised Learning”, Machine Learning 2003, LNAI 3176, pp.72-112.

Groÿekatthöfer, K., Yoon, Z., 2012, “Introduction into Quaternions for Spacecraft Attitude Representation,” [Online]. Available: http://www.tu-berlin.de/fileadmin/fg169/miscellaneous/Quaternions.pdf.

Hasan, M.G., Hasan, M.K., Ahsan, R., Sultana, T., Bhowmik, R.C., 2013, “Evaluation of a Low-Cost MEMS IMU for Indoor Positioning System”, International Journal of Emerging Science and Engineering, Vol-1, Issue-1.

Helm. I., Jalukse, L., Leito, I., 2010, “Measurement Uncertainty Estimation in Amperometric Sensors: A Tutorial Review”, Sensors 2010, 10, pp. 4430-4455.

Hellmers, H., Nordine, A., Blankenbach, J. and Eichhorn, A., 2013, "AN IMU/MAGNETOMETER-BASED INDOOR POSITIONING SYSTEM USING KALMAN FILTERING", International Conference on Indoor Positioning and Indoor Navigation.

Hemanth, K.S., Talasila, V., Rao, S., 2012, “Calibration of 3-axis Magnetometers”, IFAC Proceedings Volumes, Volume 45, Issue 1, pp.175-178.

Henderson, C., 2009, “Correcting errors inherent in directional surveying with MWD tools”, World Oil, 2009, 29.

Hirama, I., 2015, “New MEMS Sensor Process by TSV Technology for Smaller Packging”, ICEP-IAAC 2015 Proceedings, 456-459.

Hisz, D.B., Murdoch, L.C., and Germanovich, L. N., 2013, “A portable borehole extensometer and tiltmeter for characterizing aquifers”, WATER RESOURCES RESEARCH, Vol.49, pp. 7900–7910.

Hwang, D., Lee, J.H., Moon, S., Park, S.W., Woo, J., Kim, C., 2017, "The reliability of the non-radiologic measures of thoracic spine rotation in healthy adults", Physical Therapy Rehabilitation Science, Vol. 6, pp. 65-70.

Hyun, D., Yang, H.S., Park, H.S., Kim, H.J., 2010, “Dead-reckoning Sensor System and Tracking Algorithm for 3-D Pipeline Mapping”, Mechatronics, 20, pp.213-223.

Ilyas, M., Cho, K., Baeg, S. and Park, S., 2016, "Drift Reduction in Pedestrian Navigation System by Exploiting Motion Constraints and Magnetic Field", Sensors, Vol.16, 25 pages.

Iozan,L.I., Kirkko-Jaakkola,M., Collin,J., Takala,J. and Rusu, C.,2016, “Using a MEMS gyroscope to measure the Earth's rotation for gyrocompassing applications”, Measurement Science and Technology 23(2):025005.

Jain, S., 2017, “Introduction to Pseudo-Labelling: A Semi-supervised Learning Technique”, Online available: https://www.analyticsvidhya.com/blog/2017/09/pseudo-labelling-semi-supervised-learning-technique/.

Jeon, D., Eun, Y., 2014, "Distributed asynchronous multiple sensor fusion with nonlinear multiple models", Aerospace Science and Technology, Vol.39, pp. 692-704.

Jiang, Q., Zeng, Y., Q. Liu, Jing, H., 2012, “Attitude and Azimuth Reference System for Quadrotor Based on MEMS Sensors”, Proc. IEEE 2nd Int. Instrumentation & Measurement, Computer, Communication and Control, pp. 1090-1093.

Jogschies, L., Klaas, D., Kruppe, R., Rittinger, J., Taptimthong, P., A. Wienecke, L. Rissing and M. C. Wurz, 2015, “Recent Developments of Magnetoresistive Sensors for Industrial Applications”, Sensors, Vol.15, pp.28665-28689.

Julier, S., Uhlmann, J.K., 1996, “A General Method for Approximating Nonlinear Transformations of Probability”, [Online]. Available: https://pdfs.semanticscholar.org/523a/ 865ffabb50d10f85d141963d40528e952760.pdf.

Johann, C. , Philippe,C., Alain, G., 2006, “Micromachined high sensitivity thermal inclinometer”, Sensor Review,Vol.26, pp.203-208.

Kalandros, M.K., Trailovic, L., Pao, L.Y., Bar-Shalom, Y., 2004, “Tutorial on Multisensor Management and Fusion Algorithms for Target Tracking”, Proceedings of the 2004 American Control Conference, Boston, Massachusetts, pp. 4734-4748.

Kao, C.F., Chen, T.L., 2008 “Design and analysis of an orientation estimation system using coplanar gyro-free inertial measurement unit and magnetic sensors”, Sensors and Actuators (A) 144, 251–262.

Kaur, M., Kakar, S., Mandal, D., 2011, “Electromagnetic Interference”, 2011 3rd International Conference on Electronics Computer Technology, 5 pages.

Khot, L.R., Tang, L., Steward, B.L., Han, S., 2006, “Sensor Fusion for Roll and Pitch Estimation Improvement of an Agricultural Sprayer Vehicle”, ASABE Paper No.061159, [Online]. Available: https://pdfs.semanticscholar.org/6180/d57d5f3c9819b95806c02eaee3f4b7a6962b.pdf.

Kionix,” Using Two Tri-Axis Accelerometers for Rotational Measurements”, 8 pages, [Online]. Available: http://kionixfs.kionix.com/en/document/AN019.pdf 2008.

Kim, N., Kim, Y., 2015, "Indoor Positioning System with IMU, Map Matching, and Particle Filter", Recent Advances in Electrical Engineering and Computer Science, pp. 41-47.

Kim, J., Lee, S., 2016, “A Vehicular Positioning with GPS/IMU Using Adaptive Control of Filter Noise Covariance”, ICT Express, Vol.2, 1, pp.41-46.

Kok, M., Hol, J.D. and Schon, T.B., 2017, “Using Inertial Sensors for Position and Orientation Estimation”, Foundations and Trends in Signal Processing, Vol.11, No.1-2, 153 pages.

Koksal, N., Jalalmaab, M., Fidan, B., 2019, “Adaptive Linear Quadratic Attitude Tracking Control of a Quadrotor UAV Based on IMU Sensor Data Fusion”, Sensors (Basel), 2019, 19(1):46, 23 pages.

Ladetto, Q., Seeters, J.van, Sokolowski, S., Sagan, Z., Merminod, B., 2002, “Digital Magnetic Compass and Gyroscope for Dismounted Soldier Position & Navigation”, NATO Research and Technology Agency, Sensors & Electronics Technology Panel, NATO meetings, 15 pages.

Larin,V., Tunik,A., 2012 “Gyro-free Accelerometer-based SINS: Algorithms and Structures”, 2nd International Conference "Methods and Systems of Navigation and Motion Control" (MSNMC), October 9-12, Kiev, Ukraine pp.18-26.

Latt, W. T., Veluvolu, K. C. and Ang, W. T., 2011, "Drift-Free Position Estimation of Periodic or Quasi-Periodic Motion Using Inertial Sensors", Sensors, Vol.11, pp.5931-5951.

Lee, CG., Dao, NN., Jang, S., Km, D., Kim, Y., and Cho, S., 2016, “Gyro Drift Correction for An Indirect Kalman Filter Based Sensor Fusion Driver”, Sensors, 16, 864, 11 pages.

Lei, Y., Lin, J., He, Z., and Kong, D., 2012, ” A Method Based on Multi-Sensor Data Fusion for Fault Detection of Planetary Gearboxes” , Sensors, 12, pp.2005-2017.

Lentsch, D., Savvatis, A., Schubert, A., and Schoebel, W., (2012). Overcoming Drilling Challenges With Rotary Steerable Technology in Deep Geothermal Wells in the Molasse Basin of Southern Germany. GRC Transactions, Vol. 36.

Li, L., Pan, Y., Lee, J.K., Ren, C., Liu, Y., Grejner-Brzezinska, D.A., Toth, C.K., 2012, “Cart-Mounted Geolocation System for Unexploded Ordnance With Adaptive ZUPT Assistance”, IEEE Transaction on Instrumentation and Measurement, Vol. 61, No.4, pp. 974-979.

Li, J., Broas, M., Makkonen, J., Mattila, TT., Hokka, J., and Paulasto-Kröckel, M., 2014, “Shock Impact Reliability and Failure Analysis of a Three-Axis MEMS Gyroscope”, JOURNAL OF MICROELECTROMECHANICAL SYSTEMS, VOL. 23, NO. 2, pp.347-355.

Li, W., Jia, Y., Du, J., 2017, “Distributed Extended Kalman Filter with Nonlinear Consensus Estimate”, Journal of the Franklin Institute, Vol. 354, 17, pp. 7983-7995.

Li, C.I., Chen, G.D., Sung, T.Y., Tsai, H.F., 2019, “Novel Adaptive Kalman Filter with Fuzzy Neural Network for Trajectory Estimation System”, International Journal of Fuzzy Systems.

Lin, Z., Zecca, M., S. Sessa, L. Bartolomeo, Ishii, H., Takanishi, A., 2011, “Development of the Wireless Ultra-Miniaturized Inertial Measurement Unit WB-4; Preliminary Performance Evaluation”, Proc. IEEE Int. Medicine & Biology, pp. 6927-6930.

Liu, H., Shor, R., Park, S., (2018). Intelligent Filter for Accurate Subsurface Heading Estimation Using Multiple Integrated MEMS Sensors. IEEE Sensors 2018, New Delhi, India.

Liu, H., Shor, R., Park, S.S., 2019, “Intelligent Wellbore Path Estimation Using Multiple Integrated MEMS Sensors”, SPE-194127_MS, SPE/IADC Drilling Conference and Exhibition, 2019, The Hague, The Netherlands, 22 pages.

Liu, S., Atia, M.M., Y. Gao and Noureldin, A., 2015, “Adaptive Covariance Estimation Method for LiDAR-Aided Multi-Sensor Integrated Navigation Systems”, Micromachines, 6, pp. 196-215.

Liu, Y.X., Li, X.S., Zhang, X.J., and Feng, Y.B., 2014, “Novel Calibration Algorithm for a Three-Axis Strapdown Magnetometer”, Sensors, 14, pp.8485-8504.

Loganathan, C., Girija, K.V., 2013, “Hybrid Learning for Adaptive Neuro Fuzzy Inference System”, International Journal of Engineering And Science, Vol.2, Issue (11), pp.6-13.

Looney, M., 2010, “A Simple Calibration for MEMS Gyroscopes”, http://www.analog.com/media /en/technical-documentation/technical-articles/GyroCalibration_EDN_EU_7_2010.pdf.

Looney, M., 2015, “The Basics of MEMS IMU/Gyroscope Alignment”, http://www.analog.com/ library/analogDialogue/archives/49-06/IMU_Gyroscope.html.

Lowdon, R., 2014, “Demystifying Petroleum Engineering”, SPE Aberdeen Simplified Series.

Lu, Z.J., Xiang, Q., Xu, L., 2014, “An Application Case Study on Multi-sensor Data fusion System for Intelligent Process Monitoring”, Procedia CIRP, Vol 17, pp. 721-725.

Luinge, H.J., 2002 "Inertial Sensing of Human Movement", book, Twente University Press.

Luo, R. C., Chang, C.C., and Lai, C.C., 2011, “Multisensor Fusion and Integration: Theories, Applications, and its perspectives”, IEEE Sensors J., Vol.11, No.12, pp. 3122-3138.

Lyons, T., Arribas, I.P., 2018, “Labelling as an unsupervised learning problem”, Online available: https://arxiv.org/abs/1805.03911

Madgwick, S.O., 2010, “An efficient orientation filter for inertial and inertial/magnetic sensor arrays”, Report, x-io Technologies Limited, April 30, [Online]. Available: http://www.x-io.co.uk/opensource-imu-and-ahrs-algorithms/.

Madgwick, S.O.H., Harrison, A.J.L., Vaidyanathan, R., 2011, “Estimation of IMU and MARG orientation using a gradient descent algorithm”, Proc. IEEE Int. Rehabilitation Robotics, pp. 1-7.

Makni, A., Fourati, H., and Kibangou, A., 2014, “Adaptive Kalman Filter for MEMS-IMU Based Attitude estimation under External Acceleration and Parsimonious use of Gyroscopes”, Proc. European Conf. Control.

Mansuclal, J.P., 2010, “Tilt Compensated Digital Compass”, Master thesis.

Mathur, N., Glesk, I., Buis, A., 2016, “Comparison of Adaptive Neuro-Fuzzy Inference System (ANFIS) and Gaussian Processes for Machine Learning (GPML) Algorithms for the Prediction of Skin Temperature in Lower Limb Prostheses”, Medical Engineering & Physics, Vol (38), Issue (10), pp. 1083-1089.

McElhinney, Margeirsson, G.A., Jaroboranir, A., Hamlin, K., and Blok, I., 2000, “Gravity Azimuth: A New Technique to Determine Your Well Path”, IADC/SPE Drilling Conference.

Moreland, C., 2002, “Fluxgate Magnetometer”, https://www.scribd.com/document/71833550/Fluxgate-Magnetometer-Cct.

Nilashi, M., Bagherifard, K., Ibrahim, O., Janahmadi, N., and Barisami, M., 2011, “An application expert system for evaluating effective factors on trust in B2C Websites”, Engineering, 3, pp.1063-1071.

Nilsson, J. and Skog, I., 2016, “Inertial Sensor Arrays – A Literature Review”, IEEE, 2016 European Navigation Conference, pp.10, Helsinki, Finland.

Norton, A., 2009, “10 things you should know about USB 2.0 and 3.0”, Online available: https://www.techrepublic.com/blog/10-things/10-things-you-should-know-about-usb-20-and-30/

Noureldin, A., 2002, “New Measurement-While-Drilling Surveying Technique Utilizing Sets of Fiber Optic Rotation Sensors”, Ph.D Thesis, University of Calgary.

Noureldin, A., Karamat, T.B., Eberts, M.D., and EI-Shafie, A., 2009, “Performance Enhancement of MEMS-based INS/GPS Integration for Low-Cost Navigation Applications”, IEEE Trans. Veh.Technol., Vol. 58, No.3, pp. 1077-1096.

Ozzmaker, 2014, “Calculating Compass Heading”, [Online]. Available: http://space1352.rssing.com/chan-5873254/latest.php.

Parnian, N., 2008, “Integration of Local Positioning System & Strapdown Inertial Navigation System for Hand-Held Tool Tracking”, Ph.D Thesis.

Pasquale, G., D., 2010, “Reliability Testing Procedure for MEMS IMUs Applied to Vibrating Environments”, Sensors, 10, pp. 456-474.

Patonis, P., Patias, P., Tziavos, I.N., Rossikopoulos, D., Margaritis, K., G., 2018, “A Fusion Method for Combining Low-Cost IMU/Magnetometer Outputs for Use in Applications on Mobile Devices”, Sensors, 18(8).

Pei, Y., 2017, “An Elementary Introduction to Kalman Filtering”, [Online]. Available: https://arxiv.org/pdf/1710.04055.pdf.

Pettersson, O., 2005, “Execution Monitoring in Robotics: A Survey”, Robotics and Autonomous Systems, 53 (2005), pp. 73-88.

Qazizada, M.E., Pivarčiová, E., 2016, “Mobile robot controlling possibilities of inertial navigation system”, Procedia Engineering 149 (2016) 404 – 413.

Quoc, D.D., Sun, J., Le, V.N., Luo, L., 2015, “Complementary Filter Performance Enhancement through Filter Gain”, International Journal of Signal Processing, Image Processing and Pattern Recognition, Vol.8 No.7, pp.97-110.

Ren, Y., Wang, Y., Wang, M., Wu, S. and Wei, B., 2014, "A Measuring System for Well Logging Attitude and a Method of Sensor Calibration", Sensors, Vol. 14, pp. 9256-9270.

Renaudin, V., Afzal, M.H., and Lachapelle, G., 2010, “Complete Triaxis Magnetometer Calibration in the Magnetic Domain”, Journal of Sensors, Vol 2010, pp.1-10.

Renaudin, V., Combettes, C., 2014, “Magnetic, Acceleration Fields and Gyroscope Quaternion (MAGYQ)-Based Attitude Estimation with Smartphone Sensors for Indoor Pedestrian Navigation”, Sensors, 14, pp. 22864-22890.

Roberts, J.T., Ali, H.H., 1993, “Using the bubble inclinometer to measure laryngeal tilt and predict difficulty of laryngoscopy”, Journal of Clinical Anesthesia, Vol.5, pp. 306-309.

Rotate drilling motor, Online available: http://www.rotatemotor.com/bent-housing/

Roth, D., 2016, “Introduction to Machine Learning”, Online available: http://l2r.cs.uiuc.edu/ Teaching/ CS446-17/LectureNotesNew/intro/main.pdf.

Russel, A.W., Roesler, R.F., (1985). Reduction of nonmagnetic drill collar length through magnetic azimuth correction technique. SPE/IADC Drilling Conference, New Orleans, Lousiana.

Rusu-Casandra, A., Marghescu, I., Lohan, E.S., 2010, “Estimators of the Indoor Channel for GPS-based Pseudolite Signal”, 2010 9th International Symposium on Electronics and Telecommunications, 4 pages.

Sadaghzadeh, N., Poshtan, J., A. Wagner, Nordheimer, E., Badreddin, E., 2014, “Cascade Kalman and Particle Filters for Photogrammetry Based Gyroscope Drift and Robot Attitude Estimation”, ISA Trans. 53, pp. 524-532.

Salmeron-Quiroz, B.B., Villegas-Medina, G., Guerrero-Castellanos, J.F., Villalobos-Martinez, R., Mendoza-Nunez, M.A., 2013, “Data Fusion of an Attitude Estimator for Global Localization of a Robot”, Proc. 10th Int. Conf. Body Sensor Networks, 6 pages.

Sampaio, J.H.B., (2007). Planning 3D Well Trajectories Using Spline-in-Tension Functions. journal of Energy Resources Technology, 129(4).

Saxena, A., Gupta, G., Gerasimov, V., Ourselin, S., 2005, “In Use Parameter Estimation of Inertial Sensors by Detecting Multilevel Quasi-static States”, KES 2005, LNAI 3684, pp. 595-601.

Shor, R.J., Dykstra, M.W., Hoffmann, O.J., Coming, M., 2015, “For Better or Worse: APPlications of the Transfer Matrix Approach for Analyzing Axial and Torsional Vibration”, SPE/IADC-173121-MS, Drilling Conference and Exhibition held in London, UK.

Shen, Y., Zhu, Z., Mao, E., 2007, “Double-Fuzzy Kalman Filter Based on GPS/IMU/MV Sensor Fusion for Tractor Autonomous Guidance”, Proceedings of the IEEE International Conference on Automation and Logistics, Jinan, China.

Sherrett, J.L., 2013, “A Comparison of Navigation Systems Based on Inertial Sensor Selection and Configuration”, book

Shkel, A.M., 2001, “Micromachined Gyroscopes: Challenges, Design Solutions, and Opportunities”, Smart Structure and Materials 2001: Smart Electronics and MEMS, Proceedings of SPIE Vol.4334

Sivaraman, S., and Trivedi, M. M., 2013, “Looking at Vehicles on the Road: A Survey of Vision-Based Vehicle Detection, Tracking, and Behavior Analysis”, IEEE Trans. Intell. Transp. Syst., vol. 14, No. 4, pp. 1773–1795.

Smith, D., and Singh, S., 2006, “Approaches to Multisensor Data Fusion in Target Tracking: A Survey”, IEEE Trans. Knowl. Data Eng., vol. 18, No. 12, pp. 1696–1710.

Song, H., Huang, H., Zhang, J., Qu, D., 2018, “A new measurement-while-drilling system based on inertial technology”, Advanced in Mechanical Engineering, Vol.10, Issue 3, 14 pages.

Sprager, S., and Juric, M.B., 2015, "Inertial Sensor-Based Gait Recognition: A Review", Sensors, Vol.15, pp.22089-22127

Stockhausen, E., Ball, R., Clark, P., Mongan, R., and Rice P., 2016, “Placement Matters: Improving Survey Accuracy by Using Continuous Directional Data and Drilling Parameter Setting”, AAPG Annual Convention and Exhibition, Calgary, Alberta, Canada.

Subramanian, V., Burks, T.F., Dixon, W.E., 2009, “Sensor Fusion Using Fuzzy Logic Enhanced Kalman Filter for Autonomous Vehicle Guidance in Citrus Groves”, Transactions of the ASABE, Vol.52(5): 1411-1422.

Tan, T., Peng, A., Huang, J., Zheng, L., Ou, G., 2018, “A Gyroscope Bias Estimation Algorithm Based on Map Specific Information”, Sensors, 18(8), 10 pages.

Tang, J., Deng, Z., Quan, Q., Jiang, S., 2016, “Real-Time Drilling Strategy for Planetary Sampling: Method and Validation”, J. Aerosp. Eng. 29 (5)

Tarokh, A.B., Miller, E.L., 2007, "Subsurface Sensing Under Sensor Positional Uncertainty", IEEE Transactions on Geoscience and Remote Sensing, Vol.45, pp.675-688.

Trimble, (2012). Trimble R10 GNSS Receiver. https://www.neigps.com/wp-content/uploads/2014/01/R10-UserGuide.pdf.

Trimpe, S. and D'Andrea, R., 2010, "Accelerometer-based Tilt Estimation of a Rigid Body with only Rotational Degrees of Freedom", 2010 IEEE International Conference on Robotics and Automation, pp. 2630-2636.

Tsai, Y.L., Tu, T.T., Bae,H., Chou, P.H., 2010, “EcoIMU: A Dual Triaxial-Accelerometer Inertial Measurement Unit for Wearable Applications”, IEEE 2010 International Conference on Body Sensor Networks, Singapore.

Valade, A., Acco, P., Grabolosa, P., Fourniols, J.Y., 2017, “A Study about Kalman Filters Applied to Embedded Sensors”, Sensors, 17, 2810.

Vasco, D.W., Keer, H., Karasaki, K., 2000, “Estimation of reservoir properties using transient pressure data: An asymptotic approach”, Water Resource Research, Vol 36, pp.3447-3465.

Vasconcelos, J.F., Silverstre, C., Oliveira, P., Batista, P., and Cardeira, B., 2009, “Discrete Time-Varying Attitude Complementary Filter”, 2009 American Control Conference, St. Louis, Mo, USA

Vecchione, G.A., Palenzuela, D., Toledo, M., 2010, “Dingpos, a GNSS-based Multi-sensor Demonstrator for Indoor Navigation: Preliminary Results”, IEEE-ION Position Location and Navigation Symposium, pp. 670-678.

Wang, H., Lenz, H., Szabo, A., 2007, “WLAN-Based Pedestrian Tracking Using Particle Filters and Low-Cost MEMS Sensors”, 4th Workshop Poss. Navigation & Comm.

Wang, X., Yang, C., 2014, “Constructing Gyro-free Inertial Measurement Unit from Dual Accelerometers for Gesture Detection”, Sensors & Transducers, Vol. 171, Issue 5, pp. 134-140.

Wang, Z., Yin, X., Li, P., Wan, L., 2014, “Application of Rotation Vector Algorithm for SINS Attitude Updating”, Proc. IEEE 12th Int. Conf. Signal Processing, pp. 2390-2393.

Wang, Z., 2011, “Machine Learning Based Mapping of Data and Streaming Parallelism to Multi-cores”, Ph.D Thesis, University of Edinburgh.

Wang, Y., Liu, Z., Chen, J., Zhao, D., Song, C., 2010, “An improved unscented Kalman filter for projectile’s attitude determination”, Control and Decision Conference, China.

Warpinski, N.R., 2013, “Understanding Hydraulic Fracture Growth, Effectiveness, and Safety Through Microseimic Monitoring”, INTECH.

Widodo, R.B., Wada, C., 2016, “Attitude Estimation Using Kalman Filtering: External Acceleration Compensation Considerations”, Journal of Sensors, Vol.2016, 24 pages.

Woodman, O.J., 2007, “An introduction to inertial navigation”, Technical Report, [Online]. Available: https://www.cl.cam.ac.uk/techreports/UCAM-CL-TR-696.pdf.

Wozniak, P., Mehner-Heindl, K., “Orientation Determination for Android Smartphones,” SLERP Quaternion-MenschComputer 2015, [Online]. Available: http://www.katharina-mehner.de/WozniakMehner-Heindl2016_ToBeSubmitted.pdf.

Wu, F., Vibhute, A., Soh, G.S., Wood, K.L., Foong, S., “A compact magnetic field-based obstacle detection and avoidance system for miniature spherical robots”, sensors 2017, 17, 1231.

Xia, L., Wang, J., Yan, G., 2009, “RBFNN aided extended kalman filter for MEMS AHRS/GPS”, 6th Int. Conf. Embedded Software and Systems Location, pp. 559-564.

Xue, Q., Leung, H., Wang, R., Liu, B., Yu, Y., 2016, “Continuous Real-Time Measurement of Drilling Trajectory With New State-Space Models of Kalman Filter”, IEEE Trans. Instrum. Meas., Vol.65, pp.144-154.

Xue, Q.L., Wang, R.H., Sun, F, Huang, L.L., Han, L.J., 2014, “Continuous measurement-while-drilling Utilizing Strap-down Multi-model Surveying System”, IEEE Trans. Instrum. Meas., Vol.63, pp.650-657.

Yang, D., You, Z., Li, B., Duan, W., and Yuan, B., 2017, “Complete Tri-Axis Magnetometer Calibration with a Gyro Auxiliary”, Sensors, 17, 1223, 21 pages.

Yang, H., Li, W., Luo, T., Luo, C., 2017, “Research on the Strategy of Motion Constraint-Aided ZUPT for SINS Position System of a Shearer”, micromachines, 2017, 8, 340, 16 pages.

Yuan, X., Yu, S., S. Zhang, Wang G., and Liu, S., 2015, “Quaternion-Based Unscented Kalman Filter for Accurate Indoor Azimuth Estimation Using Wearable Multi-Sensor System”, Sensors, Vol.15, pp.10872-10890.

Hadavand, Z., 2015, “Reduction of Wellbore Positional Uncertainty During Directional Drilling”, Master Thesis, University of Calgary.

Zlotnik, D.E., Forbes, J.R., 2018, “Higher-Order Nonlinear Complementary Filtering on Lie Groups”, [Online]. Available: https://arxiv.org/pdf/1804.02414.pdf.

Zhang, C., and Lin, T., 2016, “A Long-Term Performance Enhancement Method for FOG-Based Measurement While Drilling”, Sensors, Vol.16, 1186.

Zhang, P., Gu, J., Milios, E.E., Huynh, P., 2005, “Navigation with IMU/GPS/Digital Compass with Unscented Kalman Filter”, Proceedings of the IEEE International Conference on Mechatronics & Automation, Niagara Falls, Canada.

Zhang, R., and Reindl, L.M., 2011, “Pedestrian Motion based Inertial Sensor Fusion by a Modified Complementary Separate-bias Kalman Filter”, Proc. IEEE Int. Conf. Sensors Applications, pp. 209-213.

Zhou, J., Jiang, T., Jiao, J. et al. 2014, “Design and fabrication of a micromachined gyroscope with high shock resistance”, Microsyst Technol (2014) 20: 137.

Zhou, L., Fei, M., Du, D., Li, W., Hu, H., Rakic A., 2019, “A Novel QGA-UKF Algorithm for Dynamic State Estimationof Power System”, International Symposium on Neural Networks, pp.240-250.

LIST OF PUBLICATIONS

Published

1. **Liu, H.,** Shor, R., Park, S.S., 2019, "Intelligent Wellbore Path Estimation Using Multiple Integrated MEMS Sensors", SPE-194127_MS, SPE/IADC Drilling Conference and Exhibition, 2019, The Hague, The Netherlands, 22 pages.

2. **Liu, H.,** Shor, R., Park, S., 2018, "Intelligent Filter for Accurate Subsurface Heading Estimation Using Multiple Integrated MEMS Sensors", IEEE Sensors 2018, New Delhi, India, 4 pages.

3. **Liu, H.,** Shor, R., Park, S., 2018, "Continuous Wellbore Path Estimation Using Multiple Integrated MEMS Sensors", 47^{th} General Meeting of SPE Wellbore Positioning Technical Section: Industry Steering Committee on Wellbore Survey Accuracy (ISCWSA), Inverness, Scotland.

Ready to Submit

4. **Liu, H.,** Shor, R., Park, S.S., 2019, "Data Fusion by a Supervised Learning Method for Orientation Esitimation Using Sensor Array Under Conditions of Magnetic Distortion and Shock Impact".

APPENDIX

SPE COPYRIGHT FORM

Meeting Name and Year SPE/IADC Drilling Conference and Exhibition, 2019, The Hague, The Netherlands

The Society of Petroleum Engineers (SPE) appreciates your willingness to contribute your paper to SPE. Transfer of copyright to SPE is a requirement for publication, including publication in conference proceedings, with the exception of material that is in the public domain (i.e., is not subject to copyright). Under this agreement, authors and their employers retain certain rights to make copies and reuse the material (refer to the Author-Retained Rights and Terms and Conditions on the back of this form). **The author/employer also retains any and all rights to any proprietary material disclosed in the paper.** This process allows for maximum dissemination of the information while maximizing protection against infringement by third parties. Under the terms of U.S. copyright law, an assignment of copyright must be a written, signed document from the owner of the work. Copyright assignment protects reproduction and distribution of the paper. SPE shall control the use and may offer to sell and/or collect royalties for use of the paper.

Publications are critical in SPE's mission to collect and disseminate knowledge concerning the exploration, development and production of oil and gas resources, and related technologies, for the public benefit; and to help industry professionals enhance their technical and professional competence. To meet these objectives freely and effectively, SPE does not accept limited permissions, including special licenses, to publish. This SPE Copyright Form must accompany and be executed for any original material to be published by SPE, including publication in conference proceedings. To ensure uniform treatment among all contributors, other forms may not be substituted for this form, nor may any wording of this form be changed.

Paper Number SPE-194127-MS

Paper Title Intelligent Wellbore Path Estimation Using Multiple Integrated MEMS Sensors

Please complete either Section A, B, or C, whichever is appropriate.

A. Copyright Transfer

The undersigned hereby assigns to the Society of Petroleum Engineers all publication and distribution rights under copyright for the above-cited paper and for any derivative works (abstracts, synopses, articles, and translations) based on the above-cited paper. The undersigned hereby warrants that (1) he/she is the author of the above-cited paper or (2) is authorized to represent the author on behalf of the author's employer, and (3) to the extent that the paper incorporates text passages, figures, data, or other materials from the works of others, the undersigned has obtained any necessary permissions.

- In the event the above-cited paper is not published by SPE within 6 months of submission, SPE will, upon request, return copyright to the original copyright holder and all copies of the paper submitted to SPE will be destroyed.
- For jointly authored papers, each author should sign a form. However, one author may sign as authorized agent for the others.

Huan Liu
Author/Authorized Agent Name (Please Print)

Author/Authorized Agent Signature

University of Calgary, Researcher
Company and Job Title

6-11 ÔÂ-2018
Date

B. United States Government Employee Certification

This will certify that all authors of the paper are U.S. government employees and prepared the paper within the scope of their official duties. As such, the paper is not subject to U.S. copyright protection.

Author/Authorized Signature

Date

C. Crown Copyright Certification

This will certify that all authors of the paper are employees of the British or British Commonwealth government and prepared the paper in connection with their official duties. As such, the paper is subject to Crown Copyright and is not assigned to SPE. The undersigned acknowledges, however, that SPE has the right to publish, distribute and reproduce the paper in all forms and media.

Author/Authorized Signature

Date

PLEASE READ AUTHOR-RETAINED RIGHTS AND TERMS AND CONDITIONS ON REVERSE SIDE.
(This form may be reproduced for each additional author.)

SPE COPYRIGHT FORM (continued)

Author-Retained Rights and Terms and Conditions

The term "employers" in the following means the companies*, universities, or organizations for which the authors worked at the time the paper was written. SPE's intent is that authors/employers maintain the ability to use the paper and the information in the paper (including images, graphs, figures, individual sections of the paper) for their business needs, including internal distribution within the authors' employers and business partners.

1. Authors/employers retain all intellectual property rights, including any idea, process, procedure, or article of manufacture described in the paper.

2. Authors/employers may reproduce and distribute copies of the paper within the company* or organization for which the author worked at the time the paper was written as well as within employers' business partners. Such distribution includes posting of the paper on the employer's intranet, even when that intranet includes non-employees.

3. Authors/employers may reproduce, or authorize reproduction of, and distribute up to 50 paper copies of the paper outside the company or organization for which the author worked at the time the paper was written and outside of employers' business partners for personal, business, or educational purposes provided that the SPE copyright notice is included, the copies are not used in any way that implies SPE endorsement of a product or service, and the copies themselves are not offered for sale. In addition, authors/employers may provide electronic copies of the paper to their business partners or to relevant government agencies.

4. Authors/employers may make an oral presentation of the same material or portions of the same material used either as a standalone presentation or incorporated in with other material.

5. Authors/employers may incorporate all or part of the paper in future writings or presentations. If the entire paper or a significant portion (>60%) is used in substantially unchanged form, proper acknowledgement of SPE copyright must be made. If the paper is substantially changed or altered in substance so that it is a new work of authorship, reference should be made to the SPE publication. Components of the paper [images, graphs, figures, and individual sections comprising less than a significant portion (≤60%)] may be used without acknowledgement of the SPE copyright within the company or organization for which the author worked at the time the paper was written, as well as within employers' business partners and with relevant government agencies, including in documents posted on the employer's intranet, even when that intranet includes non-employees.

6. Authors/employers may request return of one-time journal publication rights to enable publication of the paper in a journal or magazine if the paper is not being considered for publication in an SPE journal. Such requests should be made in writing to SPE Customer Service. Requests for return of one-time journal publication rights will not be granted for papers submitted to SPE for peer review unless the paper is declined for publication or it is at least 6 months after the submission date.

7. In the case of work performed under a U.S. government contract or grant, SPE recognizes that, if the contract/grant so requires, the U.S. government has royalty-free permission to reproduce all or portions of the paper and to authorize others to do so for official U.S. government purposes only.

8. For all uses not covered by Items 2 through 6, authors/employers must request permission from SPE to reproduce or authorize reproduction of the paper. Authors/employers may not post or distribute copies of the paper on a customer-facing or public-facing website without prior written consent by SPE.

9. Although authors are permitted to re-use all or portions of the paper in other works, this does not include granting third-party requests for reprinting, republishing, or other types of re-use. SPE must handle all such third-party requests.

Information for Authors

SPE policy requires that SPE hold copyright to all copyrightable material in its publications, including conference proceedings, and to the individual contributions contained therein, to protect the interests of SPE, authors and their employers, and at the same time, to facilitate the appropriate re-use of this material by others. SPE distributes its publications throughout the world and does so by various print and electronic means. SPE also may translate or authorize translation of its publications, and articles contained therein, for inclusion in various publications.

If you are employed and prepared this paper within the scope of your employment, the original copyright to the paper belongs to your employer. In that case, SPE assumes that when you sign this form, you are authorized to do so by your employer and that your employer has consented to the transfer of copyright, to the representation and warranty of publication rights, and to all other terms and conditions of the form. If such authorization and consent has not been given you, an authorized representative of your employer should sign this form in the space provided for the Author.

Most SPE conferences have a no-paper/no-podium policy. This means that no paper can be presented at the conference unless a written paper accompanied by a signed copy of this form transferring copyright to the paper to SPE is received by SPE before the manuscript due date to enable its publication in the conference proceedings. Failure to submit these materials to SPE by the due date will result in the paper being removed from the conference program.

NO MANUSCRIPT MAY BE PUBLISHED IN ANY SPE PUBLICATION, INCLUDING CONFERENCE PROCEEDINGS, UNLESS SPE HAS RECEIVED THIS SIGNED FORM. TO ENSURE UNIFORM TREATMENT AMONG ALL CONTRIBUTORS, OTHER FORMS MAY NOT BE SUBSTITUTED FOR THIS FORM, NOR MAY ANY WORDING OF THIS FORM BE CHANGED.

*Company or companies as used herein means the company the author worked for at the time the paper was written, such company's parent (if any), subsidiaries, and corporate affiliates.